UNIVERSITAT DE BARCELONA

Combined Transmission Electron Microscopy and In-Situ Scanning Tunneling Microscopy Characterization of Nanomaterials

Gemma Martín Malpartida

ADVERTIMENT. La consulta d'aquesta tesi queda condicionada a l'acceptació de les següents condicions d'ús: La difusió d'aquesta tesi per mitjà del servei TDX (**www.tdx.cat**) i a través del Dipòsit Digital de la UB (**diposit.ub.edu**) ha estat autoritzada pels titulars dels drets de propietat intel·lectual únicament per a usos privats emmarcats en activitats d'investigació i docència. No s'autoritza la seva reproducció amb finalitats de lucre ni la seva difusió i posada a disposició des d'un lloc aliè al servei TDX ni al Dipòsit Digital de la UB. No s'autoritza la presentació del seu contingut en una finestra o marc aliè a TDX o al Dipòsit Digital de la UB (framing). Aquesta reserva de drets afecta tant al resum de presentació de la tesi com als seus continguts. En la utilització o cita de parts de la tesi és obligat indicar el nom de la persona autora.

ADVERTENCIA. La consulta de esta tesis queda condicionada a la aceptación de las siguientes condiciones de uso: La difusión de esta tesis por medio del servicio TDR (**www.tdx.cat**) y a través del Repositorio Digital de la UB (**diposit.ub.edu**) ha sido autorizada por los titulares de los derechos de propiedad intelectual únicamente para usos privados enmarcados en actividades de investigación y docencia. No se autoriza su reproducción con finalidades de lucro ni su difusión y puesta a disposición desde un sitio ajeno al servicio TDR o al Repositorio Digital de la UB. No se autoriza la presentación de su contenido en una ventana o marco ajeno a TDR o al Repositorio Digital de la UB (framing). Esta reserva de derechos afecta tanto al resumen de presentación de la tesis como a sus contenidos. En la utilización o cita de partes de la tesis es obligado indicar el nombre de la persona autora.

WARNING. On having consulted this thesis you're accepting the following use conditions: Spreading this thesis by the TDX (**www.tdx.cat**) service and by the UB Digital Repository (**diposit.ub.edu**) has been authorized by the titular of the intellectual property rights only for private uses placed in investigation and teaching activities. Reproduction with lucrative aims is not authorized nor its spreading and availability from a site foreign to the TDX service or to the UB Digital Repository. Introducing its content in a window or frame foreign to the TDX service or to the UB Digital Repository is not authorized (framing). Those rights affect to the presentation summary of the thesis as well as to its contents. In the using or citation of parts of the thesis it's obliged to indicate the name of the author.

Tesi doctoral

Combined Transmission Electron Microscopy and In-Situ Scanning Tunneling Microscopy Characterization of Nanomaterials

Gemma Martín Malpartida

Directors: Dr. Albert Cornet Calveras
Dr. Sònia Estradé Albiol

UNIVERSITAT DE BARCELONA

Combined Transmission Electron Microscopy and In-Situ Scanning Tunneling Microscopy Characterization of Nanomaterials

Memòria presentada per optar al grau de doctor per la Universitat de Barcelona.

Programa de doctorat en Nanociències

Autora: Gemma Martín Malpartida

Directors: Dr. Albert Cornet Calveras

Dr. Sònia Estradé Albiol

Tutor: Dr. Albert Cornet Calveras

UNIVERSITAT DE BARCELONA

Dedicada al rei i a la princesa d'aquest conte de fades

Agraïments

La realització d'aquesta tesi es pot dividir fàcilment en dues etapes. La primera, en la que he après, experimentat, intentat, ensopegat, resolt i aconseguit. La segona, l'escriptura. Diria que la primera part ha estat com una muntanya russa amb moments frustrants i esgotadors i moments plens de felicitat, alegria i sensació de victòria. La segona ho resumiria en estrés i maduració. En les dues parts he tingut ajuda de molta gent, sense la qual hagués estat impossible arribar a aquest punt final (o més aviat hauria de dir un *punt i a part* o fins i tot, una *coma*).

Hi ha tanta gent a la que vull agrair el seu suport, esforç i ànims que no tinc clar per on començar, així que... començaré agraint als meus directors. Vull donar les gràcies al Prof. Albert Cornet, cap del departament d'Enginyeria Electrònica i Biomèdica, per haver contactat amb mi fa ja uns anys demanant-me formar part d'una nova línia de recerca en el LENS. Jo gairebé no sabia què era la microscòpia electrònica i encara menys com aquell treball final de màster sobre *in-situ* canviaria la meva vida. També vull donar les gràcies a la Dra. Sònia Estradé, per engrescar-me en aquest món, recolzar-me i donar-me mil idees quan a mi no me'n quedava cap. A més, voldria agrair-li totes les converses sobre temes no científics, però també importants

(política, feminisme...) i no tan importants (monty phyton, discworld...). Gràcies!

El meu agraïment més especial en el món professional va cap a la Prof. Francesca Peiró. Amb tot el meu cor, li vull agrair haver-me acollit en aquesta gran família que és el LENS. Gràcies a tu aquesta tesi ha estat possible i he pogut arribar al final sentint-me orgullosa del resultat. Ets el meu referent (soy tu fan!).

També vull agrair a tots els membres del grup de recerca en el qual s'ha dut a terme aquesta tesi, Micro-nanotecnologies i Nanoscòpies per Dispositius Electrònics i Fotònics (MIND), pel seu recolzament i moments compartits (calçotades, picatrònics i celebracions vàries...). Especialment voldria agrair al Dr. Sergi Hernández, pels moments durant la meva col · laboració en el màster de Nanociència i Nanotecnologia i per les bandes sonores i al Dr. Albert Cirera, nomenat recentment Vicerector de Transferència, Innovació i Emprenedoria (felicitats!), per endinsar-me en el món del grafè i compartir amb mi els seus coneixements.

A continuació, m'agradaria agrair el seu suport a la resta del grup del LENS: el Dr. Lluís Yedra que tant em va ensenyar del TEM durant els meus primers dies (i mesos), compartint discussions de sèries de TV i botigues de Gràcia; el Josep Rebled, que escoltant Eugenio, em va regalar tots els seus coneixements del FIB; el Dr. Alberto Eljarrat, que em va ensenyar que aquí es dina a la una; el Dr. Lluís López (l'altre Dr. Lluís), amb el que he après tant compartint infinites hores al TEM; el Pau Torruella, que encomana la seva passió (ets el pròxim, no?); la Catalina Coll, amb la que he après que la vida no és tan dramàtica (i menys si hi ha una platja); el Javier Blanco, el de les samarretes de tirants; el Sergi Plana, el més ràpid del *oeste* en trobar *typos*; i per

últim, la nova incorporació, que ja sap que li tinc un *carinyo* especial, el Daniel del Pozo.

Als meus companys del despatx Patera, per tots els moments compartits i les necessàries estones de cafè: el Dr. Julià López, la persona que més vegades m'ha desitjat un bon any nou; l'Oriol Blàzquez, que sempre té un ~~bon~~ acudit preparat; l'Adrià Huguet, l'empresari en bici; el Dr. Giovanni Vescio, per totes les converses sobre ReRAMs; el Juan Luis Frieiro, el ciao-ciao. I la resta de companys del MIND, especialment a la Dra. Aïda Varea, per les estones compartides al Raman i fora del Raman.

També vull donar les gràcies a persones que m'han ajudat durant aquest viatge, més enllà del món científic. Primer vull agrair a la Roser Marzo tota la seva feina, fas que tot aquest viatge ple de corbes sigui més fàcil. També vull fer menció al Jordi Pardo i a la Mila Rodríguez, del grup d'innovació docent, amb qui vaig compartir moments que mai oblidaré al principi de la tesi.

No vull oblidar-me de tota la gent que m'ha ajudat als Centres Científics i Tecnològics de la UB. Vull començar amb el Dr. Quim Portell, el qual m'ha ajudat enormement en la part més tècnica d'aquesta tesi. També vull donar les gràcies al Joan Mendoza, la Dra. Aranzazu Villuendas, el Fèlix Mata, l'Eva Prats i el David Artiaga.

Més enllà del departament d'Enginyeria Electrònica i Biomèdica i de la Universitat de Barcelona, voldria agrair a tota la gent que m'ha ajudat d'una manera o altre a fer possible aquesta tesi. En primer lloc vull mencionar al Dr. Xavier Borrisé, per acollir-me al seu nano-grup com una més durant la meva estada al IMB-CNM, del qui he après moltíssim. Del CNM voldria també enviar els meus agraïments a l'Ana,

la Liber, l'Albert, i tothom amb qui vaig compartir estones durant 3 mesos que es van fer molt curts.

També vull donar les gràcies per les estones al FIB al Trifon Trifonov de la UPC i a la Rocío Romero de la UMA. Gracias a los dos, he aprendido muchísimo de vosotros!

Voldria agrair també als nostres col · laboradors d'arreu del món, i especialment, a la Dra. Marie-Helene Chambrier de la universitat d'Artois, a la Prof. Francesca Campabadal i la Dra. Mireia Gonzalez del IMB-CNM i al Prof. Carlos Algora del IES-UPM.

Finalment voldria dedicar aquesta tesi a les persones que realment han fet possible que jo hagi arribat on he arribat. A la meva família. Als meus pares que m'han recolzat i animat en tot aquest viatge, des del primer dia. Per fer-ho TOT possible. Us estimo! Als meus germans, per fer de mi una petita *friki*. Als meus sogres, per fer-me sentir estimada com una filla. A les meves cunyades, que cada una d'elles és la millor cunyada del món! A la Mari, que és com una germana per mi. Al meu tiet putatiu. A la iaia Paquita, i també, tot i que no puc dedicar-li en persona, al yoyo (te llevo siempre en mi corazón).

I per últim, a les dues personas més importants de la meva vida. A l'Antonio, el meu amor. Gracias por estar a mi lado, enseñarme qué significa la felicidad, apoyarme cuando te he necesitado y dejarme envejecer a tu lado. Cada página de esta tesis es también un reflejo de todo lo qué me has enseñado a lo largo de estos años. TE AMO. I a l'Eulàlia. No tinc paraules per expressar el meu amor. Vas venir al món tot just quan començava l'aventura de la tesi. T'he vist créixer durant aquests anys i m'has fet créixer a mi també. T'estimo princesa. Aquest conte de fades és per vosaltres.

Contents

1 Introduction **1**

1.1 *In-situ* Transmission Electron Microscopy 1

1.2 Heating holders 4

1.3 Biasing holders 7

1.3.1 Biasing with chip-based holders 8

1.3.2 Biasing with direct manipulation 9

1.4 Mechanical holders 11

1.5 Gas holders 13

1.6 Liquid Cell holders 16

1.7 Using TEM as a Nanolab 20

1.8 Challenges 21

1.9 Summary and scope of this thesis 22

1.10 References 25

2 Instrumental **35**

2.1 TEM-STM holder 36

2.2 Sample preparation 39

2.2.1 Nanostructured materials 39

2.2.2 Localized preparation 42

2.3 TEM-STM holder improvements:
a gridcase 46

2.4 TEM-STM system calibration 49

2.5 Analyzing I-V curves 53

2.6 Conclusions 56

2.7 References 58

3 Effects of electrical current on Graphene Oxide (GO) sheets **61**

3.1 Graphene Oxide (GO) 61

3.2 Electrodeposition of Graphene Oxide sheets 64

3.3 Electrical characterization 65

3.4 Joule heating 68

3.5 Raman studies 69

3.6 High voltage effects 74

3.7 Conclusions 77

3.8 References 78

4 Piezo- and ferroelectricity of lead-free thin films **85**

4.1 Piezoelectricity and ferroelectricity 85

4.2 Advanced ferroelectric materials 88

4.3 α-La_2WO_6 films growth 90

4.4 Preliminary TEM characterization 93

4.5 *Ex-situ* AFM characterization 95

4.6 Piezoelectricity *in-situ* characterization 96

4.7 Ferroelectricity *in-situ* characterization 100

4.8 Conclusions 101

4.9 References 103

5 Electrical anisotropy in ordered GaInP **107**

5.1 III-V compounds 107

5.2 GaInP for multi-junction solar cells (MJSC) 109

5.3 Sb-flux assisted growth of GaInP 111

5.4 General TEM characterization 113

5.5 TEM study of the order parameter 114

5.6 Electrical characterization 118

5.7 Conclusions 121

5.8 References 122

6 Resistive switching studies of ReRAM devices **127**

6.1 ReRAM memories 127

6.2 Al/SiAlON/Si 131

6.2.1 Sample growth 132

6.2.2 Electrical characterization 133

6.2.3 TEM preliminary characterization 134

6.2.4 Structural and compositional analysis after the electroforming process 136

6.2.5 Discussion 147

6.3 Ag/HfO_2/Pt/Si inkjet-printed structure 148

6.3.1 Sample growth 149

6.3.2 Electrical characterization 150

6.3.3 Preliminary TEM characterization 151

6.3.4 Compositional analysis after the electroforming process 153

6.3.5 Discussion 157

6.4 Ni/HfO_2/Si 160

6.4.1 Sample growth and electrical characterization . 160

6.4.2 Preliminary characterization 163

6.4.3 Assessment of the devices after the electroforming process 163

6.4.4 *In-situ* polarization 171

6.4.5 Discussion 175

6.5 Conclusions 179

6.6 References 181

7 Conclusions **189**

Appendix A Resum en català **197**

Appendix B Scientific Curriculum **205**

Chapter 1

Introduction

1.1 *In-situ* Transmission Electron Microscopy

Microscopy is defined as the study of objects that are too small to be easily viewed by the unaided human eye, viewing objects that range in size from millimeters down to nanometers. But it was not until 1931 when Max Knoll and Ernst Ruska [1] at the Berlin Technische Hochschule, with the invention of the electron microscope, finally overcame the barrier to higher resolution that had been imposed by the limitations of visible light.

Today, almost a century later, the highest resolution TEMs have sub Angstrom resolving capabilities. However, classical electron microscopy provides only passive images, the object is visible but it is not possible to interact with it. It is, therefore, interesting to combine electron microscopy with *in-situ* TEM techniques. *In-situ* TEM microscopy

refers to the techniques that allow a direct observation of the dynamic properties at the nanoscale of materials subject to external stimuli (e.g. environment, a temperature change, stress, an applied external electric or magnetic field, etc.) through imaging, diffraction and quantitative measurement of some properties using the TEM (see figure 1.1).

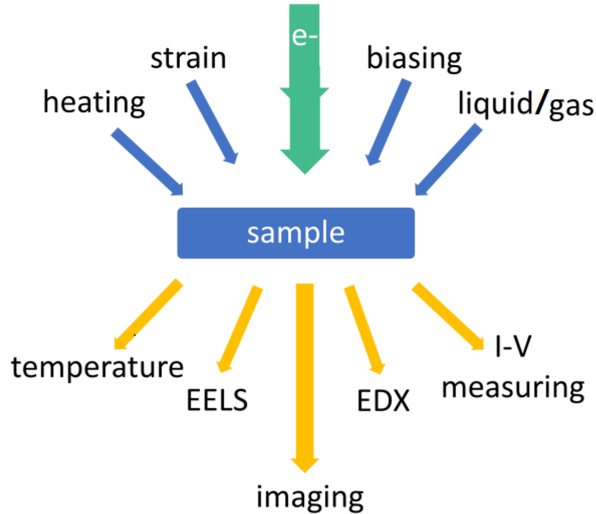

Figure 1.1 Schematic of the different *in-situ* TEM techniques combined with conventional TEM measurements.

In 1959, less than 20 years after the invention of the electron microscope, Richard Feynman issued an invitation to scientists to enter in this new field of discovery with his lecture entitled "There's Plenty of Room at the Bottom" saying “I put this out as a challenge: Is there no way to make the electron microscope more powerful?” [2], pointing out that there is still plenty of room for miniaturization and that in principle we should be able to manipulate the positions of individual atoms. From an early stage in the development of TEM, the idea was brought up that the microscope should be transformed into a micro-laboratory in which the response of the specimen to both stimuli and the surrounding environment could be recorded in real

time [3]. Nowadays *in-situ* TEM is becoming more and more relevant in the scientific community, as reflected by the exponential growth of the number of publications in the last few years related to *in-situ* TEM [4] (Figure 1.2). This is true not only in absolute terms but also for the percentage of available *in-situ* TEM with respect to TEM publications. Also, the number of *in-situ* TEM holders and the number of companies manufacturing them have seen a large increase [5].

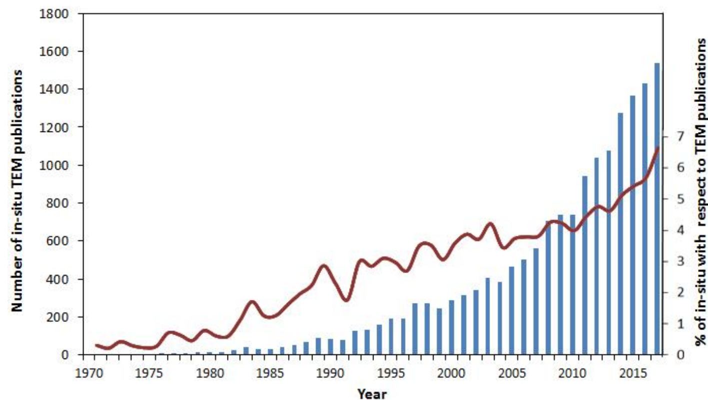

Figure 1.2 Number of publications identified using the keywords "*in-situ*" (blue bars) and percentage of "*in-situ*" publications with respect to "TEM" publications (red line), showing a steady increase over the last 20 years [4].

Thus, *in-situ* experiments have two important components: external stimuli and real time observations. To apply different external stimuli inside the TEM, special holders are needed, which is the most challenging demand. For real time observations, a fast recording system is also required.

The most traditional *in-situ* experiment is the study of thermally induced structural phase transitions [6]. Nevertheless, apart from heating and cooling, holders with a diverse range of functionalities are now available for mechanical or electrical measurements, amongst others. Using a combination of microelectromechanical systems (MEMS) based devices and special TEM holders, the changes in a

specimen can be visualized in real time. Also, appreciable progress has been made for the development of windowed cell holders to observe solid/liquid and solid/gas interactions at high temperatures [7,8].

Furthermore, developments in *in-situ* TEM combined with aberration corrected high-resolution imaging, electron energy-loss spectroscopy (EELS), and energy dispersive x-ray spectroscopy (EDX) have enabled many discoveries in dynamic materials processes at the atomic level that were not previously possible [9–13].

In this chapter the most relevant *in-situ* TEM techniques are presented, from heating holders to holders that combine multiple techniques, allowing the use of the TEM as a nanolab. A comprehensive description of the modes of operation and possible working conditions of these devices is given in the following sections.

1.2 Heating holders

Many phenomena occur at elevated temperatures that are of fundamental interest. The use of specimen heating during TEM observation allows the possibility to study direct phase transformations, such as nucleation and growth, recrystallization or dissolution processes, amongst others.

The first *in-situ* heating TEM stage was reported in 1960 to allow the observation of annealing effects on dislocations in aluminum [14]. Conventional *in-situ* heating stages for TEM were usually integrated as part of the specimen holder and were made of tantalum, beacuse of its high melting temperature and structural stability during thermal cycling. In these holders, a heating filament embracing a 3mm-diameter TEM specimen disk acted as an electric furnace and could reach

1300°C for single-tilt holders and 1000°C for double-tilt ones. In a furnace-heating holder, the thermal radiation heated the specimen, which was, therefore, an indirect heating mechanism. An embedded thermal couple measured the temperature in the furnace cup and cooling water was used to minimize the heating of other parts of the holder and to reduce specimen drift. However, the total thermal expansion effect caused a severe problem of sample drifting when changing temperature. Figure 1.3 (a) depicts a Gatan single tilt heating stage.

In order to perform high resolution TEM imaging at elevated temperatures, it is imperative to obtain high temperature stability and low sample drift [15]. This is difficult to achieve with a large sample stage that has a very large thermal mass and, also, a slow temperature response. Recently, to address this issue, MEMs heating stages have been developed[1] (figure 1.3(b)). These holders use integrated circuitry to produce localized resistive heating directly on the sample support, and therefore, they minimize the distance between the heating filament and the sample and only heat a small region. Thus, such stages show a much lower thermal mass and a very high thermal stability, which allows high resolution imaging at elevated temperatures.

The main drawback for MEMs-based heating holders is that the sample must be placed in a small window. These holders work best for thin films or nano-materials, that can be directly deposited from solution or sputtered onto the window and analyzed in vacuum.

Even if heating TEM holders are amongst the first *in-situ* TEM devices, they are still widely used for the characterization of new materials in a wide range of temperatures and for multiple applications. Recently, Wang et al. [16] studied the annealing of copper silicide

[1]Commercially available by Protochips Inc. and DENs solutions.

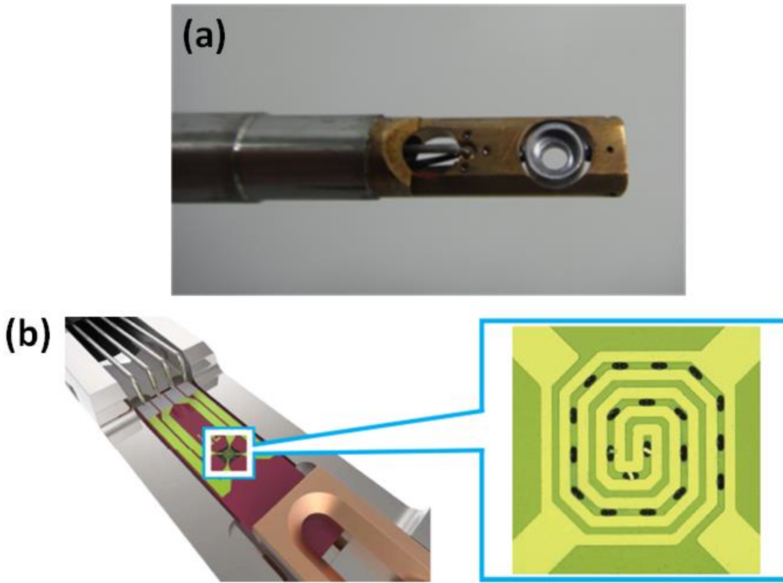

Figure 1.3 (a) Example of a single tilt heating stage design by Gatan Inc. (b) Example of a chip-based heating holder design by DensSolution Inc.

nanowires and their field emission properties using *in-situ* heating holders. Neklyudova et al. [17] demonstrated that it is possible to locally transform a 25nm thick polycrystalline Bi thin film into a [111]-oriented single-crystalline film in the TEM. In the Spanish context, one of the most recent publication is presented by Ortega et al. [18], studying the size effect on the melting temperature of Sn nanoclusters and nanorods, and diffusion of voids along the nanotube axis during heating treatments.

1.3 Biasing holders

In-situ TEM electrical characterization allows a better understanding of nanostructured materials such as nanowires, nanotubes and nanoparticles by establishing a quantifiable direct correlation between

composition or structure and electrical characteristics. Moreover, the changes in the electrical properties of the nanostructures can be correlated with changes of composition and structure in real time.

Early examples of employing electrical contacts for *in-situ* TEM experiments can be found when Blech and Meieran investigated electromigration in aluminum thin films in 1967 [19]. The continued interest in performing *in-situ* TEM electrical measurements comes from the exceptional opportunity for real-time monitoring by imaging, diffraction or spectroscopy, enabling to stablish causality effects between electrical current or biasing and sample tranformations by electromigration or Joule heting effects.

The two main types of modern holders for *in-situ* TEM electrical measurements are chip-based holders with fixed contacts and holders where the contact is achieved by *in-situ* TEM manipulators such as the TEM-STM system.

1.3.1 Biasing with chip-based holders

Historically, biasing holders consisted on bringing as many contacts as possible into the TEM via the sample holder. Nowadays, two main characteristics differentiate the chip-based biasing holders: the number and the versatility of the contacts.

The chip-based approach uses prefabricated circuitry developed by lithography on silicon chips containing thin silicon nitride membranes (Figure 1.4 shows an example of a chip-based *in-situ* holder[2]). In this type of holders two methods can be employed to connect the sample to the sample holder: clamping or bonding. In the case of clamping,

[2]Designed by DensSolution Inc.

the clamp ensures the mechanical stability and the electrical contact as well; it is less versatile because all samples need to be adapted to the clamp. The bonding method is more versatile but requires a more careful handling.

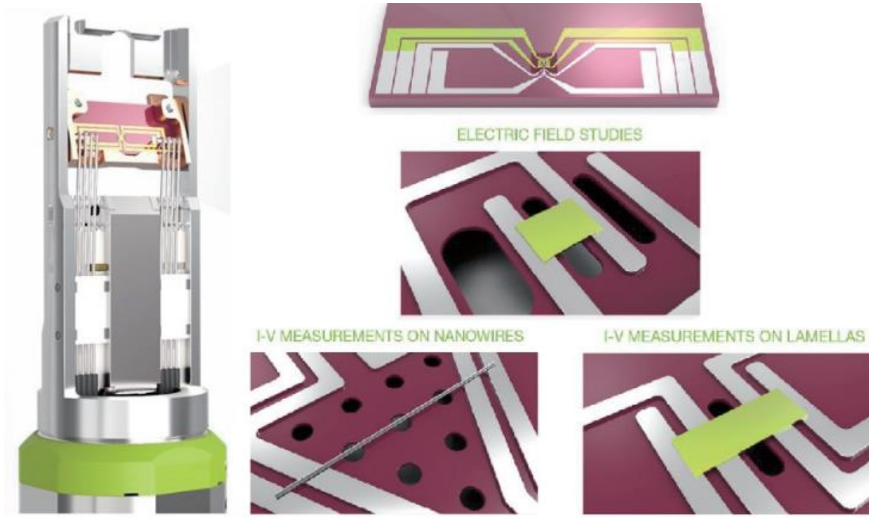

Figure 1.4 Example of a chip-based *in-situ* holder designed by DensSolution Inc.

Furthermore, some commercial chip-based holders incorporate from 4 to 8 point-probe methods both for biasing and heating, allowing for simultaneous biasing measurements at elevated temperatures.

Recently, B. Wang et al. [20] studied the domain switching in GaN thin films by using a single tilt *in-situ* holder with four electrical ports for electrical biasing, and den Hertog et al. [21] combined *in-situ* biasing and off-axis electron holography to charaterize ZnO nanowires.

1.3.2 Biasing with direct manipulation

In the case of *in-situ* TEM for electrical measurements with direct manipulation, an STM tip is used as an electrical probe to characterize

single nanostructures (see Figure 1.5). The TEM-STM system has been used in this thesis to adress the characterization of relevant nanomaterials.

In this *in-situ* technique, the probe can be positioned in a millimeter-scale workspace with subnanometer resolution using an STM unit actuated by a three-degree-of-freedom piezotube. This enables selecting a specific nanostructure and applying a voltage to perform electrical measurements [22,23]. This approach is relatively more straightforward but requires a dedicated piezo-driven stage.

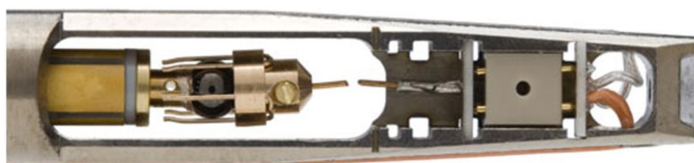

Figure 1.5 TEM-STM holder with direct manipulation used for electrical measurements from Nanofactory Inc.

One of the first results with the TEM-STM system was presented by K. Svensson et al. [24] in Chalmers University of Technology in Göteborg. They demonstrated experimentally how carbon nanotubes (CNTs) can be used as "nanopipettes" in order to deposit and retrieve solid material at a nanometer scale. The sample, multiwalled carbon nanotubes (MWNTs) filled with iron, was attached to a metal wire. The movable tip was used to approach individual MWNTs and to make an electrical contact. By driving high current through the nanotube, the entrapped iron started to migrate in a direction opposing the electric field (see Figure 1.6).

Recently, the TEM-STM system has been used to study the lithiation behavior of individual nanostructures in order to design a new generation of lithium ion batteries (LIB). Q. Su et al. [25] studied the dynamic behavior and the electrochemical reaction of

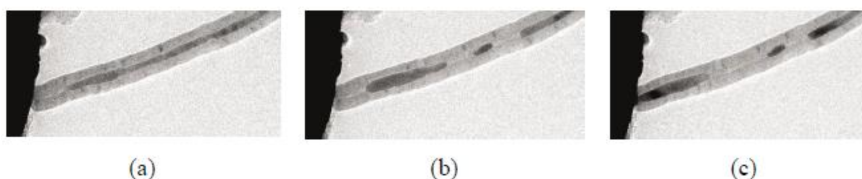

Figure 1.6 Sequential TEM images showing the induced movement of iron [24].

carbon-coated Fe_3O_4 nanowires revealing that the lithiation process involves the conversion of Fe_3O_4 nanowires to Fe nanograins and the formation of Li_2O along the lithium ions diffusion direction. The delithiated product is FeO rather than the original phase of Fe_3O_4 after the first delithiation process (Figure 1.7).

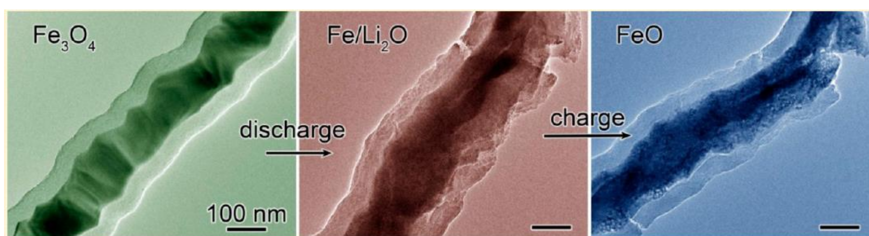

Figure 1.7 Example of a study on the lithiation behavior of individual nanostructures with an application in lithium ion batteries using the TEM-STM system [25].

1.4 Mechanical holders

Nanoindentation, or instrumented indentation, is a technique that consists in measuring the force and displacement of a hard tip (often a diamond tip) forced into a bulk material. Nanoindentation and atomic force microscopy techniques are commonly used to investigate mechanical properties of nanoscale materials such as very thin layers, nanowires and nanotubes, as well as nanoparticles.

But it was not until the first observations of moving dislocations in a TEM from the mid 50s [26] that nanoindentation in the TEM

became relevant. Since then, many research laboratories have designed and manufactured their own straining holders [27–29]. By the 1980s significant advances in nanoscale science and instrumentation led to the first instrumented indentation techniques at sub-micron length scales. Pethicai et al. [30] first demonstrated the approach of providing a continuous measurement of load and displacement during indentation with resolutions in the sub-microNewton and the sub-nanometer regimes.

Nowadays, nanoindentation experiments in the TEM are generally based on using one of two approaches: fabricated MEMs that are fitted within a TEM specimen arm [31,32], and dedicated nanoindentation stages encompassing piezo-driven probes integrated with the TEM specimen arm [33–35] (similarly to the electrical probing within the TEM).

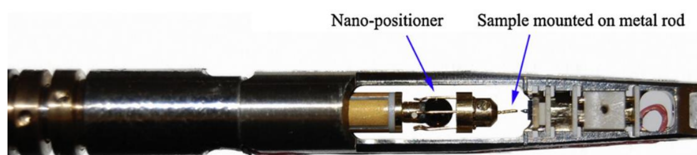

Figure 1.8 Dedicated nanoindentation stage for direct manipulation from Nanofactory Inc.

In the MEMs system approach, a load is applied using a thermal actuator on one side of the freestanding specimen and is measured on the other side, using a differential capacitive load sensor based on interdigitated electrodes. The specimen is mounted between the actuator and load sensor shuttles. MEMs design has the advantage of incorporating multiple capabilities into one platform, so that temperature control, electrical measurements and mechanical testing may be completed while imaging in the TEM. Nevertheless, most MEMs holders only operate on a single-tilt platform.

The piezo-driven nanoindenter or Atomic Force Microscopy (AFM)-TEM holders are configured with a diamond tip stable on one end and the sample attached to the piezo tube on the opposite side (Figure 1.8). The sample is controlled in 3D with a piezoelectric actuator, allowing fine movements down to 0.1nm/step. These holders are able to produce curves for load and displacement vs time and have double-tilt capability, allowing the orientation of the specimen along a particular axis. These types of holders have frequently been applied to probe the mechanical properties of grown nanowires. Flat punched tips can also serve to compress nanoparticles, but, in any case, modeling of the deformed sample is needed to obtain quantitative data [36,37].

As examples, the Golberg group [38] in 2010 demonstrated for the the first time the highest tensile strengths (up to 100 GPa) of individual SWNTs and multi-walled boron nitride nanotubes (up to 33 GPa) under tensile tests inside the TEM using a TEM-AFM holder. Kim et al.[39] in 2012 focused on complex heterogeneous amorphous CNT–boron nitride nanotube (BNNT) nanostructures and documented $\sim$5.3 GPa tensile strength for such hybrids. Recently, B. Ozdol et al.[40] have explored the structural and electronic properties of InAs and InAs/GaAs core-shell nanowires at their mechanical limits.

1.5 Gas holders

The introduction of gases in environmental TEMs (ETEMs) has expanded the capabilities of *in-situ* TEM, making it a versatile technique to study catalytic reactions, nanomaterials synthesis and corrosion, among others. [41–44]

The challenge of this technique is maintaining the high vacuum in the TEM column when the gas is introduced into the specimen area

since the high energy electron beam requires high vacuum conditions to avoid undesirable scattering from gas molecules. There are two approaches to solve this problem: specially designed environmental TEMs equipped with pumped vacuum systems [45] and sealed gas cells integrated into special TEM holders [46].

The first designs for environmental mimicking operation of the TEM were reported over 70 years ago [47,48] and were produced by either of both approaches, incorporating differentially pumped apertures that separate the specimen from the high vacuum of the TEM column [49–52] or windowed-cell designs that confine the gas within the specimen holder using electron-transparent membranes [53–56]. Atomic-resolution images in gaseous environments have been obtained with both techniques at pressures up to $\sim$10 Torr but the technological relevance of these measurements may not be compatible with the more realistic operating conditions of catalyst nanomaterials at higher pressures. ETEM microscopes that incorporate differentially pumped apertures are generally limited to pressures of 15–20 Torr but they allow imaging a standard TEM sample. A windowed-cell approach produces a much thinner layer of gas than a differentially pumped ETEM and allows examining samples at pressures greater than 50 Torr. However, the additional electron scattering due to the window membranes can decrease the attainable contrast and resolution.

Atomic-scale imaging of catalysts and other nanoparticles also benefits from *in-situ* aberration corrected high-angle annular dark-field (HAADF) TEM imaging. This imaging mode can provide directly interpretable atomic-scale images of catalyst nanoparticles at the required pressures and temperatures. HAADF imaging is ideal for catalysis studies in which small particles or clusters of heavy atoms sit on a substrate and it is necessary to differentiate chemically inhomogeneous structures at small spatial scales [57,58]. Recently, de

Jonge et al.[59] reported a resolution of 0.4 nm for gold nanoparticles at ambient gas pressure using a windowed-cell holder in STEM mode (Figure 1.9).

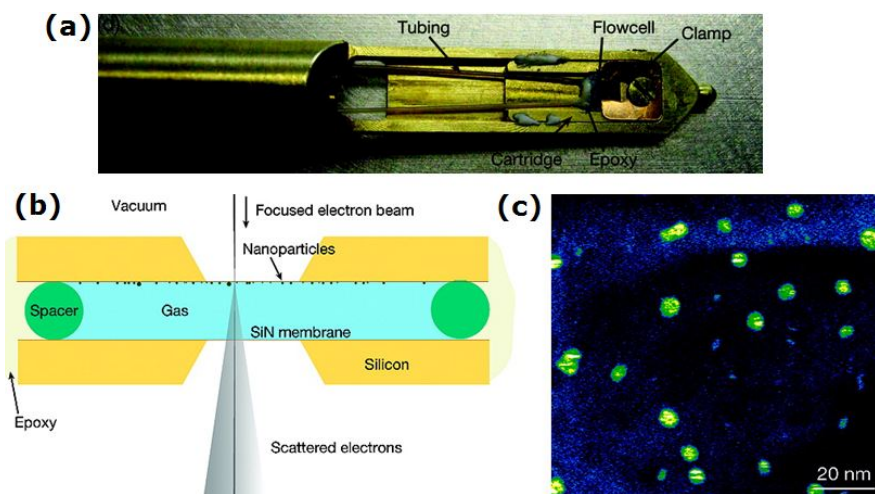

Figure 1.9 (a) Picture of the specimen holder for atmospheric pressure STEM, (b) Schematic of the flow system for atmospheric pressure STEM and (c) STEM image showing gold islets on the top SiN window [59].

Although ETEM makes it possible to obtain time-resolved atomic-resolution images and chemical information during reactions, accurate temperature measurement of the specimen area being observed, especially under conditions of flowing gas, is lacking. As a result, quantitative thermodynamic and kinetic measurements from *in-situ* data may have large uncertainties.[60]

In this sense, Creemer et al. designed a “nanoreactor” based on the microelectromechanical system (MEMS) technique, as shown in Figure 1.10 [61]. This nanoreactor allows researchers to heat the sample to 500 °C and to keep it in a 1.2 bar of H_2 atmosphere. Spatial resolution of 0.18 nm was achieved for the observation of Cu particles on ZnO at 300 kV. With the improvement of MEM systems, more advanced designs of pressure gas cell are under rapid development.

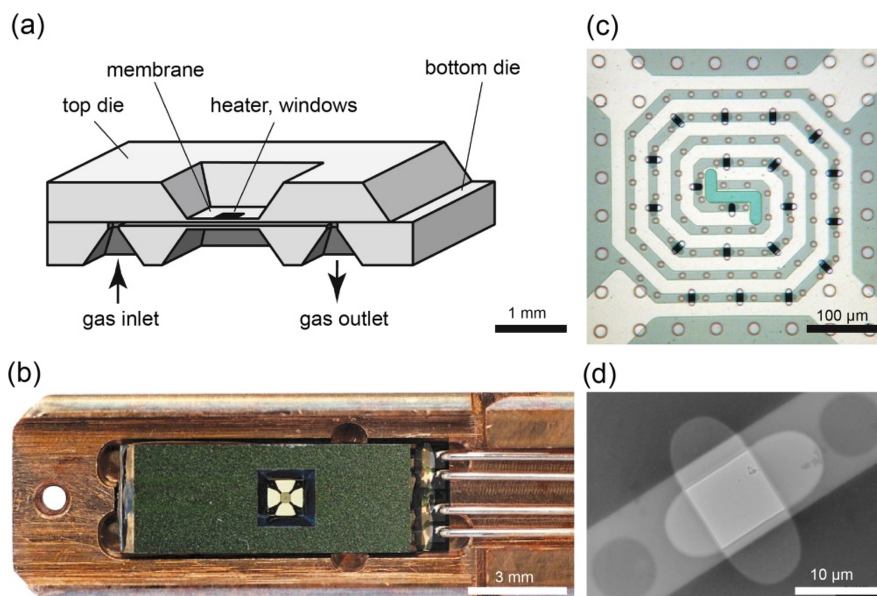

Figure 1.10 Illustration of the nanoreactor device: (a) Schematic cross-section of the nanoreactor. (b) Optical image of the TEM holder with the integrated nanoreactor and the four electrical probe contacts. (c) Optical close-up of the nanoreactor membrane. (d) A low-magnification TEM image of a pair of superimposed 10 nm thick windows [61].

In summary, although the windowed cell may reduce the spatial resolution of the TEM, the combination of *in-situ* gas holders with other techniques, such as X-ray spectroscopy, makes it possible to study the reaction dynamics inside the TEM [62].

1.6 Liquid Cell holders

In recent years, special holders have been developed for measurements in the TEM in a liquid environment. Two different techniques were developed for getting liquid inside the electron microscope while still maintaining a high enough vacuum to operate the electron source: the "open cell" and the "closed cell" approaches.

The first reports of TEM in liquids appeared in the 1940s using both open [63] and closed [64] cell technologies. The "open cell" approach consists in using differential pumping to control the pressure at the sample region. By contrast, the "closed cell" consists in enclosing the liquid between two electron transparent windows. By physically confining the liquid within a thin layer, imaging is possible in transmission mode through the windows and liquid. Nevertheless, the windows were thick and their separation of several micrometers was large enough to reduce the image resolution to a value not much better than that of light microscopes.

In the last decade, closed liquid cell (LC) has experienced a surge of interest due to the use of modern microfabrication techniques, allowing new types of thin membranes to separate a liquid specimen from the vacuum in the TEM [65] and obtaining nanometer resolution in liquid for biological samples [66] and for nanoparticles [67]. Moreover, microfabrication allows incorporating additional functionalities to the modern liquid cells such as liquid flow, electrodes, or heating and cooling.

There are several ways to encapsulate liquids in a LC in order to image them in TEM. The most popular approach, based on microfabricated chips, involves paired silicon chips with windows made of electron-transparent thin-film membranes. These chips are mounted together in what is typically named a "sandwich" chip system. For most systems, the amorphous ceramic silicon-rich silicon nitride is the preferred choice for the thin-film membrane fabrication (Figure 1.11).

In materials science, the modern LC has provided information on electrochemistry [65], nucleation and growth of nanoparticles [67], physics of fluids [69], reactions in batteries [14], corrosion [70] and biomineralization [71] among others.

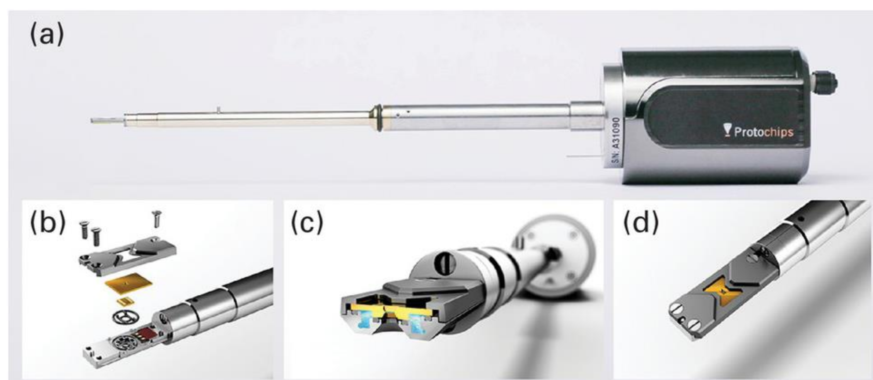

Figure 1.11 Example of a LC design by Protochips Inc. (a) The LC holder, (b) exploded view showing the tip assembly with o-rings and contacts for electrochemistry or heating, (c) cross-sectional illustration showing the liquid pathway and d) top view illustration showing the cutout that optimizes the design for EDX. [68]

In life sciences, cryogenic TEM (cryo-TEM) techniques have been used for over 30 years to address issues related to biological sample preservation. In this method, a sample is rapidly frozen by plunging it into a liquid ethane or propane slurry that is separately cooled by liquid nitrogen. This method preserves high-resolution components of the sample and also provides better tolerance against beam induced damage during imaging. However, the process of freezing completely excludes the possibility of observing dynamics in real time.

To allow for real-time TEM observations of dynamics that occur on a microsecond or faster timescale such as loop and domain motion, biological samples need to be imaged in a fully hydrated and non-frozen state. Nowadays not only biological structures can be resolved using LC TEM under fully hydrated conditions, such as virus and bacteria, spores or human body cells, but also biological processes can be stimulated *in-situ* by injecting nutrients.

However, studying physiological processes of live cells with electron microscopy is still difficult because the minimum needed electron dose

to obtain contrast is already many orders of magnitude above the lethal dose known to cause reproductive-cell death. Two different solutions are reported in the literature: combining light and electron microscopy, whereby a process is followed with the light microscope and “snap shot” electron microscopy is then used to reveal molecular configurations [72,73] and using time-lapsed Scanning TEM (STEM) with a low-dose radiation per image (0.3-0.2 $e^{-}/Å^{2}$) combined with positive stain at a very low concentration to improve the contrast [74].

Many examples of biological samples observed with LC TEM and STEM in the last few years can be found in the literature. In 2011, the de Jonge group [75] observed the intracellular uptake of 30 nm diameter gold nanoparticles in pristine eukaryotic cells. In 2013, Dukes et al. [76,77] presented for the first time the observation of rotavirus double-layered particles (DLPs) in a native liquid environment, obtaining a 3D model of the subviral particles (Figure 1.12 c)) and Chen et al. [78] presented the 3D motion of DNA-Au nanconjugates at nanometer resolution. In 2015, J. Park et al. [79] observed structures of H_3N_2 influenza viruses in a buffer solution for the first time using graphene LC. More recently, Kennedy et al. [74] have visualized live bacterial physiology with a 5 nm resolution (Figure 1.12 b) and c))using the time-lapsed STEM, and Peckys et al. [80] have presented the study of the molecular drug response in breast cancer cells.

1.7 Using TEM as a Nanolab

In the last few years the field of *in-situ* TEM has been changing rapidly for two main reasons: nanotechnology is making it possible to build better and more flexible holders and there has been a

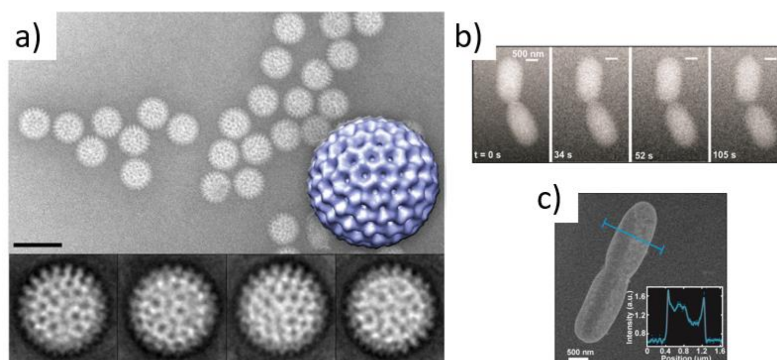

Figure 1.12 (a) Representative image and 3D reconstruction (inset) of rotavirus DLPs in liquid containing contrast reagent. Scale bar, 150 nm [76], (b) STEM snapshots of E. Coli taken at random intervals and (c) High-resolution HAADF STEM imaging of E. Coli [74].

marked improvement of the data recording and collecting systems. As a consequence, using a TEM as a nanolab is possible nowadays, combining all the capabilities presented in this chapter. It is now possible to strain the sample while heating it, or even strain a sample while heating it in a controlled environment and measuring its electronic behavior, reproducing conventional studies in a laboratory with atomic resolution inside the TEM.

In this sense, the Ross group was one of the first groups to reproduce the dynamic processess of electrochemical reactions for the growth of nanowires [81,82]. Recently, G. M Bremmen et al. [83] used a MEMS nanoreactor in combination with a specially designed *in-situ* TEM holder and gas supply system for the imaging of the formation of multiple layers of graphene encapsulating a cobalt nanoparticle, at 1 bar CO:N_2 (1:1) and 500°C. Moreover, P. Liu et al. [84] investigated the nucleation, growth and decomposition of Li_2O_2 micro-batteries in a basic liquid-state Li-O_2 system during discharging and charging by using an *in-situ* Electrochemical Cell (EC) and HAADF-STEM observations at a constant current density, together with synchronized electrochemical measurements.

1.8 Challenges

There are several challenges to consider for *in-situ* TEM instruments. Not only the presence of a high energy electron beam and the high vacuum conditions are problematic, but also the lack of space due to the pole piece geometry and the TEM holder rod itself are two limiting factors.

The space between the upper and lower pole piece in the TEM typically varies from 2mm to 5mm (it can be up to 10mm in the most favorable cases)(Figure 1.13). In conventional TEMs, ultra-high resolution pole-pieces (URPs) used for high resolution imaging have a typical gap of 2 mm, which is too narrow for most *in-situ* TEM setups. On the other hand, TEMs with analytical (ARP) and cryogenic pole-pieces (CRP) can accommodate any *in-situ* holder but the overall image resolution is degraded. More recently, with the development of aberration-corrected TEMs, several manufacturers have installed ARP pole-pieces in these instruments, thus allowing both high-resolution imaging and *in-situ* experiments. Nevertheless, the thickness of *in-situ* holders means that specimen tilt will be limited when compared to standard single-tilt and double-tilt holders.

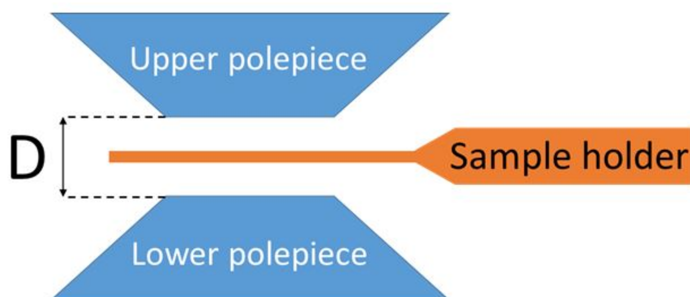

Figure 1.13 Schematic illustration of the objective lens structure used for a TEM system. The lens is composed of upper and lower polepieces. The TEM specimen is loaded in the pole piece gap.

As already mentioned, in the case of *in-situ* electrical measurements in the TEM, one important issue is the influence of the electron beam. The electrical and magnetic fields and high-energy electron bombardment disturbs the operation of the investigated device and those effects need to be decoupled during analysis of the results. As an example, irradiation by electrons can create electron-hole pairs in a semiconductor sample, plasmons in metals, and trapped electrons that can charge insulating regions and interfaces which might influence, for instance, the I-V behavior of a sample. Hence, interpretation of the experimental results of *in-situ* electrical measurements needs careful consideration.

1.9 Summary and scope of this thesis

In this thesis, *in-situ* TEM for electrical measurements through direct manipulation using a STM tip, combined with TEM imaging and spectroscopic techniques, has been used to address the characterization of relevant nanomaterials.

In the **second chapter**, the set-up and calibration of the system, the sample preparation procedures and the improvements on the TEM-STM holder carried out during the thesis will be presented.

After the standarization of the experimental set-up, specific approaches are optimized to be applied to different types of nanomaterials. The systems characterized using *in-situ* TEM biasing in combination with structural and analytical characterizations are classified according to the type of nanostructure and their application, from 2D nanostructures to functional devices.

In the **third chapter**, to better understand the behavior of Graphene Oxide (GO) in electronic nano-devices, the elucidation of

the effects of electrical current through a single graphene oxide sheet is addressed by *in-situ* TEM in combination with Raman spectroscopy.

In the **fourth chapter**, the ferroelectric and piezoelectric behavior of structures based on La_2WO_6 will be studied by using *in-situ* TEM.

In the **fifth chapter**, the anisotropic electrical conductivity of GaInP $CuPt_B$ type ordering layers used for multijunction solar cells will be assessed by *in-situ* TEM.

In the **sixth chapter**, the study of the conductive filament (CF) formation mechanism in ReRAM devices will be carried out by *in-situ* TEM analyses showing the structure and composition of the CF.

Finally, a **Conclusions** chapter will summarize the results obtained pointing out the relevance of *in-situ* TEM microscopy as a very useful and versatile tool to electrically characterize samples from nanomaterials to functional devices.

1.10 References

[1] M. Knoll and E. Ruska, "The electorn microscope", Z. Phys., vol. 78, p. 318, 1932.

[2] R. Feynman, "Plenty of room aat the bottom", in APS Annual Meeting, Caltech, pp. 22–30, 1959.

[3] E. P. Butler, "In situ experiments in the transmission electron microscope", Reports Prog. Phys., vol. 42, no. 5, pp. 833–895, 1979.

[4] T. W. Hansen and J. B. Wagner, Controlled Atmosphere Transmission Electron Microscopy: Principles and Practice. Springer. 2016.

[5] L. de Knoop, "Development of quantitative in - situ transmission electron microscopy for nanoindentation and cold - field emission", University of Toulouse, 2014.

[6] Z. L. Wang, "New developments in transmission electron microscopy for nanotechnology", Advanced Materials, vol. 15, no. 18. WILEY-VCH Verlag, pp. 1497–1514, 2003.

[7] F. M. Ross, "Opportunities and challenges in liquid cell electron microscopy", Science, vol. 350, no. 6267, p. 9886, 2015.

[8] N. Hodnik, G. Dehm, and K. J. J. Mayrhofer, "Importance and challenges of electrochemical in situ liquid cell electron microscopy for energy conversion research", Acc. Chem. Res., vol. 49, no. 9, pp. 2015–2022, 2016.

[9] H. G. Liao, D. Zherebetskyy, H. Xin, C. Czarnik, P. Ercius, H. Elmlund, M. Pan, L. W. Wang, and H. Zheng, "Facet development during platinum nanocube growth", Science, vol. 345, no. 6199, pp. 916–919, 2014.

[10] H. Yoshida, Y. Kuwauchi, J. R. Jinschek, K. Sun, S. Tanaka, M. Kohyama, S. Shimada, M. Haruta, and S. Takeda, "Visualizing gas molecules interacting with supported nanoparticulate catalysts at reaction conditions", Science, vol. 335, no. 6066, pp. 317–319, 2012.

[11] M. E. Holtz, Y. Yu, J. Gao, H. D. Abruña, and D. A. Muller, "Microscopy microanalysis in situ electron energy-eoss spectroscopy in liquids", Microsc.Microanal., vol. 19, pp. 1027–1035, 2013.

[12] M. E. Holtz, Y. Yu, D. Gunceler, J. Gao, R. Sundararaman, K. A. Schwarz, T. A. Arias, H. D. Abruña, and D. A. Muller, “Nanoscale imaging of lithium ion distribution during in situ operation of battery electrode and electrolyte”, Nano Lett., vol. 14, no. 3, pp. 1453–1459, 2014.

[13] E. A. Lewis, S. J. Haigh, T. J. A. Slater, Z. He, M. A. Kulzick, M. G. Burke, and N. J. Zaluzec, “Real-time imaging and local elemental analysis of nanostructures in liquids”, Chem. Commun., vol. 50, no. 70, pp. 10019–10022, 2014.

[14] J. Silcox and M. J. Whelan, “Direct observations of the annealing of prismatic dislocation loops and of climb of dislocations in quenched aluminium”, Philos. Mag., vol. 5, no. 49, pp. 1–23, 1960.

[15] N. Petkov, “In situ real-time TEM reveals growth, transformation and function in one-Dimensional nanoscale materials: from a nanotechnology perspective”, ISRN Nanotechnol., vol. 2013, pp. 1–21, 2013.

[16] C. Y. Wang, F. W. Yuan, Y. C. Hung, Y. W. Su, and H. Y. Tuan, “In-situ TEM and XRD analysis of microstructures changes in solution-grown copper silicide nanowires array for field emitters”, J. Alloys Compd., vol. 735, pp. 2373–2377, 2018.

[17] M. Neklyudova, C. Sabater, A. K. Erdamar, J. M. Van Ruitenbeek, and H. W. Zandbergen, “In situ transmission electron microscope formation of a single-crystalline Bi film on an amorphous substrate”, Appl. Phys. Lett., vol. 110, no. 10, p. 103101, 2017.

[18] Y. Ortega, M. L. Nó, P. Fernández, J. Piqueras, and J. M. San Juan, “In-situ transmission electron microscopy study of melting and diffusion processes at the nanoscale in ZnO nanotubes with Sn cores”, J. Alloys Compd., vol. 744, pp. 421–425, 2018.

[19] I. A. Blech and E. S. Meieran, “Direct transmission electron microscope observation of electrotransport in aluminum thin films”, Appl. Phys. Lett., vol. 11, no. 8, pp. 263–266, 1967.

[20] B. Wang, T. Wang, A. Haque, M. Snure, E. Heller, and N. Glavin, “In-situ TEM study of domain switching in GaN thin films”, Appl. Phys. Lett., vol. 111, no. 11, p. 113103, 2017.

[21] M. Den Hertog, F. Donatini, R. McLeod, E. Monroy, C. Sartel, V. Sallet, and J. Pernot, "In situ biasing and off-axis electron holography of a ZnO nanowire", Nanotechnology, vol. 29, no. 2, p. 25710, 2018.

[22] J. Ayache, L. Beaunier, J. Boumendil, G. Ehret, and D. Laub, Sample preparation handbook for Transmission Electron Microscopy. Springer Verlag, 2010.

[23] M. Hummelgård, "In-situ TEM Probing of Nanomaterials", Mid Sweden University, 2009.

[24] K. Svensson, H. Olin, and E. Olsson, "Nanopipettes for metal transport", Phys. Rev. Lett., vol. 93, no. 14, p. 145901, 2004.

[25] Q. Su, S. Wang, Y. Xiao, L. Yao, G. Du, H. Ye, and Y. Fang, "Lithiation behavior of individual carbon-coated Fe_3O_4 nanowire observed by in situ TEM", J. Phys. Chem. C, vol. 121, no. 6, pp. 3295–3303, 2017.

[26] P. B. Hirsch, R. W. Horne, and M. J. Whelan, "Direct observations of the arrangement and motion of dislocations in aluminium", Philos. Mag., vol. 1, no. 7, pp. 677–684, 1956.

[27] P. R. Swann, C. J. Humphreys, M. J. Goringe, L. E. Thomas, C. G. Shirley, J. S. Lally, and R. M. Fisher, "High voltage electron microscopy", in Proceedings of the Third International Conference, 1974.

[28] J. Pelissier and P. Debrenne, "In situ experiments in the new transmission electron microscopes", Microsc. Microanal. Microstruct., vol. 4, no. 2–3, pp. 111–117, 1993.

[29] H. Bethge, H. L. P Kubin, C. J. Cadek, B. V N Rozhanskii, M. J. Dutkiewicz, K. H. Saka, N. S. Firstov, K. V Schmidt, H. P. Haasen, G. D. Schulze, D. J. Heydenreich, H. G. Thomas, and B. P. B Hirsch, "Electron microscopy in plasticity and fracture research of materials", in Proceedings of the International Symposium held at Holzhau near Dresden, 1989.

[30] J. B. Pethicai, R. Hutchings, and W. C. Oliver, "Hardness measurement at penetration depths as small as 20 nm", Philos. Mag. A, vol. 48, no. 4, pp. 593–606, 1983.

[31] R. A. Bernal, R. Agrawal, B. Peng, K. A. Bertness, N. A. Sanford, A. V. Davydov, and H. D. Espinosa, “Effect of growth orientation and diameter on the elasticity of GaN nanowires. A combined in situ TEM and atomistic modeling investigation”, Nano Lett., vol. 11, no. 2, pp. 548–555, 2011.

[32] B. Peng, M. Locascio, P. Zapol, S. Li, S. L. Mielke, G. C. Schatz, and H. D. Espinosa, “Measurements of near-ultimate strength for multiwalled carbon nanotubes and irradiation-induced crosslinking improvements”, Nat. Nanotechnol., vol. 3, no. 10, pp. 626–631, 2008.

[33] Y. Lu, C. Peng, Y. Ganesan, J. Y. Huang, and J. Lou, “Quantitative in situ TEM tensile testing of an individual nickel nanowire”, Nanotechnology, vol. 22, no. 35, p. 355702, 2011.

[34] D. M. Tang, C. L. Ren, X. Wei, M. S. Wang, C. Liu, Y. Bando, and D. Golberg, “Mechanical properties of bamboo-like boron nitride nanotubes by in situ TEM and MD simulations: Strengthening effect of interlocked joint interfaces”, ACS Nano, vol. 5, no. 9, pp. 7362–7368, 2011.

[35] D.-M. Tang, C.-L. Ren, M.-S. Wang, X. Wei, N. Kawamoto, C. Liu, Y. Bando, M. Mitome, N. Fukata, and D. Golberg, “Mechanical properties of Si nanowires as revealed by in situ transmission wlectron microscopy and molecular dynamics simulations”, Nano Lett., vol. 12, no. 4, pp. 1898–1904, 2012.

[36] I. Lahouij, F. Dassenoy, L. de Knoop, J.-M. Martin, and B. Vacher, “In situ TEM observation of the behavior of an individual fullerene-like MoS_2 nanoparticle in a dynamic Contact”, Tribol. Lett., vol. 42, no. 2, pp. 133–140, 2011.

[37] E. Calvié, L. Joly-Pottuz, C. Esnouf, P. Clément, V. Garnier, J. Chevalier, Y. Jorand, A. Malchère, T. Epicier, and K. Masenelli-Varlot, “Real time TEM observation of alumina ceramic nano-particles during compression”, J. Eur. Ceram. Soc., vol. 32, no. 10, pp. 2067–2071, 2012.

[38] M. S. Wang, D. Golberg, and Y. Bando, “Tensile tests on individual single-walled carbon nanotubes: Linking nanotube strength with its defects”, Adv. Mater., vol. 22, no. 36, pp. 4071–4075, 2010.

[39] X. Wei, M.-S. Wang, Y. Bando, and D. Golberg, “Tensile Tests on Individual Multi-Walled Boron Nitride Nanotubes”, Adv. Mater., vol. 22, no. 43, pp. 4895–4899, 2010.

[40] B. Ozdol, C. Gammer, L. J. Zeng, S. Bhowmick, T. K. Nordqvist, P. Krogstrup, A. M. Minor, U. Dahmen, E. Olsson, and W. Jaeger, “Exploring the structural and electronic properties of nanowires at their mechanical limits”, Microsc. Microanal., vol. 23, no. S1, pp. 1520–1521, 2017.

[41] J. C. Yang and G. Zhou, “In situ ultra-high vacuum transmission electron microscopy studies of the transient oxidation stage of Cu and Cu alloy thin films”, Micron, vol. 43, no. 11, pp. 1195–1210, 2012.

[42] R. Sharma, “Design and applications of environmental cell transmission electron microscope for in situ observations of gas-solid reactions”, Microsc. Microanal., vol. 7, no. 6, pp. 494–506, 2001.

[43] F. M. Ross, “Controlling nanowire structures through real time growth studies”, Reports Prog. Phys., vol. 73, no. 11, p. 114501, 2010.

[44] P. A. Crozier, “The fundamental role of in situ electron microscopy in catalytic science”, in Microscopy and Microanalysis, vol. 12, no. SUPPL. 2, pp. 768–769, 2006.

[45] J. B. Wagner, F. Cavalca, C. D. Damsgaard, L. D. L. Duchstein, and T. W. Hansen, “Exploring the environmental transmission electron microscope”, Micron, vol. 43, no. 11, pp. 1169–1175, 2012.

[46] J. F. Creemer, S. Helveg, G. H. Hoveling, S. Ullmann, A. M. Molenbroek, P. M. Sarro, and H. W. Zandbergen, “Atomic-scale electron microscopy at ambient pressure”, Ultramicroscopy, vol. 108, no. 9, pp. 993–998, 2008.

[47] L. Marton, “La microscopie electronique des objects biologiques”, Bull. Acad. Roy. Méd. Belg., vol. 20, no. 5, pp. 439–446, 1934.

[48] L. Marton, “Electron microscopy of biological objects”, nature, vol. 133, no. 3372, pp. 911–911, 1934.

[49] E. D. Boyes and P. L. Gai, “Environmental high resolution electron microscopy and applications to chemical science”, Ultramicroscopy, vol. 67, no. 1–4, pp. 219–232, 1997.

[50] R. T. K. Baker and P. S. Harris, “Controlled atmosphere electron microscopy”, J. Phys. E., vol. 5, no. 8, pp. 793–797, 1972.

[51] E. P. Butler and K. F. Hale, “Dynamic experiments in the electron microscope”, Practical Methods in Electron Microscopy volume 9. North-Holland Pub. Co., p. 457, 1981.

[52] I. M. Robertson and D. Teter, “Controlled environment transmission electron microscopy”, Microsc. Res. Tech., vol. 42, no. 4, pp. 260–269, 1998.

[53] T. L. Daulton, B. J. Little, K. Lowe, and J. Jones-meehan, “In situ environmental cell – transmission electron microscopy study of microbial reduction of chromium (VI) using electron energy loss spectroscopy”, Microscopy Microanalysis, vol. 7, no. Vi, pp. 470–485, 2001.

[54] H. G. Heide, “Electron microscopic observation of specimens under controlled gas pressure.”, J. Cell Biol., vol. 13, no. 1, pp. 147–152, 1962.

[55] M. Komatsu and H. Mori, “In situ HVEM study on copper oxidation using an improved environmental cell”, J. Electron Microsc. (Tokyo)., vol. 54, no. 2, pp. 99–107, 2005.

[56] G. M. Parkinson, “High resolution, in-situ controlled atmosphere transmission electron microscopy (CATEM) of heterogeneous catalysts”, Catal. Letters, vol. 2, no. 5, pp. 303–307, 1989.

[57] S. J. Pennycook, “Study of supported ruthenium catalysts by STEM”, J. Microsc., vol. 124, no. 1, pp. 15–22, 1981.

[58] A. Howie, L. D. Marks, and S. J. Pennycook, “New imaging methods for catalyst particles”, Ultramicroscopy, vol. 8, no. 1–2, pp. 163–174, 1982.

[59] N. de Jonge, W. C. Bigelow, and G. M. Veith, “Atmospheric pressure scanning transmission electron microscopy”, Nano Lett., vol. 10, no. 3, pp. 1028–1031, 2010.

[60] J. P. Winterstein, P. A. Lin, and R. Sharma, “Temperature calibration for in situ environmental transmission electron microscopy experiments”, Microsc. Microanal., vol. 21, no. 6, pp. 1622–1628, 2015.

[61] J. F. Creemer, S. Helveg, G. H. Hoveling, S. Ullmann, A. M. Molenbroek, P. M. Sarro, and H. W. Zandbergen, "Atomic-scale electron microscopy at ambient pressure", Ultramicroscopy, vol. 108, no. 9, pp. 993–998, 2008.

[62] Y. Li, D. Zakharov, S. Zhao, R. Tappero, U. Jung, A. Elsen, P. Baumann, R. G. Nuzzo, E. A. Stach, and A. I. Frenkel, "Complex structural dynamics of nanocatalysts revealed in Operando conditions by correlated imaging and spectroscopy probes", Nat. Commun., vol. 6, no. 1, p. 7583, 2015.

[63] E. Ruska, "Beitrag zur uebermikroskopischen Abbildungen bei hoeheren Drucken", Kolloid Zeitschrift, vol. 100, pp. 212–219, 1942.

[64] I. M. Abrams and J. W. McBain, "A closed cell for electron microscopy", J. Appl. Phys., vol. 15, no. 8, pp. 607–609, 1944.

[65] M. J. Williamson, R. M. Tromp, P. M. Vereecken, R. Hull, and F. M. Ross, "Dynamic microscopy of nanoscale cluster growth at the solid-liquid interface", Nature Materials, vol. 2, no. 8. Nature Publishing Group, pp. 532–536, 2003.

[66] N. de Jonge, D. B. Peckys, G. J. Kremers, and D. W. Piston, "Electron microscopy of whole cells in liquid with nanometer resolution", Proc. Natl. Acad. Sci. U. S. A., vol. 106, no. 7, pp. 2159–2164, 2009.

[67] H. Zheng, R. K. Smith, Y. W. Jun, C. Kisielowski, U. Dahmen, and A. Paul Alivisatos, "Observation of single colloidal platinum nanocrystal growth trajectories", Science, vol. 324, no. 5932, pp. 1309–1312, 2009.

[68] F. M. Ross, Liquid Cell Electron Microscopy. Cambridge University Press, 2017.

[69] U. M. Mirsaidov, H. Zheng, D. Bhattacharya, Y. Casana, and P. Matsudaira, "Direct observation of stick-slip movements of water nanodroplets induced by an electron beam", Proc. Natl. Acad. Sci., vol. 109, no. 19, pp. 7187–7190, 2012.

[70] S. W. Chee, S. H. Pratt, K. Hattar, D. Duquette, F. M. Ross, and R. Hull, "Studying localized corrosion using liquid cell transmission electron microscopy", Chem. Commun., vol. 51, no. 1, pp. 168–171, 2015.

[71] M. H. Nielsen, S. Aloni, and J. J. De Yoreo, “In situ TEM imaging of $CaCO_3$ nucleation reveals coexistence of direct and indirect pathways”, Science, vol. 345, no. 6201, pp. 1158–1162, 2014.

[72] N. Liv, D. S. B. van Oosten Slingeland, J.-P. Baudoin, P. Kruit, D. W. Piston, and J. P. Hoogenboom, “Electron microscopy of living cells during in situ fluorescence microscopy”, ACS Nano, vol. 10, no. 1, pp. 265–273, 2016.

[73] K. Hirano, T. Kinoshita, T. Uemura, H. Motohashi, Y. Watanabe, T. Ebihara, H. Nishiyama, M. Sato, M. Suga, Y. Maruyama, N. M. Tsuji, M. Yamamoto, S. Nishihara, and C. Sato, “Electron microscopy of primary cell cultures in solution and correlative optical microscopy using ASEM”, Ultramicroscopy, vol. 143, pp. 52–66, 2014.

[74] E. Kennedy, E. M. Nelson, T. Tanaka, J. Damiano, and G. Timp, “Live bacterial physiology visualized with 5 nm resolution using scanning transmission electron microscopy”, ACS Nano, vol. 10, no. 2, pp. 2669–2677, 2016.

[75] D. B. Peckys, M. J. Dukes, E. a. Ring, D. W. Piston, and N. de Jonge, “Imaging specific protein labels on eukaryotic cells in liquid with scanning transmission electron microscopy”, Micros. Today, vol. 19, no. 5, pp. 16–20, 2011.

[76] M. J. Dukes, B. L. Gilmore, J. R. Tanner, S. M. McDonald, and D. F. Kelly, “In situ TEM of biological assemblies in liquid.”, J. Vis. Exp., no. 82, p. 50936, 2013.

[77] B. L. Gilmore, S. P. Showalter, M. J. Dukes, J. R. Tanner, A. C. Demmert, S. M. McDonald, and D. F. Kelly, “Visualizing viral assemblies in a nanoscale biosphere”, Lab Chip, vol. 13, no. 2, pp. 216–219, 2013.

[78] Q. Chen, J. M. Smith, J. Park, K. Kim, D. Ho, H. I. Rasool, A. Zettl, and A. P. Alivisatos, “3D motion of DNA-Au nanoconjugates in graphene liquid cell electron microscopy”, Nano Lett., vol. 13, no. 9, pp. 4556–4561, 2013.

[79] J. Park, H. Park, P. Ercius, A. F. Pegoraro, C. Xu, J. W. Kim, S. H. Han, and D. A. Weitz, “Direct observation of wet biological samples by graphene

liquid cell transmission electron microscopy", Nano Lett., vol. 15, no. 7, pp. 4737–4744, 2015.

[80] D. B. Peckys, U. Korf, S. Wiemann, and N. de Jonge, "Liquid-phase electron microscopy of molecular drug response in breast cancer cells reveals irresponsive cell subpopulations related to lack of HER2 homodimers", Mol. Biol. Cell, vol. 28, no. 23, pp. 3193–3202, 2017.

[81] M. J. Williamson, R. M Tromp, P. M. Vereecken, R. Hull, F. M. Ross, "Dynamic microscopy of nanoscale cluster growth at the solid-liquid interface", Nature Materials., vol. 2, no. 8, pp. 532-536, 2003.

[82] S. Kodambaka, J. Tersoff, M. C. Reuter, F. M. Ross, "Dynamic microscopy of nanoscale cluster growth at the solid-liquid interface", Nature Materials., vol. 2, no. 8, pp. 532-536, 2003.

[83] G. M. Bremmer, E. Zacharaki, A. O. Sjåstad, V. Navarro, J. W. M. Frenken, and P. J. Kooyman, "In situ TEM observation of the Boudouard reaction: multi-layered graphene formation from CO on cobalt nanoparticles at atmospheric pressure", Faraday Discuss., vol. 197, no. 0, pp. 337–351, 2017.

[84] P. Liu, J. Han, X. Guo, Y. Ito, C. Yang, S. Ning, T. Fujita, A. Hirata, and M. Chen, "Operando characterization of cathodic reactions in a liquid-state lithium-oxygen micro-battery by scanning transmission electron microscopy", Sci. Rep., vol. 8, no. 1, p. 3134, 2018.

Chapter 2

Instrumental

In this chapter, the TEM-STM holder used in this thesis is described. Also, the specific sample preparation processes for *in-situ* TEM-STM experiments are presented. First, for nanostructured samples different preparation solutions are addressed depending on the sample support. Then, for localized preparation of devices or thin films, Focused Ion Beam (FIB) assisted preparation is shown, pointing out the special necessities for *in-situ* preparation. Finally, the improvements on the TEM-STM holder carried out to ensure the repeatability of the experiments, as well as the calibration of the measurement system are also included.

2.1 TEM-STM holder

The TEM-STM holder used in the context of this thesis is a commercial *in-situ* TEM sample holder, manufactured by Nanofactory Instruments AB[1]. This holder is designed for the electrical probing of individual nanostructures by using an STM probe that can be moved along the x,y and z directions inside the TEM.

The TEM-STM holder is presentend in figure 2.1 (a). It consists of three main parts, the end-piece (with the connectors), the rod and the front-piece. The front-piece is at the end of the holder limited by the O-ring and contains the nanomanipulator and the sample. Figure 2.1 (b) shows a magnified image of the front-piece. As can be seen in the figure, the platinum tip (2), used as a STM probe, is placed on the right-hand side and a wire (1), used as a sample support, on the left-hand side. A sapphire ball (4) is supported by a piezotube to drive the hat (3), the only moving part in the holder, where the STM tip is placed. This system allows both fine and coarse movements of the tip in x, y and z, enabling the selection of specific nanostructures placed in the sample support [1].

As can be seen in figure 2.2, the whole TEM-STM system consists of the following parts: the controller (1), the preamplifier (2), the holder (3) and the computer (4) with the software system.

It is very important that the TEM-STM system is correctly grounded, and also that it has a low impedance path to the TEM ground, since the tip inside the holder is exposed to the e-beam inside the TEM and, to prevent charging effects, it is necessary to have a return path for the electrons back to TEM ground.

[1] Nanofactory went bankrupt in 2013, was purchased by FEI (now Thermo Fisher Scientific) and the technical service was discontinued. Maintenance and improvements are, thus, home-made.

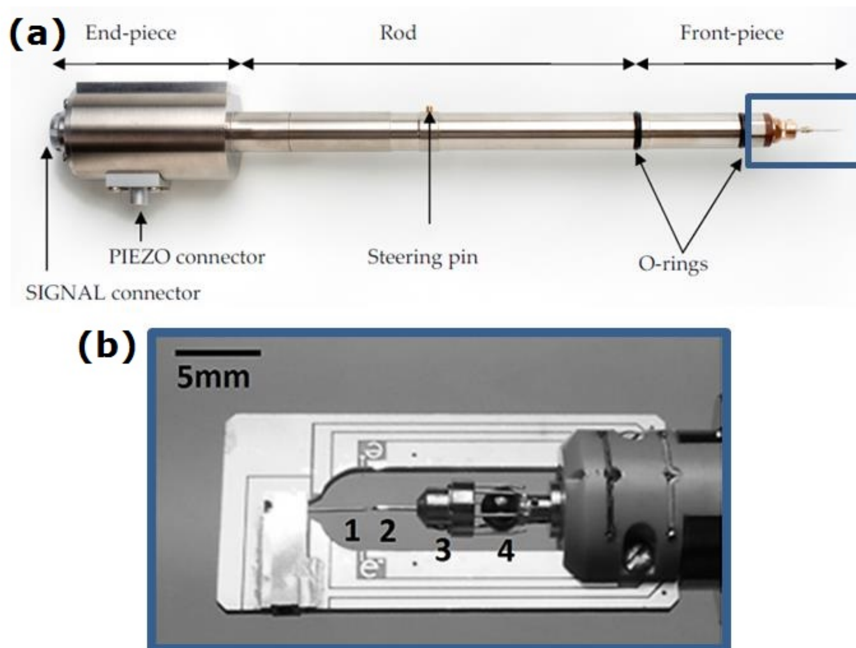

Figure 2.1 (a) TEM-STM holder for JEOL microscopes. (b) Front-piece of the TEM-STM showing the most important parts: the platinum wire used as a sample support (1); the STM movable tip (2); the hat (3) and the sapphire ball (4).

The software Nanofactory Instruments 3 (NF3) is used to control the movement of the piezo and to record the outputs, such as the measured current. Figure 2.3 shows the interface of the NF3. As shown in Figure 2.3 (b), the NF3 allows the control of the movement of the STM probe using a gaming pad.

The TEM-STM system has a wide variety of applications. First, the system can be used for measuring the electrical properties at specific locations of the sample and associate them with the TEM images. The applied bias range is ± 10 V and the measurement noise is around 1 nA. Figure 2.3 (c) shows the results of an I-V characteristic measured with the NF3 software.

Second, the TEM-STM system can also be used as a conventional STM and perform topographical images of the nanostructure. In this

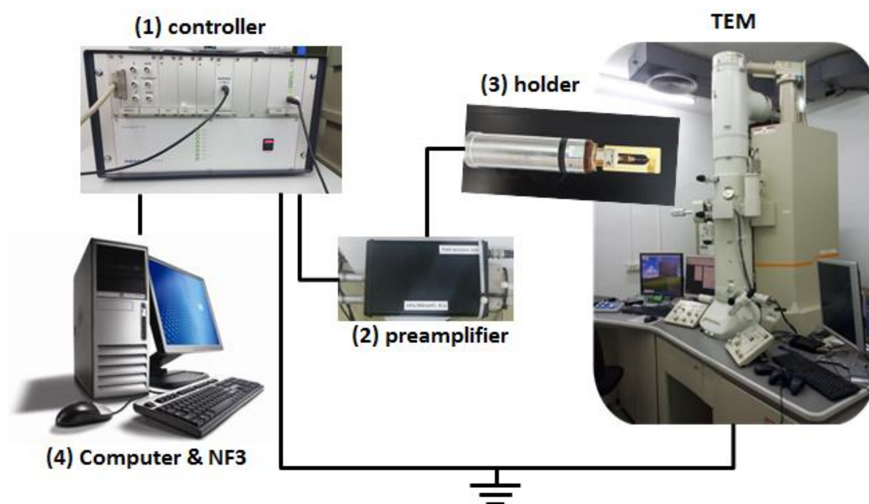

Figure 2.2 Parts of the TEM-STM system composed by: the controller (1), the preamplifier (2), the holder (3) and the computer (4) with the software system.

method, the image is built up by employing the phenomenon of electron tunneling to get a current to pass between the electrically conductive sample and the sharp metal tip. A specific current is fixed and the system adjusts the tip position via a feedback loop to maintain this constant current while the sample surface is scanned. This process keeps the tip at a constant distance to the surface and the current information related to the X and Y position of the scanner builds up a topographical map of the scanned area.

All the *in-situ* experiments in the present thesis were performed using this TEM-STM holder from Nanofactory working with both a JEOL 2100 and a JEOL 2010F TEM operating at 200 kV.

2.2 Sample preparation

For TEM-STM experiments both the sample and the STM tip have to be placed orthogonally with respect to the electron beam for imaging,

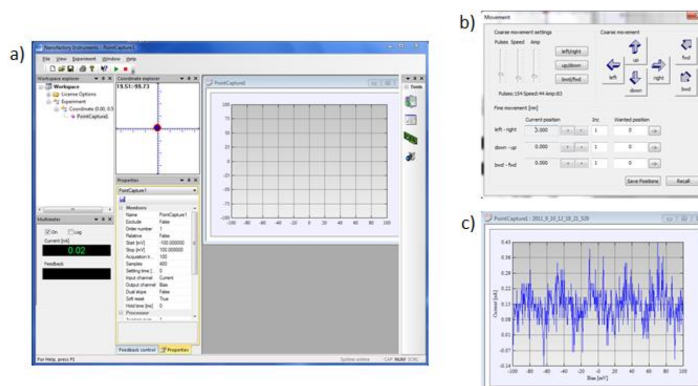

Figure 2.3 Screenshots of the Nanofactory Instruments 3 (NF3) software showing (a) the main interface, (b) the movement controller and (c) the results of an I-V characteristic.

while also keeping the electron transparent part of the TEM sample accessible to the STM tip. A successful sample preparation is then a critical step previous to any electrical measurement.

In the case of nanostructured materials, this is relatively easy to accomplish, but in the case of thin layer structures of nanodevices, localized sample preparation is a must. In the following, the main aspects of sample preparation procedures are described.

2.2.1 Nanostructured materials

Figure 2.4 summarizes the two different approaches used to prepare the samples for *in-situ* TEM experiments in the case of nanostructured materials, depending on the sample support used: a wire or a grid.

For *in-situ* TEM-STM applications, a wire is typically used as a support[2] of nanostructured samples. A similar type of wire as the one used for the STM tip is used for the specimen but placed at the opposite end in the holder (see figure 2.5).

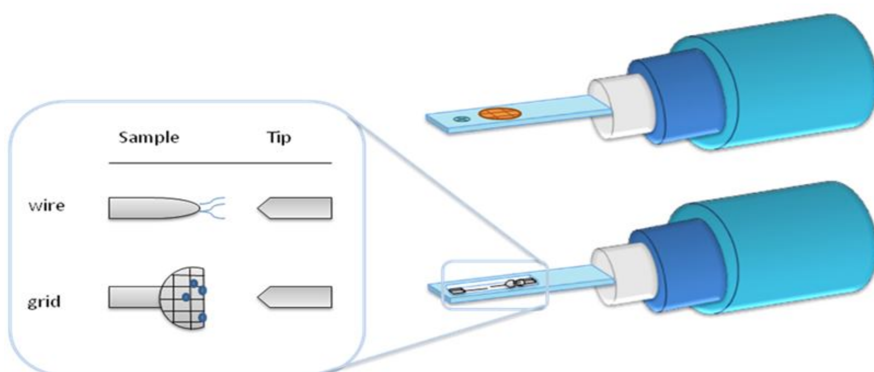

Figure 2.4 Schematic of a conventional TEM holder, TEM-STM holder, and samples prepared for *in-situ* probing.

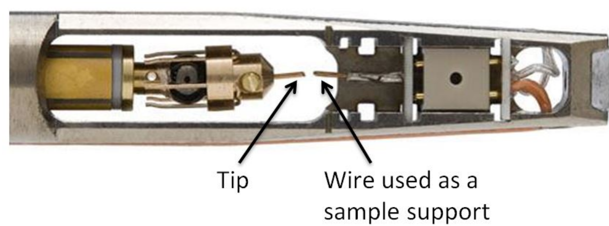

Figure 2.5 TEM-STM holder using a wire as a sample support.

To prepare the wire for the TEM-STM experiments manually, a conductive wire (e.g. copper, gold or platinum) is stretched with the aid of pliers at 45° to elongate it by its plasticity to the point of breakage and achieve an end as sharp as possible.

For nanostructured samples, once a wire with a thin end is obtained, two strategies can be considered:

- Scratching the layer that contains the nanostructures and assuming the surface adhesion will keep the nanostructures in place (figure 2.6 shows a TEM image of the tip contacting a nanowire attached to a gold wire using this strategy).

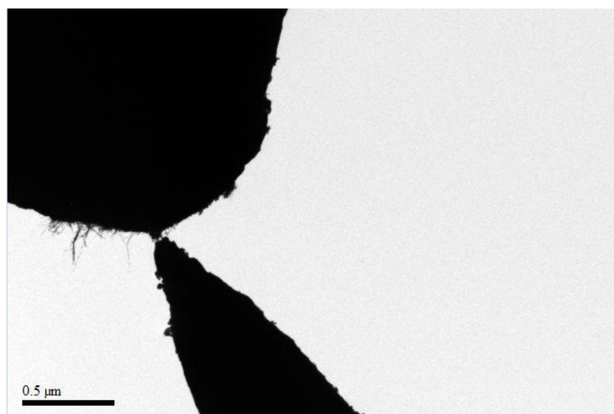

Figure 2.6 TEM image of the tip contacting the nanowires attached to a gold wire used as a support.

- Gluing the nanostructures directly to the wire with a conductive epoxy.

Although attaching the nanostructures to the wire is very useful for the *in-situ* TEM-STM system, it does not allow a subsequent observation of the same sample using other kinds of TEM holders (e.g. analytical, double-tilt...). A solution is to use a conventional copper grid attached to a wire as a sample support (see figure 2.4).

Thus, to use conventional copper grids as a sample support with the TEM-STM holder the grid is pasted to a suitable copper wire with a conductive epoxy. Then, to assure a good behavior of the epoxy, the grid-and-wire support is annealed in the oven for 10 minutes at 120°C (Figure 2.7). Once the grid is well attached to the wire, the nanostructures can be deposited. One drop of solution is applied to the grid and left to dry (depending on the solvent this may take from a few minutes to several hours).

As a final step, to use conventional TEM grids for the TEM-STM system, they should be cut in half in order to let the tip access the sample. Now, the sample is ready to be inserted into the holder to start the measurements (Figure 2.8).

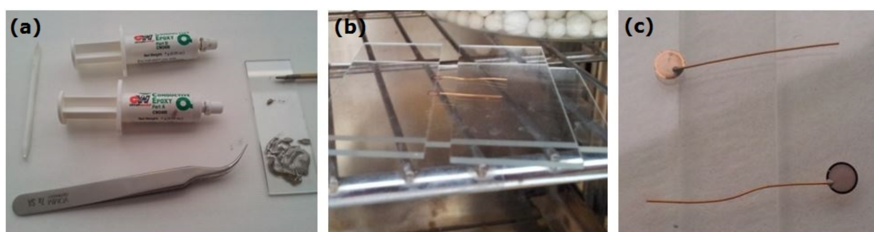

Figure 2.7 (a) Tools used for sample preparation, (b) image of samples in the oven, (c) image of samples before cutting.

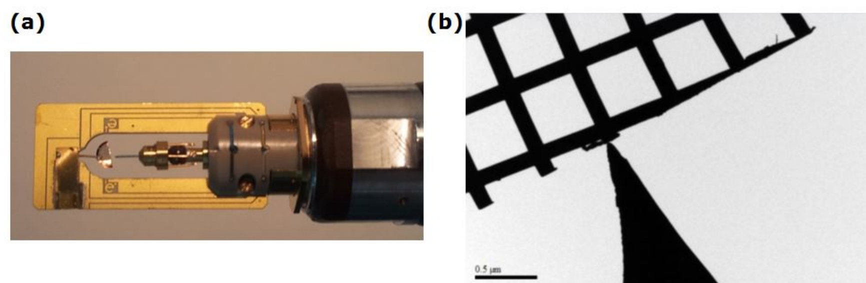

Figure 2.8 (a) Image of the TEM-STM holder with a copper grid as a sample support. (b) TEM image of the tip contacting graphene using a copper grid as a support.

2.2.2 Localized preparation

In the case of samples that are not electrotransparent *per se* (e.g. bulk samples, thin films, single devices) more sophisticated preparation methods are needed. In particular, for localized preparation, Focused Ion Beam (FIB) is the method of choice.

A typical FIB lamella preparation goes as follows. Once a region of interest is located in the sample, a platinum strip is deposited to protect this region. Electron or ion beam induced Pt deposition is achieved by decomposition of the molecules of a metalorganic gas precursor inserted in the chamber when the beam scans the selected region. Then, two deep trenches, keeping the Pt strip between both cuts, are milled at high ion current (figure 2.9 (a)). The different cuts are milled

at medium ion current in order to leave the lamella attached only on one side (figure 2.9(b)). The next step is the lift-out and consists in the extraction of the lamella, and its subsequent manipulation to bring it to the TEM grid. The lamella is then attached to the grid via Pt deposition (figure 2.9(c)). Particular TEM grids need to be used as a support for the lamellas prepared by FIB using the lift-out technique. Figure 2.10(a) shows a typical Omniprobe[2] copper grid. These grids include multiple indexed mounting locations, with both vertical bar (figure 2.10 (b)) and V-shaped attachment surfaces (figure 2.10(c)).

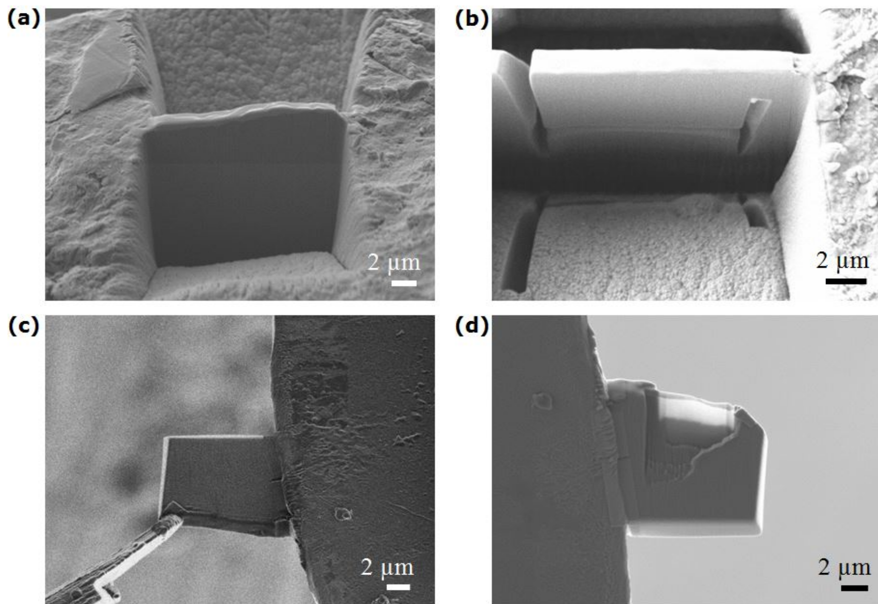

Figure 2.9 SEM images acquired during a TEM lamella preparation by FIB using the lift-out technique. (a) Trenches milled by FIB, (b) lamella attached to bulk sample by one side only and ready for the lift-out, (c) lamella attached to the TEM grid via Pt deposition, (d) TEM lamella thinned enough for electrotransparency.

Finally, the last step of a conventional lamella preparation corresponds to the final thinning and cleaning of the sample. This step consists in scanning each lateral face of the lamella by FIB at low

[2]Omniprobe Inc., acquired by Oxford Instruments in 2011.

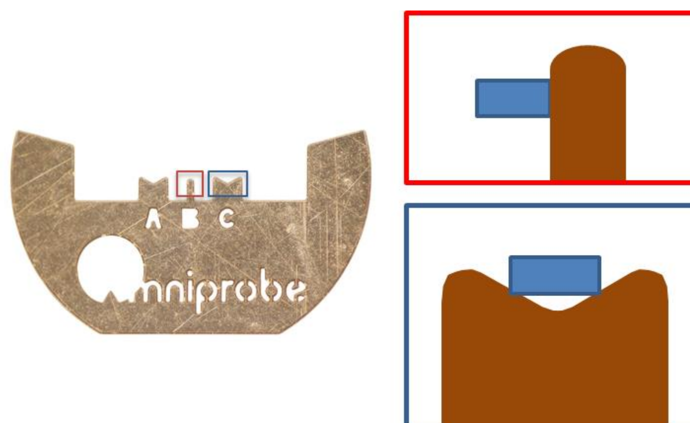

Figure 2.10 (a) Copper TEM grid manufactured by Omniprobe Inc. for TEM lamella preparation by FIB, (b) vertical post and V-shaped post for lamella location.

voltage and low current, polishing it until the lamella is thin enough for electrotransparency (∼50nm) (figure 2.9 (d)).

Figure 2.11 (a) and (b) depict the TEM-STM holder with a FIB grid used as a sample support. Although TEM sample preparation by FIB is nowadays considered a routine procedure[3,4], the lamella preparation for *in-situ* experiments with the TEM-STM system requires an additional step. The lamella not only has to be transparent to electrons, but also has to be well connected for electrical probing. Thus, two cuts are carefully made by milling with FIB in the sides of the electrotransparent part of the lamella, cutting off the current paths between the top Pt protection and the TEM grid. As can be seen in figure 2.11 (b), without these cuts the current would flow through the Pt protections deposited by FIB from the movable tip to the TEM grid, avoiding the interesting zones of the sample (as they are less conductive). Figure 2.11 (c) shows how the cuts are milled in the lamella (highlighted with red arrows) in order to avoid these short-circuits and allow the flow of current through the layers of the sample. Special attention has to be paid also in order to avoid redeposition of the milling material containing some Pt amount.

Finally, as for conventional copper TEM grids in the sample preparation of nanostructured materials, the grid has to be attached to a wire in order to insert it into the holder.

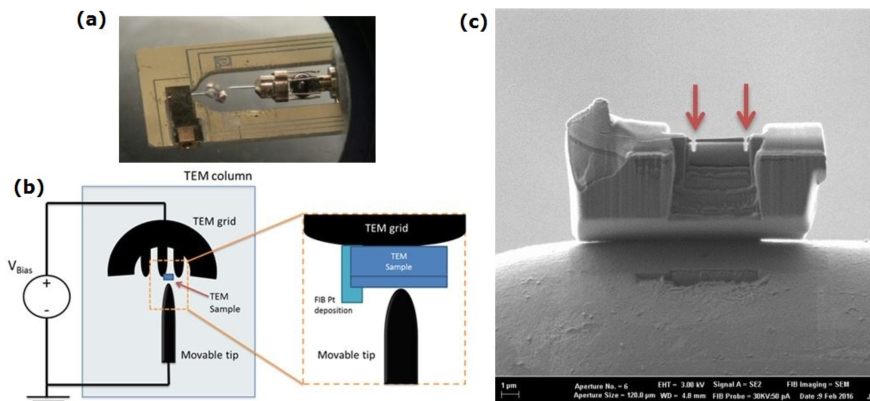

Figure 2.11 (a) Image and (b) schematic of the TEM-STM holder with a copper grid for FIB sample preparation as a sample support. (c) Lamella with additional lateral millings in order to avoid short-circuits for *in-situ* electrical measurements.

Instead of a special FIB grid (quite expensive), a wire can be also used as a lamella support. We have developed a FIB approach to attach the lamella directly to a wire, in order to use it as a sample support in the TEM-STM system. In this method, the wire has to be prepared for this purpose. First, the end of the wire has to be milled in order to achieve a stable location for the lamella (see figure 2.12(a)). After that, the lift-out technique can be carried out as usual, attaching the lamella at the top of the wire via Pt deposition. Figure 2.12(b) shows a top-view SEM image of the TEM lamella attached to the tip.

2.3 TEM-STM holder improvements: a gridcase

In the previous sections different methods to prepare samples for *in-situ* experiments on a copper grid have been described. In all cases,

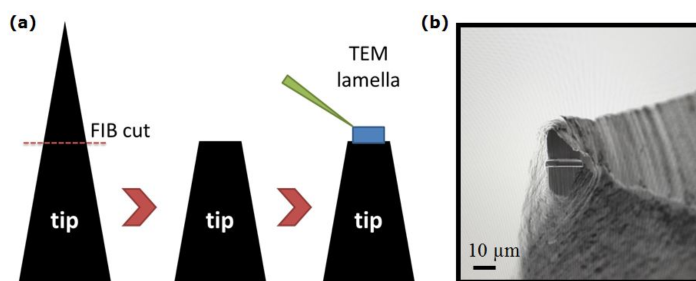

Figure 2.12 (a) FIB procedure to prepare TEM lamellas on a tip as a sample support, (b) top-view SEM image of a lamella attached to a platinum tip.

the step of gluing the grid to a wire used as a support is required. Nevertheless, to attach the grid to the wire with a conductive epoxy is not always bound to produce good results. First of all, this connection involves ohmic contacts introducing errors in the electrical resistance measurements. Secondly, sometimes this attachment is not good enough to resist large tensions. Also, the sample can be contaminated by the epoxy and, finally, if we want to observe the sample with other TEM holders, the specimen can be damaged at the moment of separating the wire from the grid.

In order to overcome these disadvantages and assure a good repeatability of the experiments, a gridcase that allows inserting a TEM grid on one side and a wire on the other side has been designed and built in the context of the present thesis. Figure 2.13 shows the gridcase design.

As can be seen in figure 2.13, the wire, which can be introduced in the TEM-STM holder, is held on the left-hand side of the gridcase (labelled as A in the figure) and the TEM grid, where the lamella is attached, is held on the right-hand side of the gridcase (labelled as B in the figure), and both are screwed into place. This way, both the wire and the grid can be easily replaced. Moreover, the gridcase

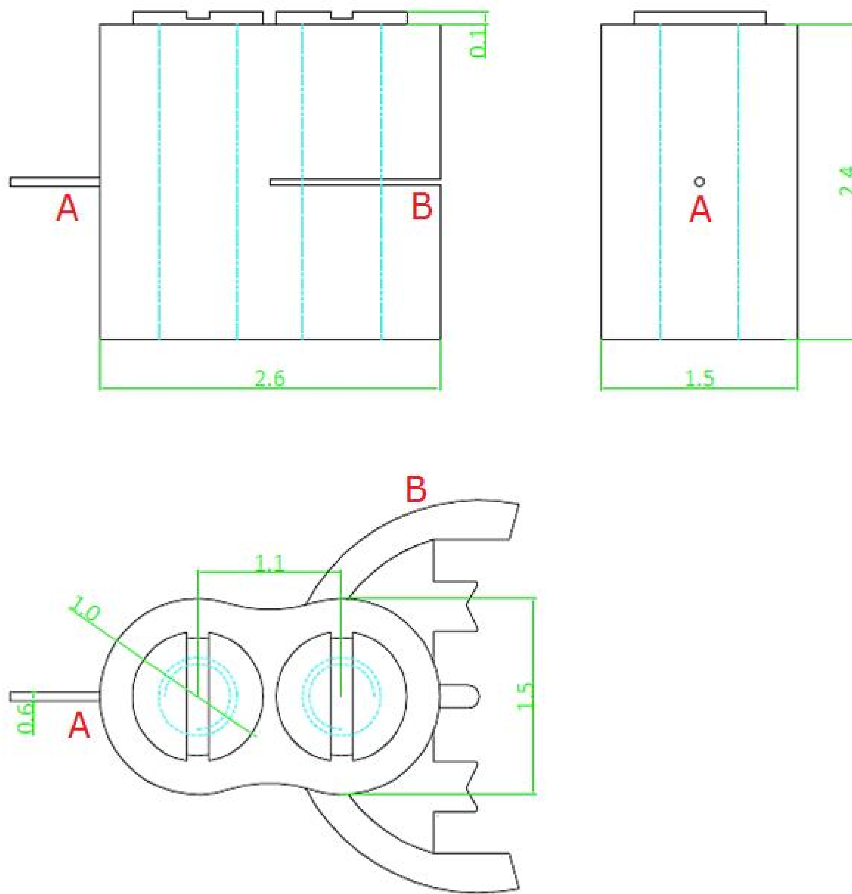

Figure 2.13 From left to right and top to bottom, the side view, front view and top view of the gridcase (dimensions in mm). Labelled as A and B, the places where the wire and the TEM grid have to be inserted in, respectively.

has been fabricated with platinum in order to assure good electrical conductivity through the grid-gridcase-wire system.

In addition, as mentioned in the previous chapter, one of the most important challenges when building *in-situ* TEM instruments is the lack of space due to the situation in the polar pieces. In order to ensure the security using our gridcase, avoiding contact with the polar pieces of the TEM, the inside of the column was observed while the

improved holder was introduced and rotated. Figure 2.14 (a) depicts the configuration for this preliminary observation. 2.14 (b) shows the *in-situ* holder with the gridcase between the polar pieces.

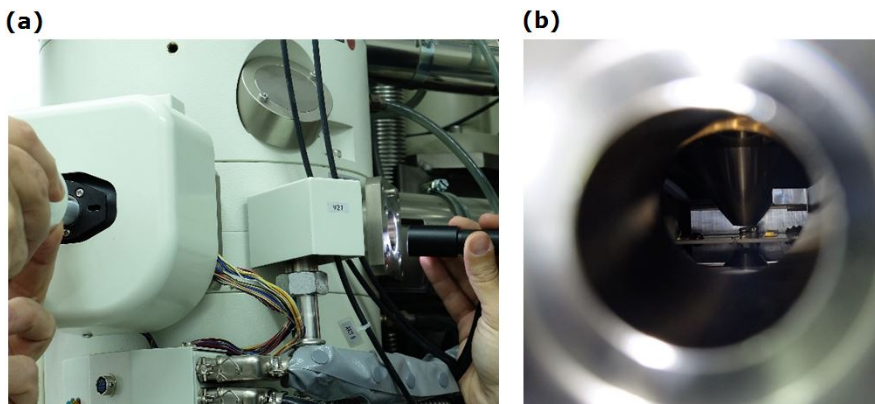

Figure 2.14 (a) Configuration for the observation of the gridcase in the TEM. (b) Image of the *in-situ* holder with the gridcase between the polar pieces.

The fabrication of a homemade gridcase for using a TEM grid as a sample support in the TEM-STM system offers a greater versatility in the experiments since it is possible to combine the capabilities of this system with other holders for conventional TEM observation, while reducing the measurement errors and improving the repeatability of the experiments. Figure 2.15 shows a picture of the TEM-STM holder with the homemade gridcase using a Omniprobe copper grid as a sample support.

2.4 TEM-STM system calibration

In order to ensure the accuracy and consistency of the measurements made with the TEM-STM system, a calibration has been carried out. For this, commercial resistors were used as a reference. In particular, different resistors from 0,01 kΩ to 20 kΩ with a 5% tolerance were measured with three different approaches:

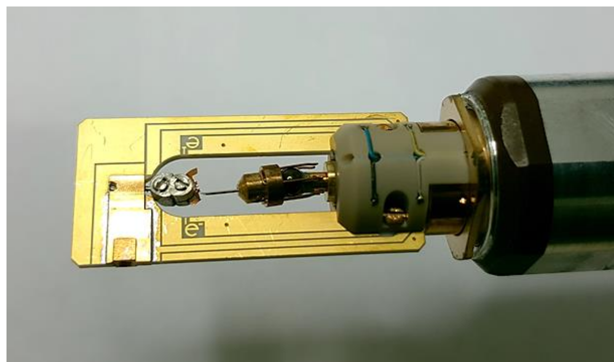

Figure 2.15 TEM-STM holder using the gridcase as a sample support.

(a) With a commercial multimeter (KAISE Digital Multimeter MAS830L). These resistance measurements will be called R_1.

(b) With the TEM-STM system avoiding the contact effects of the movable tip, using a protoboard and external connections, assuring a perfect contact between the components (see figure 2.16 (a)). A ramp from -100 mV to 100 mV, with 400 sampling points and an acquisition time of 100 ms for the entire ramp was used to measure the resistance. It will be called R_2.

(c) Finally, with the TEM-STM system as operated taking into account the contact effects of the movable tip. In this approach the STM tip was moved to the resistor with the NF3 Software until the electrical contact occurred (see figure 2.16 (b)). A ramp from -100 mV to 100 mV, with 400 sampling points and an acquisition time of 100 ms for the entire ramp was used to measure the resistance. It will be called R_3.

Results are summarized in table 2.1, showing the nominal values of the resistors, the average values of the resistances measured and the relative errors (ε) for each approach.

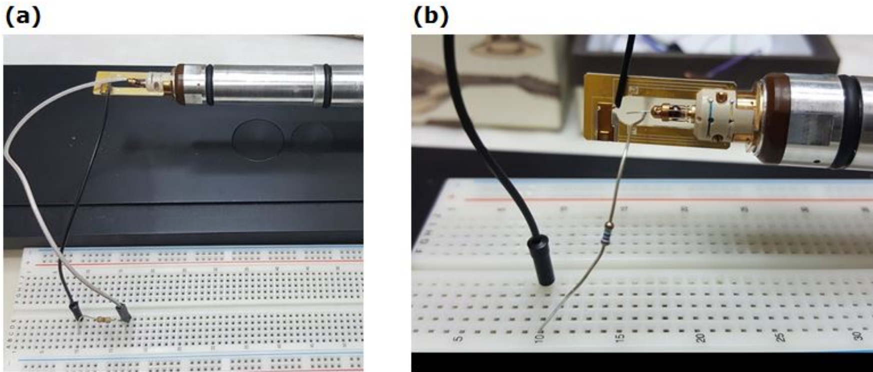

Figure 2.16 Procedure used for the calibration of the system (a) avoiding the contact effects of the movable tip and (b) taking into account the contact effects of the movable tip.

$R_n(k\Omega)$	$\bar{R}_1(k\Omega)$	$\bar{R}_2(k\Omega)$	$\bar{R}_3(k\Omega)$	ε_1	ε_2	ε_3
0.01	0.013±0.001	0.049±0.001	0.035±0.001	0.3	3.9	2.5
0.1	0.011±0.001	0.124±0.001	0.116±0.001	0.01	0.24	0.16
0.2	0.217±0.001	0.237±0.001	0.235±0.001	0.09	0.19	0.18
0.5	0.467±0.001	0.482±0.001	0.484±0.001	0.07	0.04	0.03
1	0.994±0.001	1.022±0.001	1.032±0.001	0.01	0.02	0.03
2	1.971±0.001	2.04±0.06	2.013±0.001	0.02	0.02	0.01
10	9.89±0.01	9.897±0.001	9.91±0.01	0.01	0.01	0.01
20	19.77±0.01	20.165±0.005	20.07±0.01	0.01	0.01	0.01

Table 2.1 Nominal values of the resistors, average values of the resistances measured and relative errors for each approach.

A graphical account of the results of table 2.1 is given in figure 2.17. These results show low errors and a good repeatability in the TEM-STM system measure for resistances above 0.5 $k\Omega$, obtaining even, in some cases, lower errors than for the commercial multimeter. For resistances below 0.5 $k\Omega$, the error in the measurement increases, since the resistance of the system itself is not negligible. Therefore, for small resistances, a deeper analysis of the measure is needed. In this case, the resistance measured is given by

$$R_T = R_{sample} + R_{tips} + R_{eq} \tag{2.1}$$

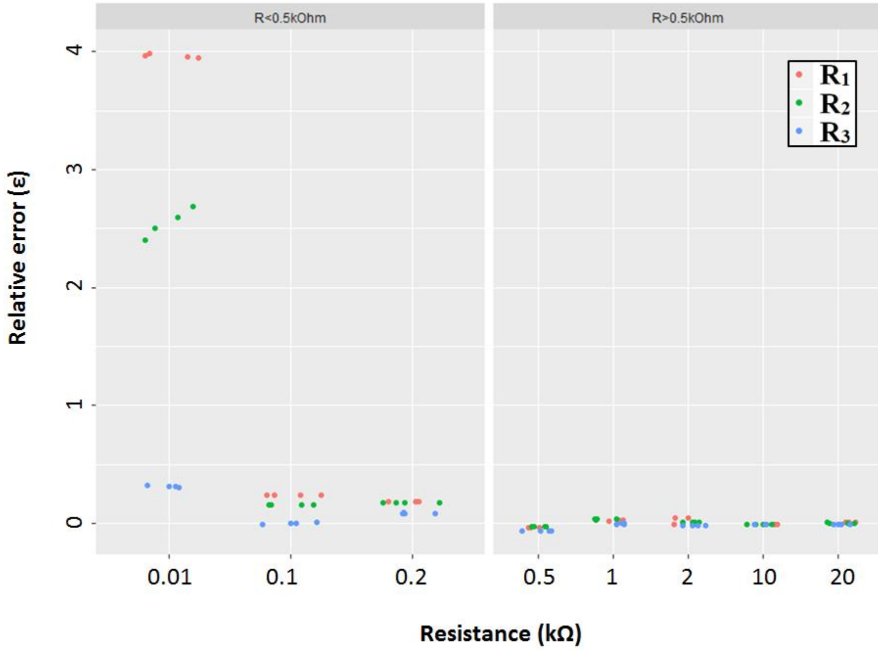

Figure 2.17 Graphical account of the results of table 2.1, showing the relative errors of the measurements for each resistor for the three different approaches: R_1 corresponds to measurements made with a commercial multimeter, R_2, to measurements made using the TEM-STM system with a protoboard and wire connections and R_3, to measurements made using the TEM-STM system as usually operated.

The resistance measured is not only the resistance of the sample, it is the direct sum of the resistance of the sample (R_{sample}), the tips (R_{tips}) and the rest of the measurement system (R_{eq}) (equation 2.1), in series of course (see figure 2.18).

Moreover, for resistances above 0.5 $k\Omega$ the results with and without taking into account the contact effects of the movable tip are similar. This result demonstrates that the effect of the movable tip contact is negligible. In the literature, the Olsson group determined that the contact resistivity between the tip and a rGO sheet is 2 x $10^{-6}\Omega cm^2$ [5].

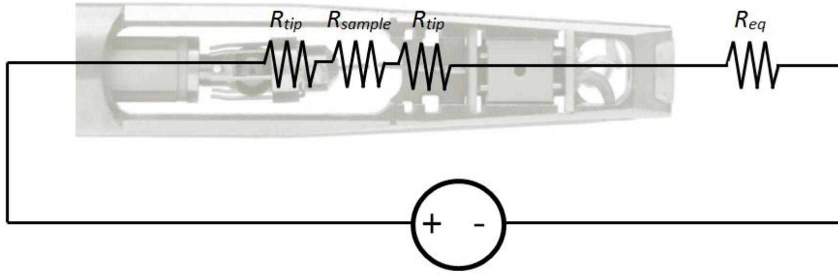

Figure 2.18 Schematic of the resistance system of the TEM-STM holder.

2.5 Analyzing I-V curves

In addition to the calibration of the measuring instrument, in the case of semiconducting nano-objects, I-V curves have to be analyzed. In general, two-terminal measurements can be linear, nonlinear but symmetric or nonlinear and asymmetric depending on factors such as the Fermi level and doping level of the semiconductor, the work function of the metal tip, or the contact condition between the metal tip and the semiconductor[6].

As an example, in the case of measuring the I-V curves of semiconducting nanostructures, the system can be described, at first approximation, by two Schottky barriers embedding the nanostructure. The two metal/semiconductor (M-S) junctions are the Pt-tip/sample and sample/Pt-wire junctions. The schematic diagram of the M-S-M structure and its equivalent circuit are shown in Figure 2.19. The voltages at barrier 1, the nanostructure and barrier 2 are denoted as V_1, V_{sample} and V_2 respectively.

According to the double Schottky diode model, the Schottky contact will be active at either the first or the second junction, depending on the sign of the applied voltage. When not active, one of the two

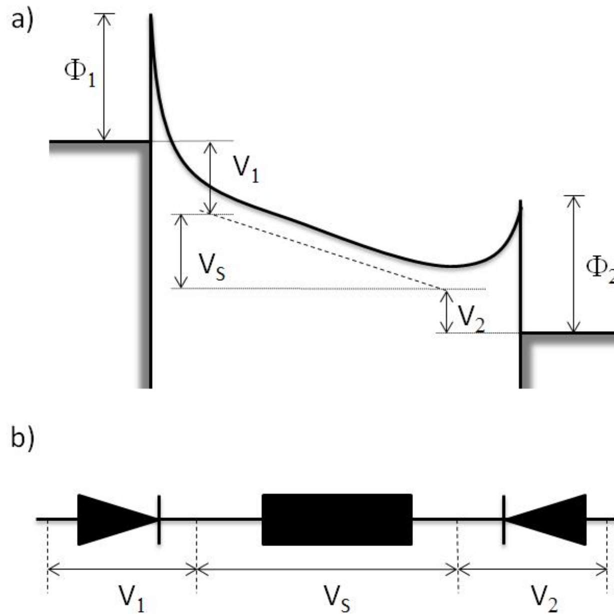

Figure 2.19 (a) Energy band diagram of the M–S–M structure and (b) its equivalent circuit.

Schottky diodes will have a resistive behavior, in series with the active diode and the nanostructure itself.

The M-S-M structure is usually modeled using thermionic emission theory (TED)[7]. If the semiconductor is heavily doped, both contacts may be reduced to ohmic contacts resulting in a linear I-V characteristic. On the other hand, if one contact is ohmic while the other one remains a Schottky contact, the TED predicts a rectifying I-V characteristic. However, the most frequently observed I-V characteristic from semiconducting nanostructures is neither linear nor rectifying, being instead an almost symmetric I-V characteristic as in Figure 2.20.

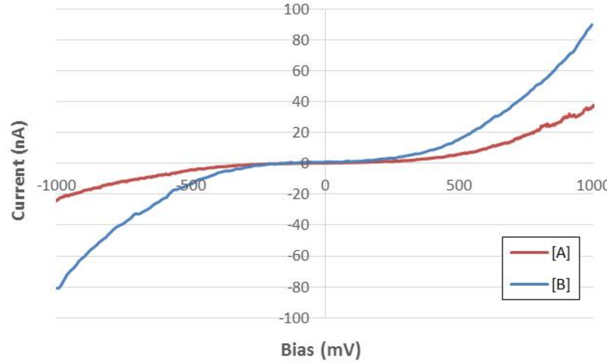

Figure 2.20 I-V characteristic of GaInP structures as an example of an I-V characteristic of semiconducting nanostructures.

From this M-S-M model, one can estimate the intrinsic parameters of the sample. According to the TED model, the current density flowing in the reverse bias Schottky junction is given by

$$J_i = A^{**}T^2 exp\left(\frac{q\Phi_i}{kT}\right) exp\left(\frac{qV_i}{n_i kT}\right) \tag{2.2}$$

Where A^{**} is the effective Richardson constant for Schottky diodes, T is the temperature, Φ_i is the height of the Schottky barrier at the contacts, k is the Boltzmann constant, q is the magnitude of the electron charge and V_i is the effective voltage.

Several authors present this model to analyze I-V characteristics of semiconductor nanomaterials [8-10]. In particular, according to the method presented by Zhang et al.[11], observing figures 2.19 and 2.20 we can consider three regimes. First, at very low bias regime, the current passing through the system is very small and the total voltage is distributed mainly on the two Schottky Barriers (i.e. V_1 and $V_2 \gg V_{sample}$). In the intermediate bias regime, the reverse-biased Schottky barrier dominates and the voltage on the nanostructure

becomes non-negligible. Finally, at larger biases, the voltage V_{sample} increases almost linearly with the bias and becomes the dominating term. So, in this region, the I-V curve can be differentiated to obtain the resistance of the sample,

$$R = \frac{dV_{sample}}{dI} \approx \frac{dV}{dI} \tag{2.3}$$

Thus, analyzing the I-V curves from the M-S-M structure with the TED model, calculations of intrinsic parameters of specific samples can be carried out. This has been extensively applied in the present thesis.

2.6 Conclusions

In this chapter, the TEM-STM holder has been presented, showing the most important parts of the system and the possible applications for the measurement of the electrical properties of nanostructures.

Moreover, the sample preparation for *in-situ* experiments has been described, depending on the type of sample. First, the preparation of nanostructured samples that are electroctransparent *per se* is described. Second, the preparation of devices or bulk samples in a specific location is addressed, presenting the Focused Ion Beam (FIB) sample preparation method for a conventional TEM lamella and the additional steps that are needed during the lamella preparation for the *in-situ* experiments. Furthermore, a new approach for the preparation of the lamella directly on a STM tip is described.

The design and fabrication processes of a handmade gridcase for using a TEM grid as a sample support in the TEM-STM system

have been presented. This improvement offers a greater versatility, enhancing the repeatability and reducing the measurement errors of the *in-situ* experiments

Finally, the calibration of the system has been addressed and the I-V curves of semiconducting nanostructures have been analyzed. The calibration results demonstrate that the effect of the movable tip contact is negligible and that the TEM-STM system offers low errors and good repeatability in the measure of resistances above 0.5 $k\Omega$.

2.7 References

[1] K. Svensson, Y. Jompol, H. Olin, and E. Olsson, “Compact design of a transmission electron microscope-scanning tunneling microscope holder with three-dimensional coarse motion,” Rev. Sci. Instrum., vol. 74, no. 11, pp. 4945–4947, 2003.

[2] L. de Knoop, “Development of quantitative in - situ transmission electron microscopy for nanoindentation and cold - field emission,” Universite de Toulouse, 2014.

[3] R. . Langford and C. Clinton, “In situ lift-out using a FIB-SEM system,” Micron, vol. 35, no. 7, pp. 607–611, 2004.

[4] L. A. Giannuzzi and F. A. Stevie, “A review of focused ion beam milling techniques for TEM specimen preparation,” Micron, vol. 30, pp. 197–204, 1999.

[5] H. M. Nilsson, L. de Knoop, J. Cumings, and E. Olsson, “Localized resistance measurements of wrinkled reduced graphene oxide using in-situ transmission electron microscopy,” Carbon N. Y., vol. 113, pp. 340–345, 2017.

[6]Q. Chen and L.-M. Peng, “Fabrication and electric measurements of nanostructures inside transmission electron microscope,” Ultramicroscopy, vol. 111, pp. 948–954, 2011.

[7] E. H. Rhoderick, “Metal-semiconductor contacts,” IEE Proc. I Solid State Electron Devices, vol. 129, no. 1, p. 1, 1982.

[8] Y. J. Kim, T. G. Yun, I. Choi, S. Kim, W. I. Park, S. Min Han and J. Jang, “Time-dependent mechanical-electrical coupled behavior in single crystal ZnO nanorods,” Scientific Reports, vol. 5, pp. 9716, 2015.

[9] G. Bussone, H. Schafer-Eberwein, E. Dimakis, A. Biermanns, D. Carbone, A. Tahraoui, L. Geelhaar, P. H. Bolívar, T. U. Schulli and U. Pietsch, “Correlation of Electrical and Structural Properties of Single As-Grown GaAs Nanowires on Si (111) Substrates,” Nano Lett., vol. 15, pp. 981–989, 2015.

[10] S. Lu, J. Qi, Z. Wang, P. Lin, S. Liu and Y. Zhang, “Size effect in a cantilevered ZnO micro/nanowire and its potential as a performance tunable force sensor,” RSC Adv., vol. 3, pp. 19375-19379, 2013

[11] Z. Y. Zhang, C. H. Jin, X. L. Liang, Q. Chen, and L.-M. Peng, “Current-voltage characteristics and parameter retrieval of semiconducting nanowires,” Appl. Phys. Lett., vol. 88, no. 7, p. 73102, 2006.

Chapter 3

Effects of electrical current on Graphene Oxide (GO) sheets

3.1 Graphene Oxide (GO)

Graphene is the name given to a flat monolayer of carbon atoms tightly packed into a two-dimensional (2D) honeycomb lattice, a basic building block for graphitic materials of all other dimensionalities (Figure 3.1). It can be wrapped up into 0D fullerenes, rolled into 1D nanotubes or stacked into 3D graphite.

Geim and Novoselov [1] isolated a graphene layer for the first time in 2004 and were able to measure its electrical characteristics. Since then, graphene has attracted a great deal of interest from scientists due to the exciting properties of the single-layer graphene sheets, such

as a Young's modulus of 1 TPa and intrinsic strength of 130 GPa [2], high thermal conductivity (above $3.000 WmK^{-1}$)[3], demonstrated room temperature quantum Hall effect [4], room temperature electron mobility of $2.5x10^5$ $cm^2V^{-1}s^{-1}$ [5], tuneable optical properties [6] and a tuneable band gap [7]. Geim and Novoselov were awarded the Physics Nobel Prize in 2010.

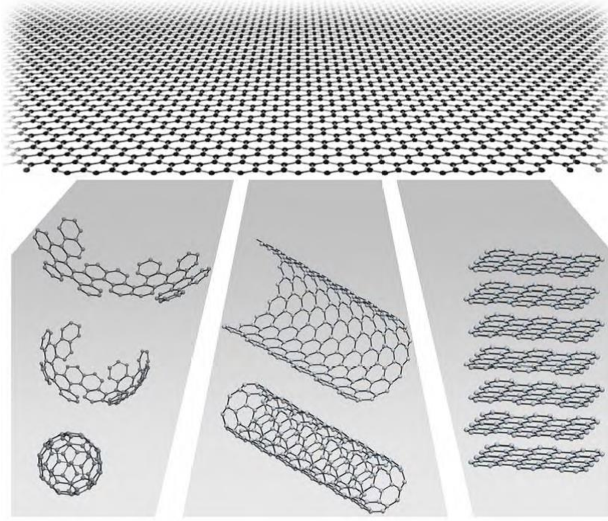

Figure 3.1 Graphene is a 2D building material for carbon materials of all other dimensionalities. It can be wrapped up into 0D buckyballs, rolled into 1D nanotubes or stacked into 3D graphite [8].

Graphene oxide (GO) is an interesting graphene-based material [9] because its physical and chemical properties can be tuned depending on the amount and nature of the functional groups attached to its carbon structure [10–12]. Its use ranges a wide variety of applications such as drug delivery [13], biodevices [14], energy storage systems [15], catalysis [16], memory devices [17], lightweight technology [18] or 3D printing [19].

Usually this material is obtained as a part of the synthesis of graphene layers during the oxidation of graphite [20]. In chemically

obtained graphene oxide the majority of the attached molecules are oxygen-based (O-groups: carboxyl, hydroxyl and epoxy groups)[22,23]. Figure 3.2 shows a schematic of the chemical structure of GO. The covalently bonded O-groups lead to tuneable physical and chemical properties; for example, the conductivity ranges from insulator to semiconductor behaviour as the oxygen content is decreased [23]. For this reason, and due to their two dimensional nature, GO or its reduction products (reduced graphene oxide, rGO) have been proposed as suitable materials to be implemented in advanced electronic nano-devices, and even their combination in all-graphene devices [24–27].

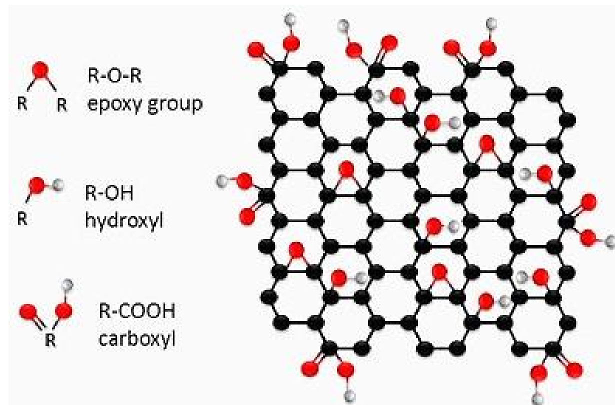

Figure 3.2 Schematics of the chemical structure of grapheme oxide [28].

Extensive literature describes the physical and chemical properties of GO powders [29] and thin film structures [30–32]. However, to better understand the behaviour of GO in electronic nano-devices, the elucidation of the effects of electrical current through a single graphene oxide sheet has received recent attention. In this sense, I. Jung et al.[33] described a controllable thermal reduction of individual GO sheets at low temperatures with simultaneous electrical measurements. More recently, H.M. Nilson et al.[34] have demonstrated the possibility to measure the electrical properties of wrinkled reduced GO flakes

using *in-situ* TEM. Nevertheless, there is a lack of studies correlating the changes of the structural properties of individual GO sheets while an electrical current is flowing through its carbon structure. In this thesis, *in-situ* TEM and Raman spectroscopy have been used to assess the effects of the electrical current applied through a single GO sheet on its structural parameters, enabling a better understanding of the structural modifications of an in-operation GO sheet.

3.2 Electrodeposition of Graphene Oxide sheets

The GO sample preparation and the Raman spectroscopy studies were performed in collaboration with the group of Dr. Albert Cirera from the University of Barcelona. Commercial graphene oxide sheets from GRAnPH Nanotech, Grupo Antolín Ingeniería [35] were dispersed into isopropanol (0.2 mg/mL) and sonicated for 30 minutes to guarantee the appropriated homogeneity of the dispersion. No additives were used. According to oxygen elemental analysis with a Thermo Flash 2000 analyzer, the oxygen content of the GO sheets used in this work was 50 %wt.

Previous to deposition, platinum wires were cleaned with ethanol and sonicated for 30 min to ensure good electrical contact during *in-situ* experiments. GO deposits onto Pt wires, used as a sample support for the *in-situ* TEM, were carried out in a Yflow Electrospinner 3.2.D-400 working as electrospray at room conditions (T=22 °C; 30% relative humidity). This equipment has two high voltage sources, one for the emitter (metallic needle) and another one for the collector. During the deposition process, the working difference potential was fixed at 6.5 kV, the flow rate was kept constant at 0.5 mL/h and the working distance

(between the electrospray nozzle and the Pt wire) at 20 cm. Deposition time was fixed to 1 min in order to avoid GO sheets agglomerations. Figure 3.3 (a) shows a picture of the electrospinner system used and figure 3.3 (b) shows the schematic of the TEM-STM holder with GO sheets attached to a Pt wire as a sample support.

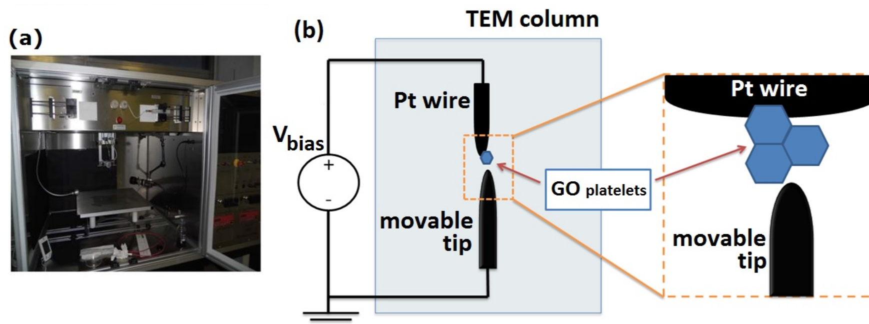

Figure 3.3 (a) Picture of the electrospinner system used for the graphene oxide deposition onto the platinum tip. (b) A scheme of a TEM-STM measuring system for the GO studies.

3.3 Electrical characterization

Four different suitable samples with single GO sheets attached to the platinum wire (referred to as sample I, II, III and IV) were located and electrically contacted. Figure 3.4 shows TEM images of the contacted GO sheets.

The electrical resistance of GO, related with the presence of functional groups bonded to its structure [36], is considered one of its most important characteristics [37]. For this reason, the resistance of the single sheets was measured before and after the application of current, in order to understand the effects of the electric current through individual GO flakes on the electrical conductivity. First of all, a ramp from -100 mV to 100 mV, with 400 sampling points and an

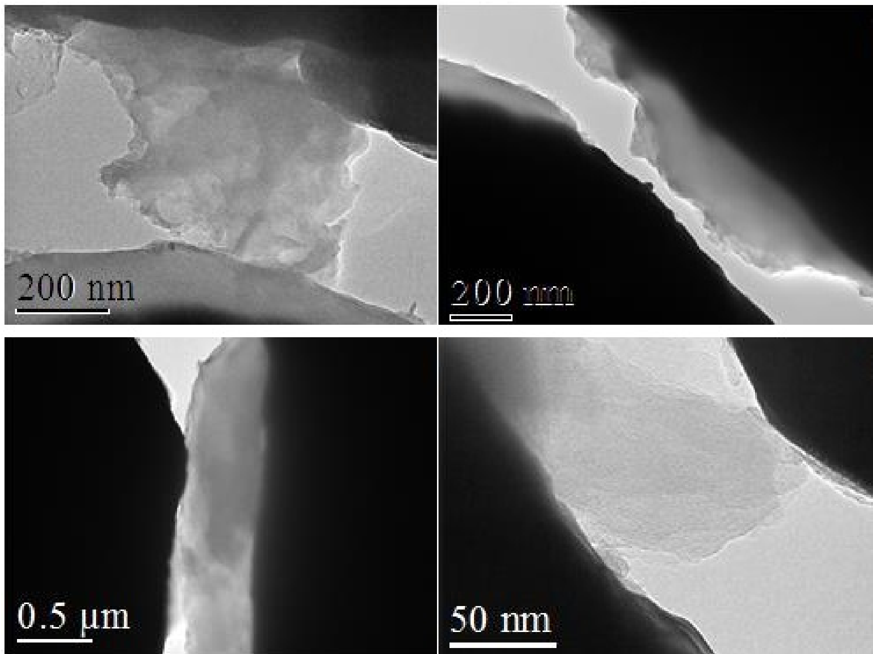

Figure 3.4 TEM images of the contacted GO sheets.

acquisition time of 100 ms for the entire ramp, was used to measure the initial electrical resistance (R_0) of each GO sheet. The R_0 value measured from the I-V curves ranged from 850 kΩ to 2 MΩ (see Table 3.1).

The effects of the electrical current over each single GO sheet were assessed by applying a constant voltage of 100 mV between the Pt wire and the STM movable tip during 100 seconds. The intensity was recorded as a function of time. In order to compare the current measured in all samples, the intensity was normalized to the area (current density, J). The current density was calculated using the geometric parameters of the GO sheets obtained from the TEM images (inset images of Figure 3.5) and by considering the thickness of graphene sheets to be 1 nm [38]. Figure 3.5 shows the current density (J) vs time for each sample (notice the scale change). An increase of the

Sample	R_0 ($k\Omega$)	R_f ($k\Omega$)	$\frac{(R_f - R_0)}{R_0}$	A (nm^2)	I*max* (nA)	J*max* ($A \cdot cm^{-2}$)	Q (nJ)
I	2180	1140	0.47	260	95	0.36	85
II	857	435	0.49	500	243	0.49	2.18
III	996	440	0.55	400	258	0.64	1.85
IV	1114	226	0.80	400	576	1.44	4.78

Table 3.1 Important parameters (initial resistance (R_0), final resistance (R_f), change of the electrical resistance (R_f-R_0)/R_0, surface of the GO sheet (A), maximum current applied to the GO sheet (I_{max}), maximum current density applied to the GO sheet (J_{max}) and Joule heating(Q)) obtained in the *in-situ* TEM experiments for each individual sample.

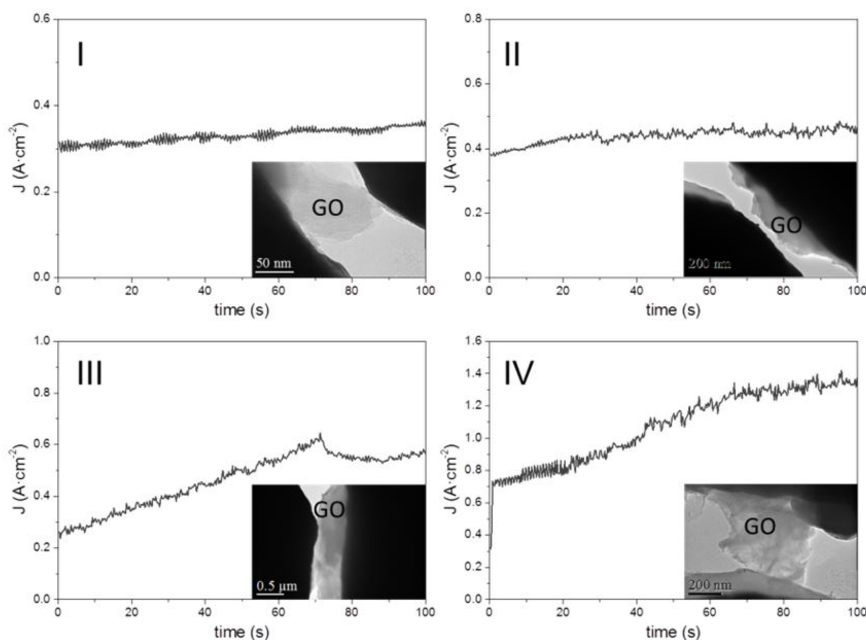

Figure 3.5 Current density vs time curves during the process for the four analyzed GO samples. The inset shows a TEM image of each sample during the experiment, with the platinum tip contacting the GO sheet attached to the platinum wire.

current density is observed in all cases, indicating a decrease of the sheet resistance.

The final electrical resistance (R_f) was determined again from I-V measurements, following the same procedure as described above for

the initial calculation of R_0. The R_f values decreased for all samples reaching values from 220 kΩ to 1 MΩ.

3.4 Joule heating

Due to the nature of the experiment, the decrease of the electrical resistance can be attributed to the Joule heating effect [39], where the Joule heat (Q) can be calculated as:

$$Q = \frac{1}{A}\int_0^t V \cdot J dt = \frac{V}{A}\int_0^t J dt \qquad (3.1)$$

where V=100 mV, A is the surface for each GO sheet, and $\int_0^t J dt$ is the area determined by the J-t curves from Figure 3.5.

Figure 3.6 shows the electrical resistance variation of the samples (defined as (R_f-R_0)/R_0) vs Joule heat (Q). Thus, we observe that, as Joule heat increases, the change of the electrical resistance increases too. Then, because of the Joule heating, a reduction process is taking place, changing the resistance value of the GO sheets due to the removal of the O-groups attached to its carbon structure.

No noticeable changes of the geometry of the GO sheet or the tip-sample contact were observed in TEM images during the experiment in any case. Although morphologically visible changes were not observed, we proceeded to assess by Raman spectroscopy the changes suffered by an in-operation GO sheet in terms of its structural parameters. We expect the electrical current applied on a single GO sheet, using *in-situ* TEM, to give rise to changes in the bonding properties of the GO sheet.

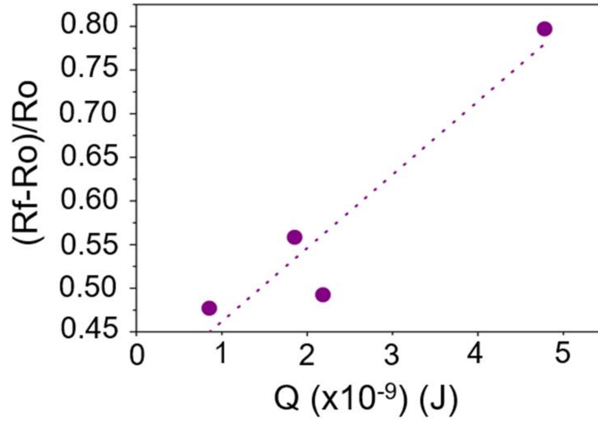

Figure 3.6 Change on the electrical resistance against the Joule heat for the four GO sheets contacted.

3.5 Raman studies

Generally, the spectrum of GO exhibits some common characteristics to graphene, like the G (~1585 cm^{-1}) and the 2D (~2700 cm^{-1}) bands, associated with the first- and second-order allowed Raman mode E_{2g}, respectively [40]. However, GO exhibits a wider G band and the 2D band spreads to a bump located between 2500 and 3200 cm^{-1}; both effects are attributed to a high defect concentration related to oxidation [41]. These two Raman features are also accompanied by a new and intense D peak at ~1350 cm^{-1}. The D band corresponds to the A_{1g} breathing mode and it is related to modifications in the basal plane structure of graphene [42]. Some other less intense peaks appear in graphene oxide Raman spectrum. The D' band, centered at 1620 cm^{-1}, is attributed to the disorder-induced phonon mode due to crystal defects [43]. More recent works have identified two new peaks, D* (between 1150 and 1200 cm^{-1}) and D" (broad peak between 1150 and 1200 cm^{-1}), both fundamental to better fit the 1000-1800 cm^{-1} spectral region [23,44]. These two extra bands have

been related to molecules attached to carbon structure and amorphous parts of chemically obtained GO samples. While D* was related with disordered graphitic lattice provided by sp^2-sp^3 bonds at the edges of the networks [45], S. Vollebregt et al. related D" with interstitial defects associated with amorphous sp^2-bonded forms that may include functionalized small molecules[44]. Recent studies have elucidated the importance of analyzing these interbands D* and D" for the assessment of the reduction degree [22].

The Raman studies in the present thesis have been carried out in close collaboration with the Dr. Cirera group, especially with Dr. Varea. The first order Raman spectra for a pristine GO sheet and the four current-exposed GO samples are shown in Figure 3.7(a). All the spectra were calibrated using the Si band at 520 cm^{-1}. Raman spectra were fitted using 5-bands (Figure 3.7(b)): D and G bands centred at 1350 cm^{-1} and 1588 cm^{-1} respectively, D' band (∼1610 cm^{-1}), D* (∼1150 - 1200 cm^{-1}) and D" (∼1450 - 1550 cm^{-1}).

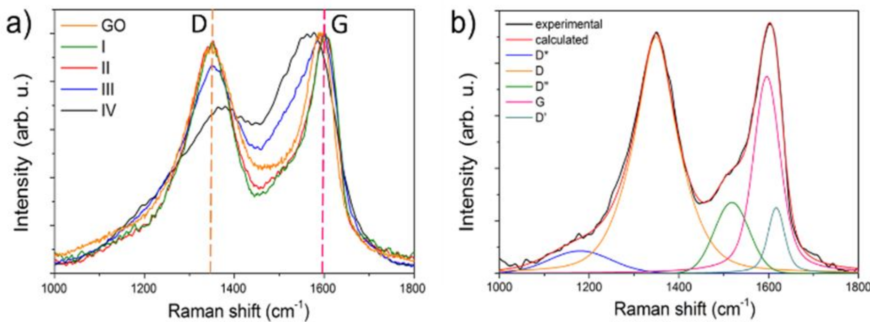

Figure 3.7 (a) First order Raman spectra for GO and treated-GOs under different powers; notorious changes can be observed. (b) An example of 5-fitting method where the calculated data better fits the experimental data.

Considering the previous explanation, in our samples three kinds of spectra can be clearly differenciated: i) The GO spectra from the as received samples, which are characterized by D and G bands located at

1350 cm^{-1} and 1588 cm^{-1} respectively, and a broad shoulder between them, characteristic of chemically obtained GO. ii) The reduced GO spectra (samples I and II), characterized by the G band moved to lower Raman shift values when compared with GO. Also, a decrease of the D-G interband amplitude is observed. iii) Finally, the amorphous carbon spectra (samples III and IV), that show broader D and G bands than GO or rGO spectra and an increase of the interband zone.

To perform a more in-depth study on the structural properties of GO sheets subjected to an electrical current, the changes of the Raman active G, D, D" and D* bands in correlation with the concomitant $(R_f - R_0)/R_0$ changes have been evaluated. Figure 3.8((a) shows the evolution of G and D" band positions for the different electrical resistance changes. The G position values move to higher Raman shift values for the lower resistance changes, and then decreases for higher $(R_f - R_0)/R_0$ values. For D" position, there is an initial stage where D" moves towards lower Raman shift values, and then it increases for higher resistance changes. Other interesting features, the D* and D areas normalized to G band, have been plotted as a function of the electrical resistance variation in Figure 3.8(b); they both show a two-step process: i) an initial step where the D* and D areas are smaller than those for GO, and ii) a second step where the areas recover and overcome these initial values.

Ferrari et al. described a model for the Raman spectra evolution of graphite to amorphous carbon [46]. They suggested that, taking into account the position of G band, there is a first stage where the G band moves towards higher Raman shift values, from graphite to nanocrystalline (nc) graphite, and a second stage that corresponds to the transformation from nc-graphite to amorphous carbon (a-C), where the G band moves the opposite way, i.e. towards lower Raman shift values. D* and D" bands are also good reduction estimators

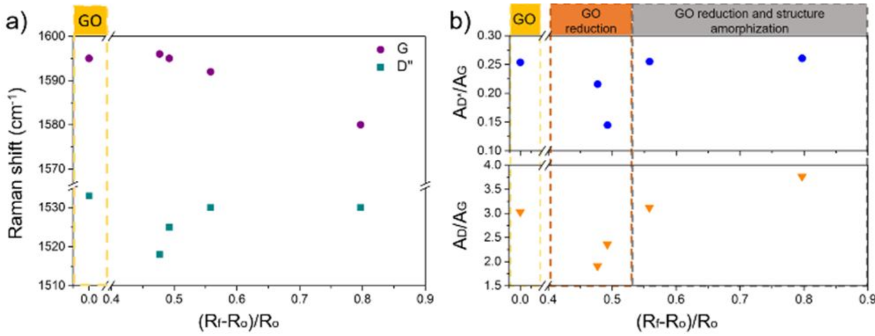

Figure 3.8 (a) Evolution of the position of the D" and G bands as a function of the variation of resistance. (b) Evolution of D* and D band areas normalized to G band as a function of the variation of resistance.

for thermally reduced GO [22]. Changes in D* were attributed to disordered graphitic lattice provided by the existence of sp^3 bonds, while D" changes were ascribed to amorphous phases that may also include organic molecules. Thus, the analysis of G and D" band position indicates that the reduction process is two-fold (Figure 3.8(a)) in good agreement with Ferrari et al.[37]: i) for low resistance changes (i.e. low Joule heat), D" moves towards lower Raman shift values indicating a decrease of the amorphous GO content due to the removal of oxygen functional groups. On the other hand, ii) for higher resistance changes, this band moves to higher Raman shift values indicating an increase of the amorphous phase. This suggests that heating does not only eliminate a fraction of functional groups attached to carbon structure, but also allows the relaxation of the strained lattice around them leading to the formation of holes [47]. The D* area decrease indicates a lower sp^3 bonds content in a first reduction step. This fact is ascribed to carboxyl functional groups removal. For higher applied current the conductor achieves higher temperatures and the removal of hydroxyl groups starts. The removal of hydroxyl groups needs an extra source of carbon atoms, and, if they are taken from the graphitic structure, the sp^3 is promoted, and, as a consequence,

D* band area increases, as can be observed in Figure 3.8(b). The analysis of D band, which is the main indicator of the disorder in carbon structures, confirms that there is an initial reduction stage, where D area decreases, and the formation of ordered sp^2/sp^3 domains is induced due to O-groups removal; however, a second stage starts: D area increases, suggesting the formation of higher sp^3 domains prompted by holes formation (i.e. higher disordered carbon structure). Figure 3.9 shows a schematic representation of this two-step process promoted by the effect of the electrical current through a single GO sheet.

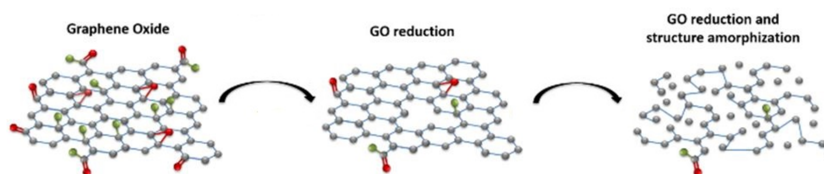

Figure 3.9 Schematic representation of the effects of the electrical current through a single GO sheet.

3.6 High voltage effects

In order to attain a deep understanding of the effects of the electrical current through a single GO sheet, a bias voltage of 5 V was applied through a GO platelet during more than 5 minutes. Figure 3.10 shows a series of TEM images captured during the experiment. As can be seen in the figure, at first the tip is approached to the GO sheet, and then the bias is applied. The TEM images show how apparently there is no change in the sheet structure, until the image taken at second 310 when the GO structure changes. The last image shows a more transparent sheet, which can be related to the reduction of the GO.

As in the previous studies, we proceeded to assess by Raman spectroscopy the changes suffered by the GO sheet in terms of its

structural parameters. We expected the GO sheet to be reduced because of the applied electrical current, but also the hydroxyl groups should be removed inducing the formation of a higher disorder carbon structure. Figure 3.11 shows the first order Raman spectra for a GO sheet as received (orange), a random flake found in the tip which was not exposed to the Joule heating (blue) and finally for a GO sheet exposed to the electrical current (black).

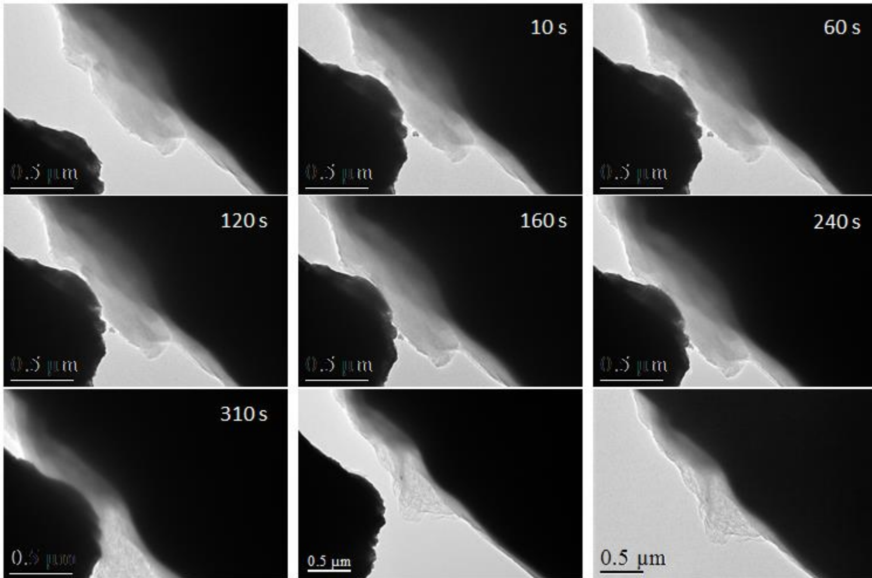

Figure 3.10 Series of TEM images captured during the thermal reduction process under 5 V of constant bias stress as a function of time.

Thus, as expected, the Raman spectrum shows broader D and G bands and an increase of the interband zone related with a reduction of the GO but also with an amorphization of the sample structure.

Moreover, if we compare the TEM images with the current evolution versus time (figure 3.12), we can observe three clear regions. A first region, up to the first two minutes, where the current grows slowly, that can be related to an initial reduction phase due to the removal of oxygen functional groups induced by the Joule heating effect. A

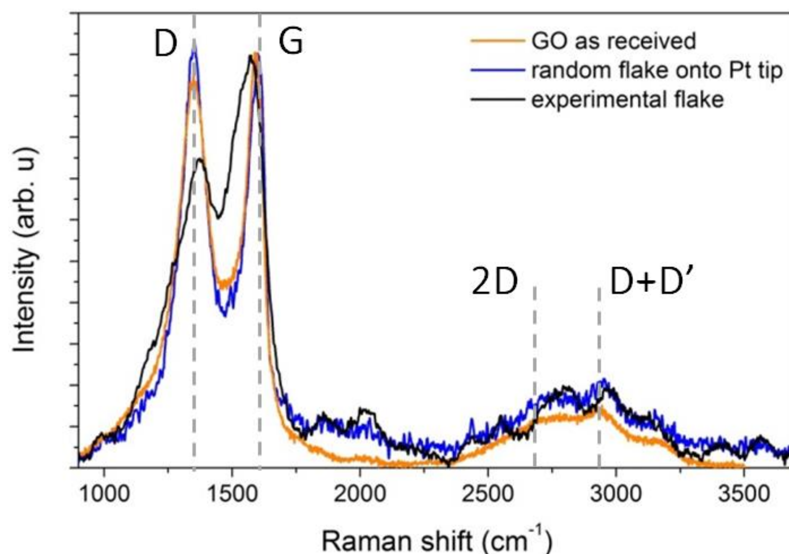

Figure 3.11 First order Raman spectra for a GO sheet as received (orange), a random flake found in the tip which was not exposed to the Joule heating (blue) and a GO sheet exposed to the electrical current (black).

second region, after the first two minutes, where some current peaks are observed. These current peaks could correspond to cracks on the carbon structure due to the removal of hydroxyl groups. Finally, a third region, around the fifth minute, where a transformation of the carbon structure to an amorphous carbon sheet is observed, changing its electrical resistance and allowing an increase of the current.

3.7 Conclusions

Summing up, *in-situ* TEM and Raman have been used to study the effects of the electrical current flow through a single GO sheet. The electrical current passing through an individual GO sheet causes an initial reduced state with the removal of oxygen functional groups due to the Joule heating effect. A lower content of sp^3 bonds is observed

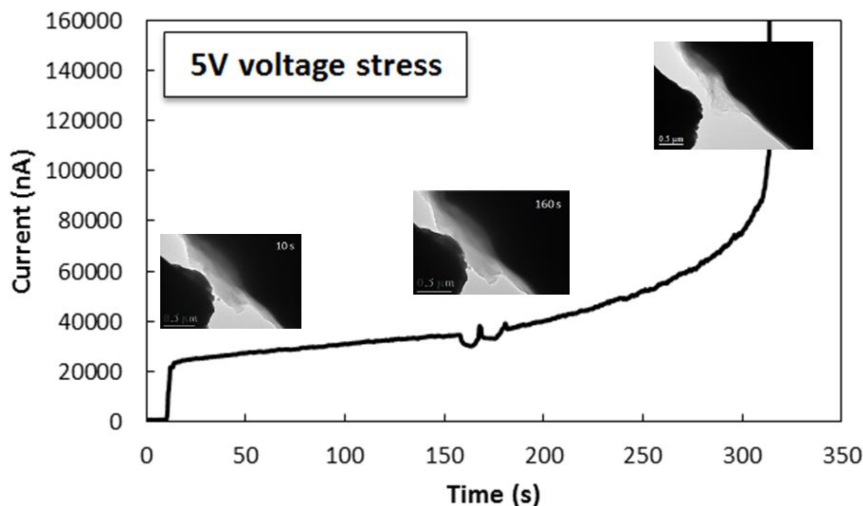

Figure 3.12 I-t curve during the thermal reduction process under a 5 V constant bias stress.

due to the carboxyl functional groups removal. As the electrical current increases through the GO sheet, the removal of hydroxyl groups starts inducing the formation of a highly disordered carbon structure.

Therefore, Joule heating effect can be used for the reduction of GO. However, the applied power has to be limited; otherwise, an amorphization of the graphene-based structure takes place. A balance between reduction and structural disorder needs to be obtained. The results presented in this chapter illustrate the importance of properly analysing the effects of current flow through single sheets of carbonaceous materials.

In future works, it would be interesting to focus on the relationship between the current peaks observed during the Joule heating and the removal of specific O-groups of the GO sheet.

The work presented in this chapter has been published in Nanotechnolgy in 2018 [48].

3.8 References

[1] K. S. Novoselov, A. K. Geim, S. V Morozov, D. Jiang, Y. Zhang, S. V Dubonos, I. V Grigorieva, and A. A. Firsov, "Electric field effect in atomically thin carbon films.," Science, vol. 306, no. 5696, pp. 666–9, 2004.

[2] C. Lee, X. Wei, J. W. Kysar, and J. Hone, "Strength of monolayer graphene measurement of the elastic properties and intrinsic measurement of the elastic properties and intrinsic strength of monolayer graphene," V. Randle, Scr. Mater. S. R. Ortner, Acta Met. Mater. Acta Mater, vol. 385, no. 54, pp. 1011–635, 2008.

[3] A. A. Balandin, "Thermal properties of graphene and nanostructured carbon materials," Nature Materials, vol. 10, no. 8. Nature Publishing Group, pp. 569–581, 2011.

[4] K. S. Novoselov, Z. Jiang, Y. Zhang, S. V. Morozov, H. L. Stormer, U. Zeitler, J. C. Maan, G. S. Boebinger, P. Kim, and A. K. Geim, "Room-temperature quantum hall effect in graphene," Science, vol. 315, no. 5817, pp. 1379, 2007.

[5] K. I. Bolotin, K. J. Sikes, Z. Jiang, M. Klima, G. Fudenberg, J. Hone, P. Kim, and H. L. Stormer, "Ultrahigh electron mobility in suspended graphene," Solid State Communications, vol. 146, no. 9-10, pp. 351-355, 2008.

[6] R. R. Nair, P. Blake, A. N. Grigorenko, K. S. Novoselov, T. J. Booth, T. Stauber, N. M. R. Peres, and A. K. Geim, "Fine Structure Constant Defines Visual Transparency of Graphene," Science (80-.)., vol. 320, no. 5881, pp. 1308–1308, 2008.

[7] Y. Zhang, T.-T. Tang, C. Girit, Z. Hao, M. C. Martin, A. Zettl, M. F. Crommie, Y. R. Shen, and F. Wang, "Direct observation of a widely tunable bandgap in bilayer graphene," Nature, vol. 459, no. 7248, pp. 820–823, 2009.

[8] A. K. Geim and K. S. Novoselov, "The rise of graphene," 2007.

[9] A. C. Ferrari, F. Bonaccorso, V. Falko, K. S. Novoselov, S. Roche, P. Bøggild, S. Borini, F. H. L. Koppens, V. Palermo, N. Pugno, J. A. Garrido, R. Sordan, A. Bianco, L. Ballerini, M. Prato, E. Lidorikis, J. Kivioja, C. Marinelli, T. Ryhänen, A. Morpurgo, J. N. Coleman, V. Nicolosi, L. Colombo,

A. Fert, M. Garcia-Hernandez, A. Bachtold, G. F. Schneider, F. Guinea, C. Dekker, M. Barbone, Z. Sun, C. Galiotis, A. N. Grigorenko, G. Konstantatos, A. Kis, M. Katsnelson, L. Vandersypen, A. Loiseau, V. Morandi, D. Neumaier, E. Treossi, V. Pellegrini, M. Polini, A. Tredicucci, G. M. Williams, B. Hee Hong, J.-H. Ahn, J. Min Kim, H. Zirath, B. J. van Wees, H. van der Zant, L. Occhipinti, A. Di Matteo, I. A. Kinloch, T. Seyller, E. Quesnel, X. Feng, K. Teo, N. Rupesinghe, P. Hakonen, S. R. T. Neil, Q. Tannock, T. Löfwander, and J. Kinaret, "Science and technology roadmap for graphene, related two-dimensional crystals, and hybrid systems," Nanoscale, vol. 7, no. 11, pp. 4598–4810, 2015.

[10] D. R. Dreyer, S. Park, C. W. Bielawski, R. S. Ruoff, J. M. Tour, K. Müllen, A. Ivaska, R. S. Goh, R. H. Friend, A. T. S. Wee, P. K. Ho, D. Chen, and R. S. Ruoff, "The chemistry of graphene oxide," Chem. Soc. Rev., vol. 39, no. 1, pp. 228–240, 2010.

[11] K. P. Loh, Q. Bao, G. Eda, and M. Chhowalla, "Graphene oxide as a chemically tunable platform for optical applications," Nat Chem, vol. 2, no. 12, pp. 1015–1024, 2010.

[12] S. Stankovich, R. D. Piner, S. T. Nguyen, and R. S. Ruoff, "Synthesis and exfoliation of isocyanate-treated graphene oxide nanoplatelets," Carbon N. Y., vol. 44, no. 15, pp. 3342–3347, Dec. 2006.

[13] T. Yin, J. Liu, Z. Zhao, Y. Zhao, L. Dong, M. Yang, J. Zhou, and M. Huo, "Redox sensitive hyaluronic acid-decorated graphene oxide for photothermally controlled tumor-cytoplasm-selective rapid drug delivery," Adv. Funct. Mater., vol. 27, no. 14, p. 1604620, 2017.

[14] N. Luo, J. K. Weber, S. Wang, B. Luan, H. Yue, X. Xi, J. Du, Z. Yang, W. Wei, R. Zhou, and G. Ma, "PEGylated graphene oxide elicits strong immunological responses despite surface passivation," Nat. Commun., vol. 8, p. 14537, 2017.

[15] Z. Sun, J. Zhang, L. Yin, G. Hu, R. Fang, H. M. Cheng, and F. Li, "Conductive porous vanadium nitride/graphene composite as chemical anchor of polysulfides for lithium-sulfur batteries," Nat. Commun., vol. 8, p. 14627, 2017.

[16] S. Wang, R. Cazelles, W.-C. Liao, M. Vazquez-Gonzalez, A. Zoabi, R. Abu-Reziq, and I. Willner, "Mimicking horseradish peroxidase and NADH peroxidase by heterogeneous Cu^2+ -modified graphene oxide nanoparticles," Nano Lett., vol. 17, no. 3, pp. 2043–2048, 2017.

[17] V. K. Nagareddy, M. D. Barnes, F. Zipoli, K. T. Lai, A. M. Alexeev, M. F. Craciun, and C. D. Wright, "Multilevel Ultrafast Flexible Nanoscale nonvolatile hybrid graphene oxide titanium oxide memories," ACS Nano, vol. 11, no. 3, pp. 3010–3021, 2017.

[18] D. Joung, A. Nemilentsau, K. Agarwal, C. Dai, C. Liu, Q. Su, J. Li, T. Low, S. J. Koester, and J. H. Cho, "Self-assembled three-dimensional graphene-based polyhedrons inducing volumetric light confinement," Nano Lett., vol. 17, no. 3, pp. 1987–1994, 2017.

[19] J. Z. Manapat, J. D. Mangadlao, B. D. B. Tiu, G. C. Tritchler, and R. C. Advincula, "High-strength stereolithographic 3D printed nanocomposites: graphene oxide metastability," ACS Appl. Mater. Interfaces, vol. 9, no. 11, pp. 10085–10093, 2017.

[20] D. Li, M. B. Müller, S. Gilje, R. B. Kaner, and G. G. Wallace, "Processable aqueous dispersions of graphene nanosheets," Nat. Nanotechnol., vol. 3, no. 2, pp. 101–105, 2008.

[21] G. Eda, G. Fanchini, and M. Chhowalla, "Large-area ultrathin films of reduced graphene oxide as a transparent and flexible electronic material," Nat. Nanotechnol., vol. 3, no. 5, pp. 270–274, 2008.

[22] S. Claramunt, A. Varea, D. Lopez-Diaz, M. M. Velazquez, A. Cornet, and A. Cirera, "The importance of interbands on the interpretation of the raman spectrum of graphene oxide," J. Phys. Chem. C, vol. 119, no. 18, pp. 10123–10129, 2015.

[23] H. A. Becerril, J. Mao, Z. Liu, R. M. Stoltenberg, Z. Bao, and Y. Chen, "Evaluation of solution-processed reduced graphene oxide films as transparent conductors," ACS Nano, vol. 2, no. 3, pp. 463–470, 2008.

[24] X. Wang, H. Tian, M. A. Mohammad, C. Li, C. Wu, Y. Yang, and T. L. Ren, "A spectrally tunable all-graphene-based flexible field-effect light-emitting device," Nat. Commun., vol. 6, 2015.

[25] W. Kim, C. Li, N. Chekurov, S. Arpiainen, D. Akinwande, H. Lipsanen, and J. Riikonen, “All-graphene three-Terminal-junction field-effect devices as rectifiers and inverters,” ACS Nano, vol. 9, no. 6, pp. 5666–5674, 2015.

[26] C. Ogata, R. Kurogi, K. Hatakeyama, T. Taniguchi, M. Koinuma, Y. Matsumoto, X. Chen, A. Aspuru-Guzik, R. G. Gordon, M. J. Aziz, T. Yamada, H. Kitagawa, and S. Hayami, “All-graphene oxide device with tunable supercapacitor and battery behaviour by the working voltage,” Chem. Commun., vol. 52, no. 20, pp. 3919–3922, 2016.

[27] I. Lahiri, V. P. Verma, and W. Choi, “An all-graphene based transparent and flexible field emission device,” Carbon N. Y., vol. 49, no. 5, pp. 1614–1619, 2011.

[28] N.-F. Chiu, T.-Y. Huang, and H.-C. Lai, “Graphene oxide based surface plasmon resonance biosensors,” in Advances in Graphene Science, InTech, pp. 191–216, 2013.

[29] S. Stankovich, D. A. Dikin, R. D. Piner, K. A. Kohlhaas, A. Kleinhammes, Y. Jia, Y. Wu, S. T. Nguyen, and R. S. Ruoff, “Synthesis of graphene-based nanosheets via chemical reduction of exfoliated graphite oxide,” 2007.

[30] C. Mattevi, G. Eda, S. Agnoli, S. Miller, K. A. Mkhoyan, O. Celik, D. Mastrogiovanni, G. Granozzi, E. Garfunkel, and M. Chhowalla, “Evolution of electrical, chemical, and structural properties of transparent and conducting chemically derived graphene thin films,” Adv. Funct. Mater., vol. 19, no. 16, pp. 2577–2583, 2009.

[31] D. Yang, A. Velamakanni, G. Lay Bozoklu, S. Park, M. Stoller, R. D. Piner, S. Stankovich, I. Jung, D. A. Field, C. A. Ventrice, and R. S. Ruoff, “Chemical analysis of graphene oxide films after heat and chemical treatments by X-ray photoelectron and Micro-Raman spectroscopy,” Carbon N. Y., vol. 47, pp. 145–152, 2008.

[32] O. O. Ekiz, M. Urel, H. Guner, A. K. Mizrak, and A. Dana, “Reversible electrical reduction and oxidation of graphene oxide,” ACS Nano, vol. 5, no. 4, pp. 2475–2482, 2011.

[33] I. Jung, D. A. Dikin, R. D. Piner, and R. S. Ruoff, “Tunable electrical conductivity of individual graphene oxide sheets reduced at ‘low’ temperatures,” Nano Lett., vol. 8, no. 12, pp. 4283–4287, 2008.

[34] H. M. Nilsson, L. de Knoop, J. Cumings, and E. Olsson, “Localized resistance measurements of wrinkled reduced graphene oxide using in-situ transmission electron microscopy,” Carbon N. Y., vol. 113, pp. 340–345, 2017.

[35] B. Lobato, C. Merino, V. Barranco, T. A. Centeno, A. Macías-García, V. Gómez-Serrano, F. Stoeckli, R. Carter, and I. A. Aksay, “Large-scale conversion of helical-ribbon carbon nanofibers to a variety of graphene-related materials,” RSC Adv., vol. 6, no. 62, pp. 57514–57520, 2016.

[36] Y. Zhu, S. Murali, W. Cai, X. Li, J. W. Suk, J. R. Potts, and R. S. Ruoff, “Graphene and graphene oxide: synthesis, properties, and applications,” Adv. Mater., vol. 22, no. 35, pp. 3906–3924, 2010.

[37] C. Gómez-Navarro, R. T. Weitz, A. M. Bittner, M. Scolari, A. Mews, M. Burghard, and K. Kern, “Electronic transport properties of individual chemically reduced graphene oxide sheets,” Nano Lett., vol. 7, no. 11, pp. 3499–3503, 2007.

[38] C. J. Shearer, A. D. Slattery, A. J. Stapleton, J. G. Shapter, and C. T. Gibson, “Accurate thickness measurement of graphene,” Nanotechnology, vol. 27, no. 12, p. 125704, 2016.

[39] Y. Zhu, S. Murali, W. Cai, X. Li, J. W. Suk, J. R. Potts, and R. S. Ruoff, “Graphene and graphene oxide: synthesis, properties, and applications,” Adv. Mater., vol. 22, no. 35, pp. 3906–3924, 2010.

[40] S. Reich and C. Thomsen, “Raman spectroscopy of graphite,” Philosophical Transactions of the Royal Society A, vol. 362, no. 1824, pp. 2271-2288, 2004.

[41] E. H. Martins Ferreira, M. V. O. Moutinho, F. Stavale, M. M. Lucchese, R. B. Capaz, C. A. Achete, and A. Jorio, “Evolution of the Raman spectra from single-, few-, and many-layer graphene with increasing disorder,” Phys. Rev. B, vol. 82, no. 12, p. 125429, 2010.

[42] L. G. Cançado, A. Jorio, E. H. M. Ferreira, F. Stavale, C. A. Achete, R. B. Capaz, M. V. O. Moutinho, A. Lombardo, T. S. Kulmala, and A. C. Ferrari, "Quantifying defects in graphene via Raman spectroscopy at different excitation energies," Nano Lett., vol. 11, no. 8, pp. 3190–3196, 2011.

[43] X. Zhao and Y. Ando, "Raman spectra and X-Ray diffraction patterns of carbon nanotubes prepared by hydrogen arc discharge," Jpn. J. Appl. Phys., vol. 37, no. Part 1, No. 9A, pp. 4846–4849, 1998.

[44] S. Vollebregt, R. Ishihara, F. D. Tichelaar, Y. Hou, and C. I. M. Beenakker, "Influence of the growth temperature on the first and second-order Raman band ratios and widths of carbon nanotubes and fibers," Carbon N. Y., vol. 50, no. 10, pp. 3542–3554, 2012.

[45] A. Sadezky, H. Muckenhuber, H. Grothe, R. Niessner, and U. Pöschl, "Raman microspectroscopy of soot and related carbonaceous materials: Spectral analysis and structural information," Carbon N. Y., vol. 43, no. 8, pp. 1731–1742, 2005.

[46] A. Ferrari and J. Robertson, "Interpretation of Raman spectra of disordered and amorphous carbon," Phys. Rev. B - Condens. Matter Mater. Phys., vol. 61, no. 20, pp. 14095–14107, 2000.

[47] X. Díez-Betriu, S. Álvarez-García, C. Botas, P. Álvarez, J. Sánchez-Marcos, C. Prieto, R. Menéndez, and A. de Andrés, "Raman spectroscopy for the study of reduction mechanisms and optimization of conductivity in graphene oxide thin films," J. Mater. Chem. C, vol. 1, no. 41, p. 6905, 2013.

[48] G. Martín, A. Varea, A. Cirera, S. Estradé, F. Peiró, A. Cornet, "Effects of electric current on individual graphene oxide sheets combining in-situ transmission electron microscopy and raman spectroscopy," Nanotechnology, Just Accepted, 2018.

Chapter 4

Piezo- and ferroelectricity of lead-free thin films

4.1 Piezoelectricity and ferroelectricity

Piezoelectricity was discovered by Jacques Curie and Pierre Curie [1] in 1880. By analogy with temperature-induced charges in pyroelectric crystals, they observed the generation of electricity under mechanical pressure of certain crystals such as quartz, zinc blendes, tourmaline and Rochelle salt. The converse piezoelectric effect (i.e. deformation or strain under applied electric field) was mathematically deduced from fundamental thermodynamic principles by Lippmann [2] and experimentally confirmed by the Curie brothers [3] in 1881.

From the very beginning it was understood that the crystallographic symmetry of materials played a decisive role in piezoelectric phenomena.

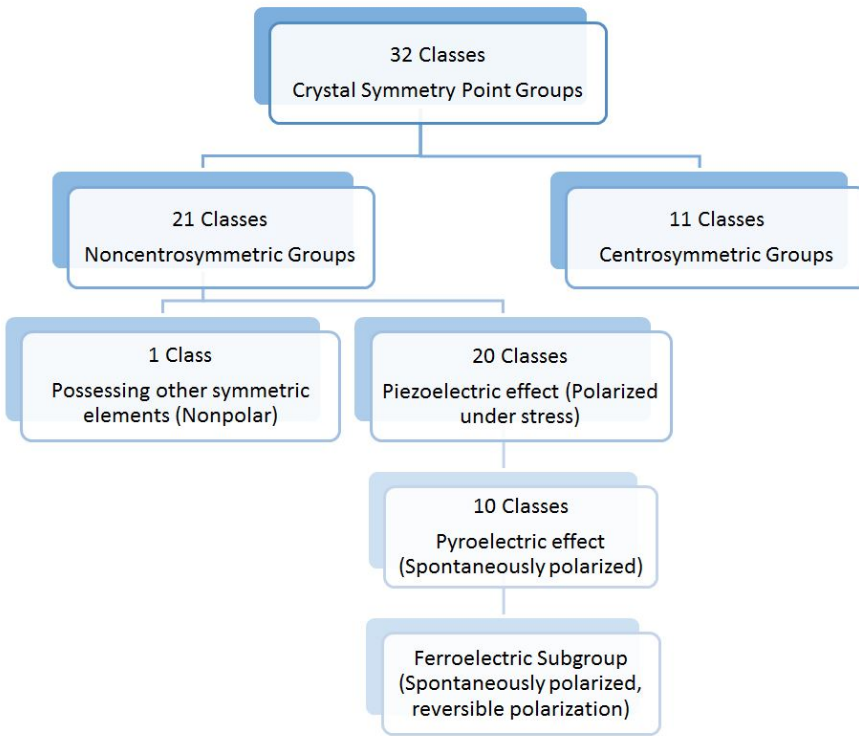

Figure 4.1 Grouping of crystal classes according to their piezoelectric, pyroelectric and ferroelectric properties.

Figure 4.1 summarizes the classification of the crystallographic classes according to their piezoelectric, pyroelectric and ferroelectric properties. From the 32 crystallographic classes, piezoelectricity may exist in the non centro-symmetric crystallographic structures (see figure 4.2), except for the cubic 21th class (432), where the piezoelectric charges along the <111> polar axes cancel each other. Among the 20 piezoelectric crystal classes, there are ten pyroelectric point groups that possess a unique polar axis. Pyroelectric crystals contain a built-in polarization, which manifests itself in temperature-induced changes of the total dipole moment of the unit cell (in the absence of applied fields). If this spontaneous polarization can be reversed

by an external electric field, the crystal is called ferroelectric. This phenomenon was discovered in Rochelle salt crystal by Joseph Valasek [4] in 1920, observing the typical hysteretic behaviour between electric displacement and electric field.

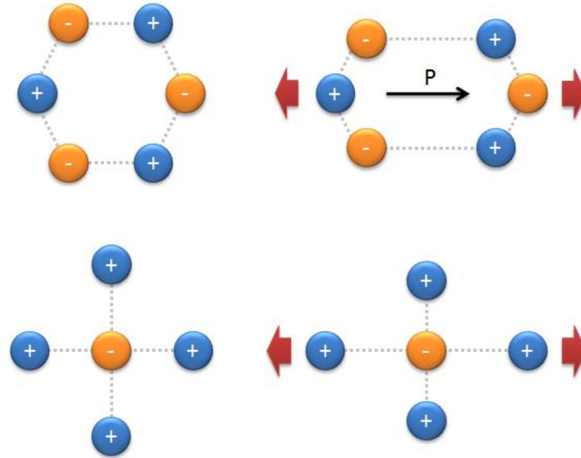

Figure 4.2 Schematic of non centro-symmetric (top) and centro-symmetric (bottom) crystallographic structures under an external mechanical pressure.

Piezoelectric and ferroelectric materials are of high interest in advanced electronics and are of great industrial and economic importance. Their applications are widespread and include sonars, frequency filters, gas ignitors, ultrasonic and medical diagnosis transducers, surveillance devices and FeRAM memories among others [5].

In last years *in-situ* electron microscopy has been used to study piezoelectricity, allowing experiments on piezoelectric nanomaterials. In 2006, the Wang group used a combination of SEM and a multiprobe Ti/Au/W tip, demonstrating that ZnO nanowires can act as piezoelectric-gated diodes [6]. More recently, in 2014, Renyun et al.[7] investigated the same material, piezoelectric-gated ZnO nanowire

diodes, using *in-situ* TEM, demonstrating that the diode is actually gated by the piezoelectric effect. In 2017, Okayasu et al.[8] performed *in-situ* TEM observations of microstructural characteristics of lead zirconate titanate piezoelectric ceramics during heating to 1000 °C. Thus, *in-situ* TEM studies on piezoelectric materials can lead to an understanding of the local effects of piezoelectricity and ferroelectricity on nanostructures allowing the improvement of new electronic devices.

4.2 Advanced ferroelectric materials

To date, lead-based oxides are the most widely exploited and extensively used ferroelectric materials. The perovskite solid solution family of lead-zirconate-titanates $Pb(Zr,Ti)O_3$ (PZT) is by far the most widely used piezoceramics because of their outstanding electromechanical properties that can be tailored to numerous applications through chemical modifications.

PZT are widely used as sensor and actuator devices multilayered capacitors, as hydrophones, etc.[9–11], with an estimated market of tens of billions of dollars worldwide, due to their excellent polarization values, dielectric constant, easy integration to various devices and piezoelectric constant.

However, PZT are composed of about 60 %wt. lead, which rises important concerns. Thus, some countries have legislated to replace these materials by lead-free ceramics since lead is a toxic element that affects the human health and the environment. In this sense, the development of lead-free piezoelectric and ferroelectric materials and its characterization at device level is mandatory.

Lead-free oxides based on A_2O_3-MO_3 (A=Bi^{3+} or Ln^{3+}; M=Mo or W) systems are of significant technological interest owing to

laser applications [12], ionic conduction [13], catalytic [14] and, particularly, ferroelectric [15] properties.For the La_2WO_6 (LWO) compound, bibliography is scarce and its two polymorphic structures (i.e., β-La_2WO_6 and α-La_2WO_6) were solved only recently [16,17].

The low temperature variety, β-LWO, which crystallizes in the space group $P2_12_12_1$ (group n.19) with cell parameters a = 7.5196(1) Å, b = 10.3476(1) Å and c = 12.7944(2) Å; and the high temperature one, α-LWO, crystallizes in the space group $Pm2_1n$ (group n.31) with quenched cell parameters a =16.5531(1) Å, b = 5.52003(3) Å and c = 8.88326(3) Å (see figure 4.3) [17]. In fact, the two polymorphs, α and β, crystallize in a non centro-symmetric space group, and this can lead to potentially interesting ferroelectric properties.

In this chapter, the piezo- and ferroelectric behaviour at local level of α-LWO thin films, grown on (100)-oriented $SrTiO_3$ (STO) substrate by Pulsed Layer Deposition (PLD), will be addressed. No other such studies are found in the literature.

4.3 α-La_2WO_6 films growth

The α-La_2WO_6 thin films growth and the X-Ray structural studies were performed by the group of Dr. Marie-Hélène Chambrier from the University of Artois.

Initially, ground powder was obtained from the La_2O_3 and WO_3 oxides, weighted in stoichiometric proportions and mecanically mixed together in an agate mortar. Before crushing, the lanthanum oxide powder was first dried and decarbonated at 1000 °C, overnight. The prepared compound was then heated at 1350 °C, during one complete night, in an alumina crucible, before cooling it down. This procedure

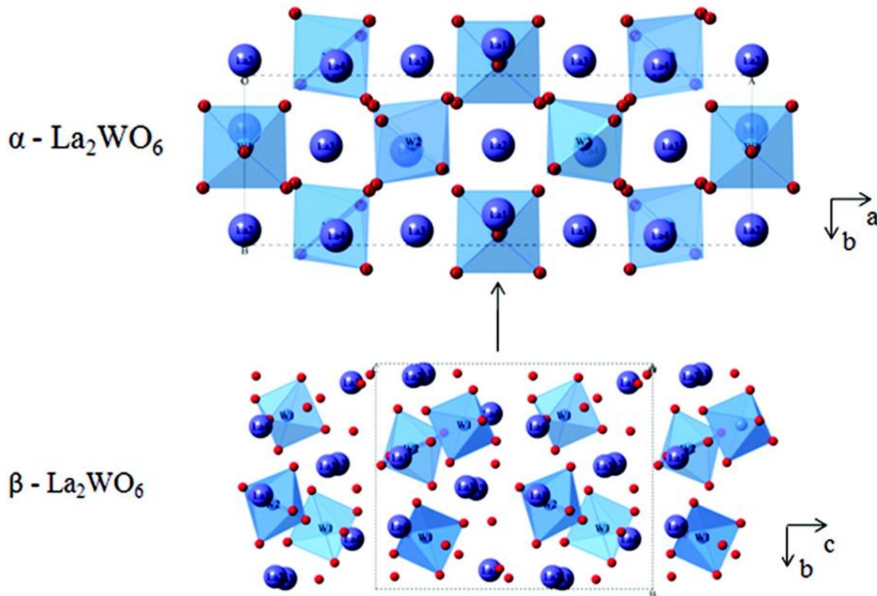

Figure 4.3 Crystal structures of the α and β-LWO phases [17].

was repeated twice to ensure more reliable results. Electron Diffraction (ED) analyses were performed on the powder as shown in figure 4.4. The sharp spots and the absence of any diffuse streaks demonstrate the good crystallization of the sample and rule out the existence of any stacking defects.

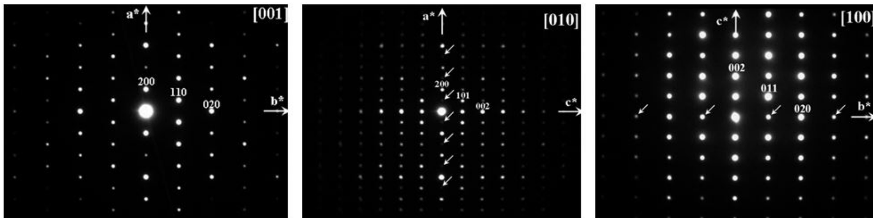

Figure 4.4 Electron diffraction patterns of α-La_2WO_6 phase recorded along the [001], [010], and [100] directions. White arrows point to forbidden reflections appearing from double diffraction.

In order to prepare the target for PLD, the ground powder was compelled into pellets (1 in. diameter) with the help of uniaxial

pressure and finally annealed at 1450 °C for 12h in air before letting it slowly cool down toward room temperature.

LWO thin films were deposited on (100) $SrTiO_3$(STO) single-crystal substrates (Crystal GmbH, Germany). All substrates were first ultrasonically cleaned in ethanol for 5 min, and then dried. The pressure in the pulsed-laser chamber was lowered down to 1×10^{-6} mbar and the substrate temperature for the film growth raised through a 10 °C/min step elevation toward synthesis temperature (three temperatures were tested: 600, 800, and 900 °C) while adjusting the O_2 pressure during deposition to 1×10^{-3} mbar or 1×10^{-1} mbar. Finally, at the end of deposition, the O_2 pressure was increased up to 200 mbar in the chamber and next, the films were slowly cooled to room temperature.

Depositions were carried out by PLD using a Compex Pro 102 KrF excimer laser ($\lambda = 248$ nm). All films were grown using 6000 laser-pulse shots. The fluence was adjusted to 2 J/cm^2 and the deposition rate fixed at 2 Hz. The target-substrate distance was adjusted to d = 4.5 cm.

Because there were no previous studies about pulsed laser deposition of LWO, the first step consisted in optimizing the thin film growth conditions. For such a purpose, both the temperature of the substrate and the O_2 pressure during deposition were optimized in order to increase the thin-film quality. XRD diffractograms were acquired at three different deposition temperatures, ranging from 600 to 900 °C (Figure 4.5). For the lowest temperature considered, i.e., 600 °C, no crystalline peak is observed, implying an amorphous film. Increasing the pressure from 10^{-3} to 10^{-1} mbar has no influence on crystallization (4.5 (a), (d)). At 800 °C, the O_2 pressure plays an important role: whereas the thin film is still amorphous under a

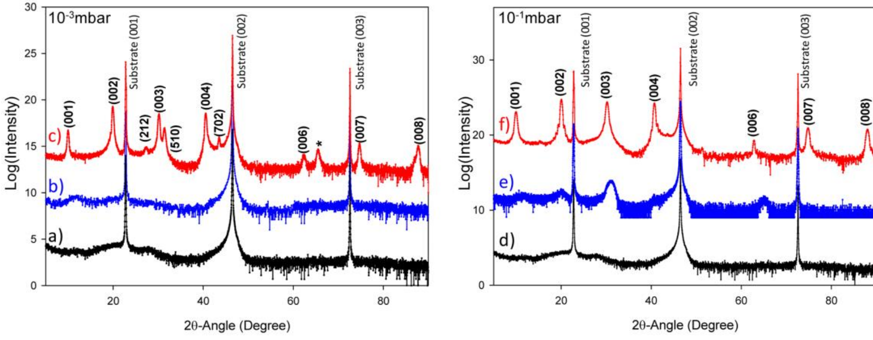

Figure 4.5 X-ray diffractograms showing the effect of temperature T and pressure P in obtaining epitaxial α-La_2WO_6 thin film. (a) T = 600 °C and $P_{O_2} = 1 \times 10^{-3}$ mbar; (b) T = 800 °C and $P_{O_2} = 1 \times 10^{-3}$ mbar; (c) T = 900 °C and $P_{O_2} = 1 \times 10^{-3}$ mbar (the star corresponds to an unidentified peak); (d) T = 600 °C and $P_{O_2} = 1 \times 10^{-1}$ mbar; (e) T = 800 °C and $P_{O_2} = 1 \times 10^{-1}$ mbar; (f) T = 900 °C and $P_{O_2} = 1 \times 10^{-1}$ mbar.

pressure of 1×10^{-3} mbar, some XRD peaks with large full width at half maximum (FWHM) appear under a pressure of 1×10^{-1} mbar (Figure 4.5 (b), (e)). Finally, at 900 °C for the two tested pressures, 1×10^{-3} and 1×10^{-1} mbar, well-defined families of XRD peaks emerge. Such an observation at this rather high temperature is not surprising when taking into account the refractive behavior of these oxides. However, the number of diffraction peaks that are observed on the diffractograms appears rather limited, compared to the ones obtained in the case of bulk materials. As a result, the indexation may only carry some signature conferring the α-La_2WO_6 composition to the obtained thin films.

Considering the film grown at 900 °C under an O_2 pressure of 10^{-1} mbar, a preliminary TEM study was carried out to demonstrate the possibility to grow highly oriented c-axis α-LWO thin films and that the high-temperature α-LWO polymorph may be stabilized at room temperature in thin film by PLD.

4.4 Preliminary TEM characterization

TEM images were, thus, acquired in a cross-section configuration from the sample grown at 900°C under an O_2 pressure of 10^{-1} mbar, prepared by FIB using the lift-out technique.

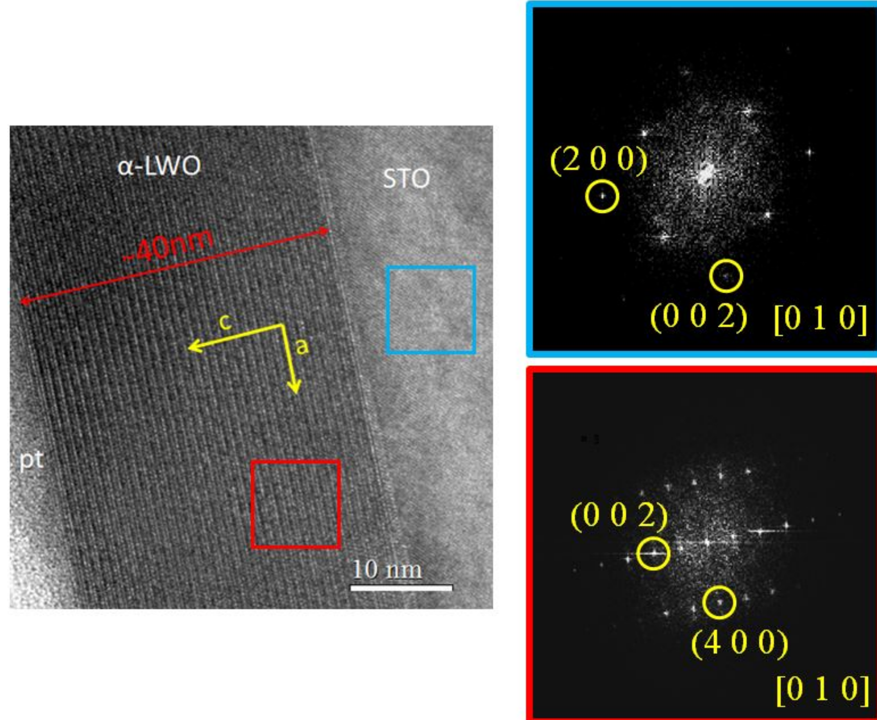

Figure 4.6 (a) HRTEM image of an α-LWO thin film grown on a (001)-oriented STO substrate; (b) and (c) FFT of the highlighted areas in (a).

Figure 4.6 shows an HRTEM image of the LWO/STO system and the corresponding Fast Fourier Transform (FFT) of the LWO thin film and the substrate. The FFT of the layer could be indexed according to α-LWO structure.

Moreover, the α-LWO film thickness was determined to be close to 40nm. As the films were grown using 6000 laser-pulse shots, the

deposition rate can be determined as 0.067 Å ± 0.017 Å par laser-pulse shot.

Furthermore, good thin film crystallinity was evidenced with no amorphous areas at the interface between the film and the substrate.

From the FFT calculations, the (001) orientation of the film growth was confirmed (marked as c axis in Figure 4.6). Moreover, the expected epitaxial relationship, shown in figure 4.7, was also assessed.

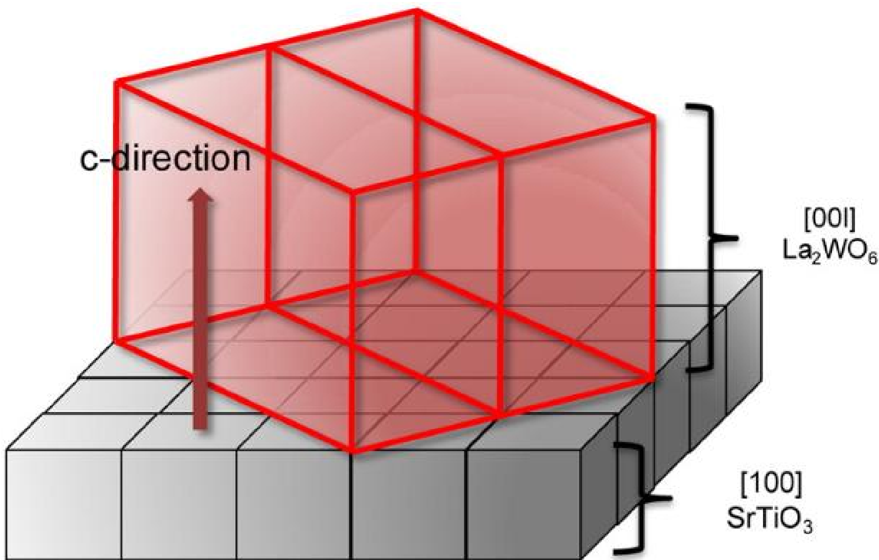

Figure 4.7 Epitaxy relationship scheme of the α-LWO thin film on a STO-(100) substrate.

4.5 *Ex-situ* AFM characterization

An ex-situ AFM characterization of the α-LWO thin films was carreid out by the Chambrier group.

To address the local switching behavior of ferroelectric domains, as well as the piezo-activity, piezo-response loops have been performed

by placing the AFM tip over the free film surface. Off-field phase and amplitude loops are depicted in figure 4.8. In this procedure, each point was measured at zero bias voltage to promote the electromechanical contribution at the expense of the electrostatic effect, which corresponds to the remnant response. Square hysteresis response is clearly obtained from the phase signal (Figure 4.8 (a)). Both opposite polarization states and the hysteretic behavior strongly reveal the local ferroelectricity in the as-deposited α-LWO thin film.

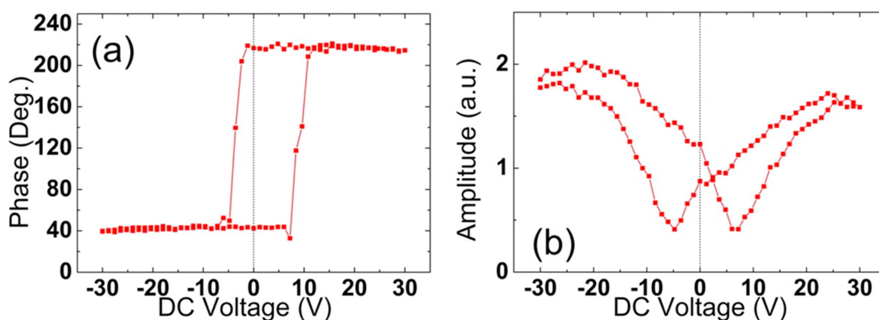

Figure 4.8 Remnant (a) phase and (b) amplitude hysteresis loops, simultaneously measured on the free surface of the α-LWO thin film.

Besides, a well-defined typical butterfly shape due to the inverse piezoelectric effect is observed for the simultaneously recorded amplitude piezo-loop (Figure 4.8 (b)), evidencing the local piezo-activity of the film. In addition, a saturated loop is measured without a linear part, an indication of the strong electromechanical contribution to the detected piezo-signal.

4.6 Piezoelectricity *in-situ* characterization

Although the macroscopic piezoelectric behavior of this material is thus demonstrated, the local piezoelectric response of α-LWO is studied here by using the Nanofactory STM holder.

The TEM-STM system can be used for piezo-controlled movement of the tip for the deformation of nanoscale materials. The tip is moved at a constant velocity and this design allows us to control the movement of the Pt probe to ensure optimum contact with the specimen, but also allows for electromechanical testing of materials. Unfortunately, the mechanical measurements made using this design are only qualitative because the applied force can be only correlated with the displacement of the TEM-STM tip.

The TEM lamella was prepared by FIB using the lift-out technique. Figure 4.9 depicts a schematic of the system used for this experiment. The lamella was attached to an Omniprobe grid with FIB Pt deposition. As can be seen in the figure, a final step during the FIB sample preparation was to mill part of the Pt protection in order to allow the tip to access the α-LWO thin film (see chapter 2 for more details about the TEM lamella preparation for *in-situ* experiments).

The first step of the experiment was to characterize the conductivity through the FIB platinum deposition, contacting with the tip at position "1" of figure 4.9(c). The resistance through the FIB platinum deposition is about 500 Ω, which shows that the system allows for good electrical conduction.

Figure 4.9 (c) shows the movable tip of the holder contacting the α-LWO thin film and figure 4.9 (d) shows with an arrow the direction of the pressure applied with the tip to the sample during the experiments.

A qualitative characterization of the piezoelectric behavior was carried out by measuring the I-V curves while pressure was applied by the STM tip to the sample. These *in-situ* TEM measurements enable us to probe the direct effect of the piezoelectricity, i.e., the generated electrical energy (or current) following the application of

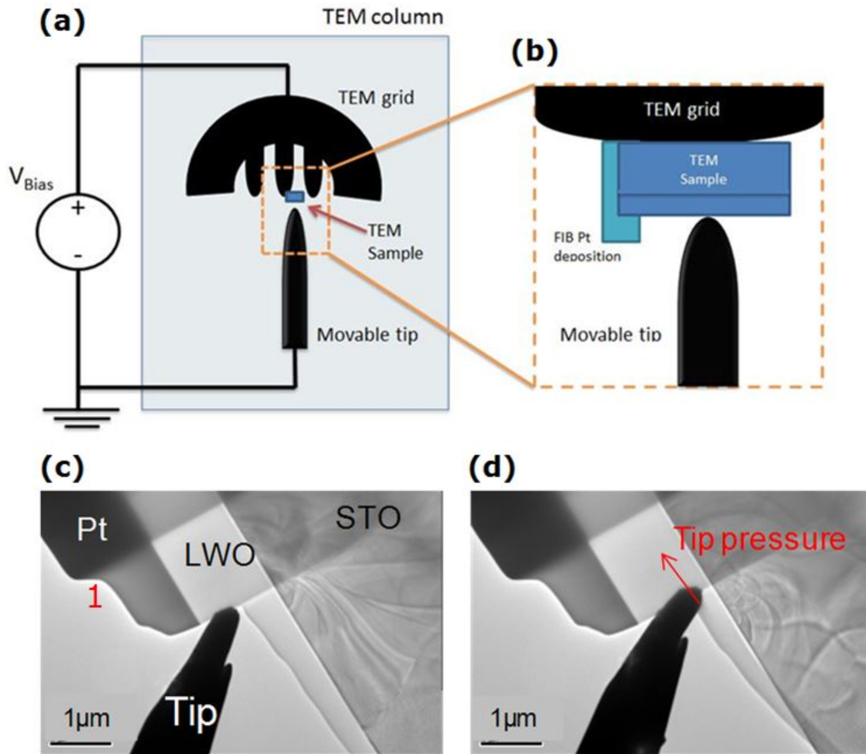

Figure 4.9 (a) Schematic representation of the *in-situ* TEM-STM system, (b) TEM image of the platinum tip contacting the sample and (c) TEM image taken during the experiment.

some mechanical stress. As it is not possible to accurately quantify the force applied with the employed TEM-STM system, we used, as a measurement unit, each mechanical step of the tip position (see figure 4.10 (a)). For each position of the movable tip of the holder, we recorded a characteristic local I-V curve (a ramp from -1V to 1V, with 400 sampling points and an acquisition time of 100 ms for the entire ramp).

The I-V red curve corresponds to the minimum force which can be applied to allow electrical contact. We observe a clear increase of the conductivity when higher pressure is applied to the LWO surface. In

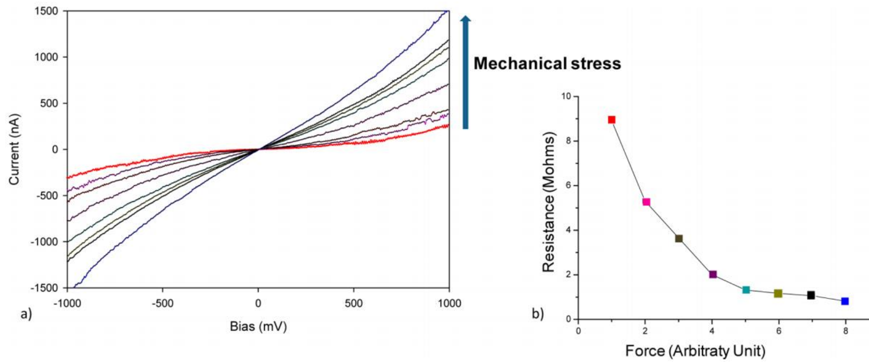

Figure 4.10 (a) I-V curves for different pressures applied by the tip to the sample. (b) Resistance vs force applied by the tip to the sample.

addition, the resistance values were calculated and plotted in Figure 4.10 (b). A decrease in the resistance, from 9 MΩ (red curve) to 800 kΩ (blue curve) is observed as more pressure is applied by the nanometric tip to the sample. In fact, we can consider that the resistance of the sample remains constant during the experiment and the changes in the current measurement are due to the electrical charge induced by the mechanical pressure.

So, the piezoelectric effect can be measured using the Ohm law as

$$V + \Delta V = I \cdot R \tag{4.1}$$

Where V is the applied voltage, ΔV the piezoelectric induced voltage, I the measured current and R the resistance of the sample. Taking into account the equation 4.1, ΔV can be plotted as a function of the force applied with the tip (see figure 4.11).

Although recent publications have reported mechanical pressure induced changes in signals and bias induced ionic motion [19,20], this effect can be considered negligible for this type of electrical resistance measurements.

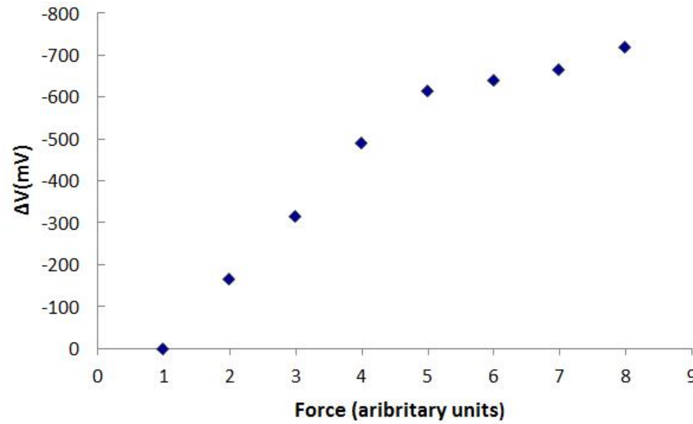

Figure 4.11 Piezoelectric induced voltage vs force applied by the tip to the sample.

Thus, the evolution of the resistance measurements during the experiment is a direct effect of the internal generation of electrical charge resulting from the applied mechanical pressure with the tip, demonstrating the piezoelectricity that occurs in the LWO thin film.

4.7 Ferroelectricity *in-situ* characterization

The TEM-STM system was also applied to study the ferroelectricit behavior of α-LWO thin films. Figure 4.12 shows a half-cycle of the hysteresis switching current, obtained with the I-V measurement method by applying the minimum pressure that allows electrical contact. In this measurement, a ramp from -1V to 1V, with 4000 sampling points and an acquisition time of 100 ms for the entire ramp was applied. Interestingly, a jump of the current value for a 620 mV bias voltage is observed. In fact, this jump is predicted for a ferroelectric film when the applied voltage is close to the coercive level [21]. This current peak corresponds to the dipole-reorientation contribution of

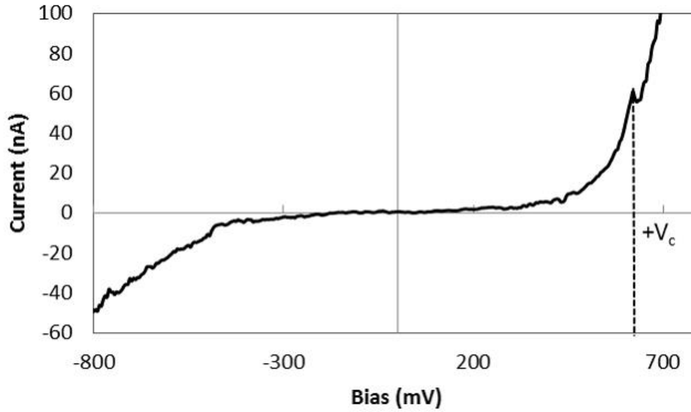

Figure 4.12 Half-cycle of the hysteresis switching current obtained with the I–V measurement method by applying the minimum pressure allowing electrical contact.

the ferroelectric material, which is a signature of ferroelectricity in the α-LWO layer.

Thus, the TEM-STM system has been used to assess the piezoelectric and ferroelectric behavior of $\alpha - LWO$ thin films, in good agreement with the results obtained with AFM.

4.8 Conclusions

In this chapter, the piezoelectric and ferroelectric properties of α-LWO thin films grown on a (001)-oriented STO substrate by PLD are assessed for first time by *in-situ* TEM.

A decrease of the resistance is observed as pressure is applied from the TEM-STM tip. This effect can be ascribed to a ΔV produced by the piezoelectricity, confirming the local piezoelectric behavior of the α-LWO thin films. Besides, ferroelectricity has been confirmed from the cycle of the hysteresis switching current using the I-V method.

This new lead-free α-LWO phase, stabilized as a thin film, can be considered as a promising candidate for nanodevice applications.

Although the TEM-STM system has been used for a qualitative measurement due to the lack of an integrated force sensor, this study demonstrates that *in-situ* TEM techniques are a powerful tool for the study of piezoelectricity and ferroelectricity of nanomaterials and opens a wide range of possibilities for future experiments.

The work presented in this chapter was published in ACS Appied Materials & Interfaces in 2015 [18].

4.9 References

[1] J. Curie and P. Curie, “Développement, par pression, de l’électricité polaire dans les cristaux hémièdres à faces inclinées,” Comptes rendus l ’Académie des Sci., vol. 91, pp. 294–295, 1880.

[2] G. Lippmann, “Principe de la conservation de l’électricité , ou second principe de la théorie des phénomènes électriques,” Physic Theory Appl., vol. 10, no. 1, pp. 381–394, 1881.

[3] J. Curie and P. Curie, “Contractions et dilatations produites par des tensions électriques dans les cristaux hémièdres à faces inclinées,” Comptes rendus l ’Académie des Sci., vol. 93, p. 1137, 1881.

[4] J. Valasek, “Piezo-electric and allied phenomena in Rochelle salt,” Phys. Rev., vol. 17, no. 4, pp. 475–481, 1921.

[5] G. H. Haertling, “Ferroelectric ceramics: history and technology,” J. Am. Ceram. Soc., vol. 82, no. 4, pp. 797–818, 1999.

[6] J. H. He, C. L. Hsin, J. Liu, L. J. Chen, and Z. L. Wang, “Piezoelectric gated diode of a single ZnO nanowire,” Adv. Mater., vol. 19, no. 6, pp. 781–784, 2007.

[7] R. Zhang, H. Andersson, M. Olsen, M. Hummelgård, S. Edvardsson, H. E. Nilsson, and H. Olin, “Piezoelectric gated ZnO nanowire diode studied by in situ TEM probing,” Nano Energy, vol. 3, pp. 10–15, 2014.

[8] M. Okayasu, T. Ogawa, and Y. Sasaki, “In situ TEM observations of microstructural characteristics of lead zirconate titanate piezoelectric ceramic during heating to 1000 °C,” Ceram. Int., vol. 43, no. 18, pp. 16306–16312, 2017.

[9] H. S. Tzou, H. J. Lee, and S. M. Arnold, “Smart materials, precision sensors/actuators, smart structures, and structronic systems,” Mech. Adv. Mater. Struct., vol. 11, no. 4–5, pp. 367–393, 2004.

[10] B. Sahoo, V. A. Jaleel, and P. K. Panda, “Development of PZT powders by wet chemical method and fabrication of multilayered stacks/actuators,”

Mater. Sci. Eng. B Solid-State Mater. Adv. Technol., vol. 126, no. 1, pp. 80–85, 2006.

[11] B. Sahoo and P. K. Panda, "Dielectric, ferroelectric and piezoelectric properties of (1 - X)[$Pb_{0.91}La_{0.09}(Zr_{0.60}Ti_{0.40})O_3] - x[Pb(Mg_{1/3}Nb_{2/3})O_3], 0 \leq x \leq 1$," J. Mater. Sci., vol. 42, no. 12, pp. 4270–4275, 2007.

[12] A. Senthil Kumaran, S. Moorthy Babu, S. Ganesamoorthy, I. Bhaumik, and A. K. Karnal, "Crystal growth and characterization of $KY(WO_4)_2$ and $KGd(WO_4)_2$ for laser applications," J. Cryst. Growth, vol. 292, no. 2, pp. 368–372, 2006.

[13] P. Lacorre, F. Goutenoire, O. Bohnke, R. Retoux, and Y. Lallgant, "Designing fast oxide-ion conductors based on $La_2Mo_2O_9$," Nature, vol. 404, no. 6780, pp. 856–858, 2000.

[14] K. S. Knight, "The Crystal Structure of Russellite; a Re-Determination Using Neutron Powder Diffraction of Synthetic Bi_2WO_6," Mineral. Mag., vol. 56, no. 384, pp. 399–409, 1992.

[15] H. J. Borchardt and P. E. Bierstedt, "Ferroelectric rare-earth molybdates," J. Appl. Phys., vol. 38, no. 5, pp. 2057–2060, 1967.

[16] M. Yoshimura and A. Rouanet, "High temperature phase relation in the system $La_2O_3 - WO_3$," Mater. Res. Bull., vol. 11, no. 2, pp. 151–158, 1976.

[17] M.-H. Chambrier, S. Kodjikian, R. M. Ibberson, and F. Goutenoire, "Ab - initio structure determination of β-La_2WO_6," J. Solid State Chem., vol. 182, p. 209, 2009.

[18] T. Carlier, M.-H. Chambrier, A. Ferri, S. Estradé, J.-F. Blach, G. Martín, B. Meziane, F. Peiró, P. Roussel, F. Ponchel, D. Rèmiens, A. Cornet, and R. Desfeux, "Lead-free α-La_2WO_6 ferroelectric thin films," ACS Appl. Mater. Interfaces, vol. 7, no. 44, pp. 24409–24418, 2015.

[19] Y. Yan, L. Wang, J. Xue, and H.-C. Chang, "Ion current rectification inversion in conic nanopores: Nonequilibrium ion transport biased by ion selectivity and spatial asymmetry," J. Chem. Phys., vol. 138, no. 4, p. 44706, 2013.

[20] K. Doi, M. Tsutsui, T. Ohshiro, C.-C. Chien, M. Zwolak, M. Taniguchi, T. Kawai, S. Kawano, and M. Di Ventra, "Nonequilibrium Ionic Response of Biased Mechanically Controllable Break Junction (MCBJ) Electrodes," J. Phys. Chem. C, vol. 118, no. 7, pp. 3758–3765, 2014.

[21] H. Kohlstedt, N. A. Pertsev, J. Rodríguez Contreras, and R. Waser, "Theoretical current-voltage characteristics of ferroelectric tunnel junctions," Phys. Rev. B, vol. 72, no. 12, p. 125341, 2005.

Chapter 5

Electrical anisotropy in ordered GaInP

5.1 III-V compounds

The III-V compounds are semiconductors combining elements of the third and fifth groups of the periodic table, such as gallium arsenide and indium antimonite. Many binary and ternary naturally occurring compounds were known to exhibit a behavior now associated with semiconducting properties long before the invention of the transistor. Nevertheless, it was this development that stimulated systematic searches for new semiconductors in the early 1950s. The first materials investigated in this manner were the diamond structure III-V compounds. Although in 1950 Blum et al. and Goryunova and Obukhov [1] reported InSb to be a semiconductor, Welker was the first

one to appreciate the importance of III-V compounds as a new class of semiconductor in 1952 [2].

III-V semiconductors have been explored as active materials for high-speed electronic devices, many types of opto-electronic and high-efficiency photovoltaic devices. The widespread use of III-V semiconductors is due to the inherent advantages of direct bandgap and high electron mobility.

In recent years *in-situ* electron microscopy has become a very significant tool contributing to the optimization of III-V based modern nanodevices. In 2011, the Ross group [10] reported the *in-situ* growth of nanowires of one particular III-V semiconductor, GaP, in a TEM, using the precursor gases trimethylgallium and phosphine. In 2014, F. Lenrick et al. [11] studied the *in-situ* growth of InAs nanowires using a closed cell in a conventional TEM with a heating holder. Moreover, V. T. Fauske et al.[12] performed the electrical characterization of individual GaAs nanowires by using *in-situ* SEM probing. More recently, in 2017, R. Straubinger et al.[13] reported *in-situ* thermal annealing in the TEM of III-V semiconductor heterostructures in different environments. Hence, *in-situ* TEM studies on III-V compounds can lead to an understanding of the structural properties of nanostructures allowing the improvement of new advanced optoelectronic devices.

In this chapter, the anisotropic electrical conductivity of GaInP will be assessed by using *in-situ* biasing TEM. The electrical conductivity of GaInP thin films with a different degree of order (controlled by the amount of Sb flux used during the growth) will be measured in the orthogonal [110] and [1-10] directions and the differences discussed in view of the antiphase boundaries present in the layer.

5.2 GaInP for multi-junction solar cells (MJSC)

Recently, III-V semiconductor compounds are receiving much attention because of their efficiency in III–V multi-junction solar cells (MJSC). The III-V semiconductor family possesses a number of attractive properties for fabricating solar cells. The bandgaps of the binary III-V semiconductors are conveniently scattered around the solar spectrum with further bandgap tuning possible through ternary or quaternary alloys. The majority of III-V materials have direct bandgaps, leading simultaneously to large absorption coefficients for photons with energies in excess of the bandgap and short radiative lifetimes [3].

To date, the best III–V compound triple-junction and four-junction solar cells have attained conversion efficiencies of up to 44.4 and 46% under concentrated light, respectively [4,5]. To further increase the conversion efficiency it is necessary to enhance light absorption, increase carrier collection, or reduce energy loss due to thermalization. Several strategies have been proposed to increase the conversion efficiency in III–V MJSC [6–9]. For example, a new material engineering technique has been developed for maintaining high thermal homogeneity at the wafer surface, which expands the bandgap engineering possibilities for improving the efficiency in III–V MJSC [8]. Also, metal nanoparticles have been introduced on the illuminated surface of III–V multi-junction solar cells for producing strong light scattering and light trapping, which is beneficial for carrier generation in the absorbing region [6,7]. A 15% increase of conversion efficiency has been implemented by introducing Au nanoclusters on top of the III–V multi-junction solar cells [7].

GaInP is a key material in III-V MJSCs. GaInP presents a CuPt ordering in the group III sublattice, as many other III-V ternaries.

This ordering consists of alternating Ga- and In-rich planes on the four equivalent 111 planes of the zinc-blende structure (figure 5.1). Misorientation of the (001) substrate by a few degrees towards (111) favors the formation of a single GaInP variant, exhibiting ordering only on the (-111) and (1-11) planes ($CuPt_B$ type).

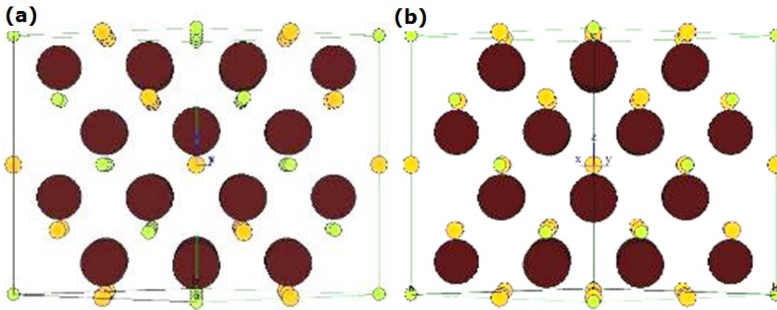

Figure 5.1 Crystal structure of GaInP for (a) [110] and (b) [-110] zone axes.

The electrical and optical properties of GaInP are influenced by the ordered domains as the presence of these domains leads to anisotropy in the minority carrier diffusion length as well as in the layer conductivity and reduces carrier mobility. Surfactants, such as Sb, among others, can be used to control the degree of order (related with the energy bandgap (E_g) of the alloy) without changing other process variables. Nevertheless, to further increase the performance of the aforementioned devices, a deep understanding of the relationship between the growth conditions and the electrical properties of the devices is mandatory.

5.3 Sb-flux assisted growth of GaInP

The GaInP sample growth and optical porperties determination were performed by the group of Prof. Carlos Algora from the Institute of Solar Energy of Universidad Politécnica de Madrid (IES-UPM).

GaInP semiconductor structures were grown in a commercial horizontal MOVPE reactor (Aixtron AIX200/4) equipped with an *in-situ* reflectance anisotropy (RA) spectrometer (Laytec EpiRAS 200) on Ge(001) substrates with 6° misorientation towards the nearest [111] direction [14]. The Sb precursor employed was TESb. They all consist of a 365nm-thick GaInP nucleation layer, followed by a Zn doped, 1100 nm-thick GaInP layer (where different amounts of Sb were introduced into the reactor to promote surfactant mediated growth) and a 400 nm-thick GaInAs overbuffer. Layers were grown at 675°C, a V/II ratio of 120 and a growth rate of 0.60nm/s. Figure 5.2 depicts a cross-section sketch of the GaInP structure under study.

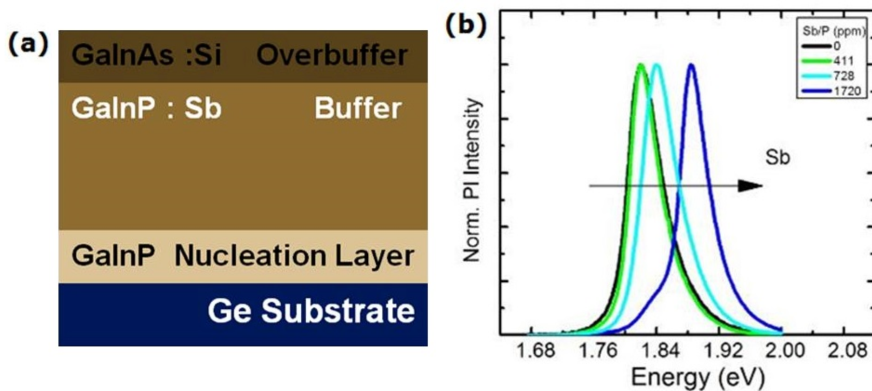

Figure 5.2 (a) Cross-section sketch of the GaInP structure under study on Ge substrate. (b) Normalized PL measurements at RT of GaInP TC base layers with different amounts of Sb.

In order to control the degree of order of GaInP structures using Sb as a surfactant, a preliminary study was carried out. Preliminary PL measurements were performed on layers grown with different Sb/P ratios. Figure 5.2(b) shows how the peak position shifts from 1.819 eV up to 1.884 eV [15,16].

In view of these results, it is confirmed that the amount of Sb modulates the degree of order in GaInP. In this sense, an order

parameter is defined as η. η is estimated from the variation of the energy bandgap of an alloy with respect to the gap of the disordered material according to the equation [17],

$$E_g(\eta) = E_g(\eta = 0) - \eta^2 \Delta E_g \tag{5.1}$$

where ΔE_g is the bandgap reduction of the fully ordered alloy, which has been experimentally determined to be 471 meV [18]. Accordingly, the order parameter can be inferred from the energy position of the PL peak as

$$\eta = \sqrt{\frac{1991 - PL\,at\,20K(meV)}{471}} \tag{5.2}$$

where 1991 meV is the estimated energy bandgap of a completely disordered GaInP layer at 20 K grown lattice-matched on a Ge substrate [15].

Table 5.1 summarizes the samples analyzed with the employed Sb/P ratios, together with the energy bandgap determined from the PL peak energy at 20K, and their η (order parameter) value.

Sb/P	$\boldsymbol{\eta}$	$\mathbf{E_g}$**(eV)20K**
0	0.53	1.855
411	0.48	1.880
728	0.44	1.904
1721	0.31	1.949

Table 5.1 Order parameter and value of the PL peak energy at 20K for the Sb/P ratio in the vapour phase for the GaInP samples grown.

5.4 General TEM characterization

TEM images of the GaInP structures were acquired in a cross-section configuration from specimens prepared by FIB using the lift-out technique.

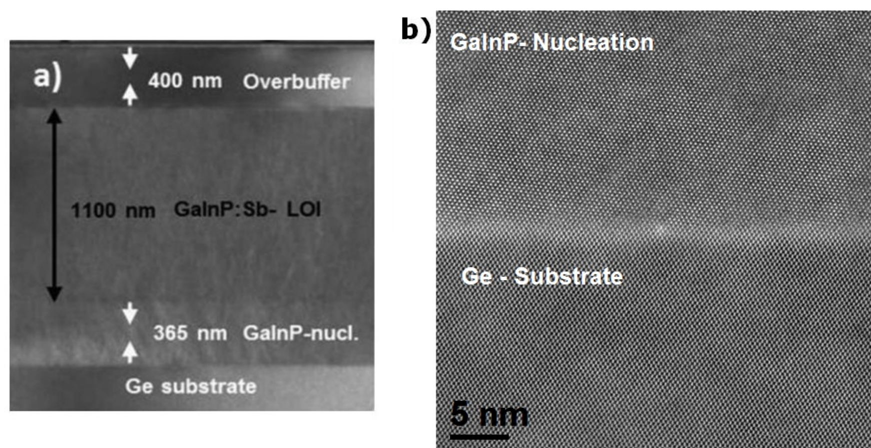

Figure 5.3 (a) TEM image of the cross-section of the structure and (b) HAADF-STEM image of the Ge-substrate/GaInP Nucleation layer interface

Figure 5.3 (a) depicts a low magnification bright field TEM image of the sample showing, on top of the Ge-substrate, the GaInP nucleation layer, the GaInP buffer grown with the Sb surfactant with layer thicknesses of 365 nm and 1100 nm, respectively, and the 400 nm thick GaInAs overbuffer.

From HAADF-STEM images (figures 5.3 (b) and 5.4) we can confirm the high quality of all samples. No trace of anti-phase domains was observed for any sample at the GaInP/Ge heterointerface as shown in figure 5.3 (b). Therefore, we can discard any influence of the III/V/IV heteroepitaxy in the microstructure of the upper layers grown using Sb. In addition, no evidence of GaInP decomposition was found in any of the examined samples. This was avoided by the use of relatively low Sb/P ratios and high growth rates [19]. Moreover, the alternating In-rich and Ga-rich planes can be observed through the Z-contrast STEM-HAADF using aberration corrected instruments in figure 5.4[1].

[1]FEI TITAN[3], equipped with a high brightness Schottky field emission gun (X-FEG) and a condenser lens Cs corrector, 80 kV-300 kV. Located at École Centrale des Arts et Manufactures, Paris.

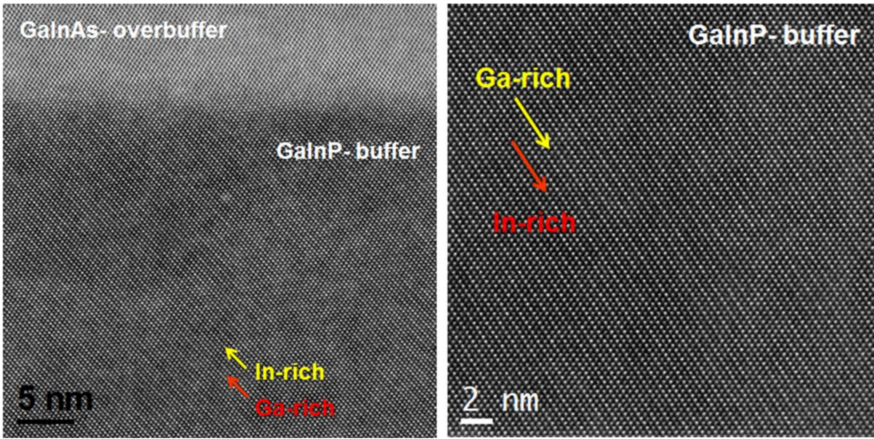

Figure 5.4 HAADF-STEM image of GaInP structure obtained along the [110] zone axis.

5.5 TEM study of the order parameter

In order to study the effect of the Sb/P ratio on the degree of order in the GaInP structures, samples were studied in the two orthogonal [110] and [1-10] cross-section directions. Hereafter, the observed along [110] zone axis will be refered to as [A] oriented samples, and the [1-10] as [B] oriented samples. The cross-section TEM lamellas were prepared by FIB using the lift-out technique. Figure 5.5 shows a SEM image obtained during the preparation in the two orthogonal directions.

Figure 5.6 shows the selected area electron diffraction (SAED) patterns in [A] and [B] orientations for each sample with different Sb/P ratios employed. As can be seen, all samples observed in the [B] zone axis show the expected pure zinc-blende pattern. In contrast, SAED patterns of all samples oriented in the [A] direction present extra satellite spots at positions $(h \pm \frac{1}{2}, k \mp \frac{1}{2}, l \pm \frac{1}{2})$. These results show the existence of a $CuPt_B$ ordering in the (1-11) plane with only one variant for all samples, which indicates that Sb does not change the

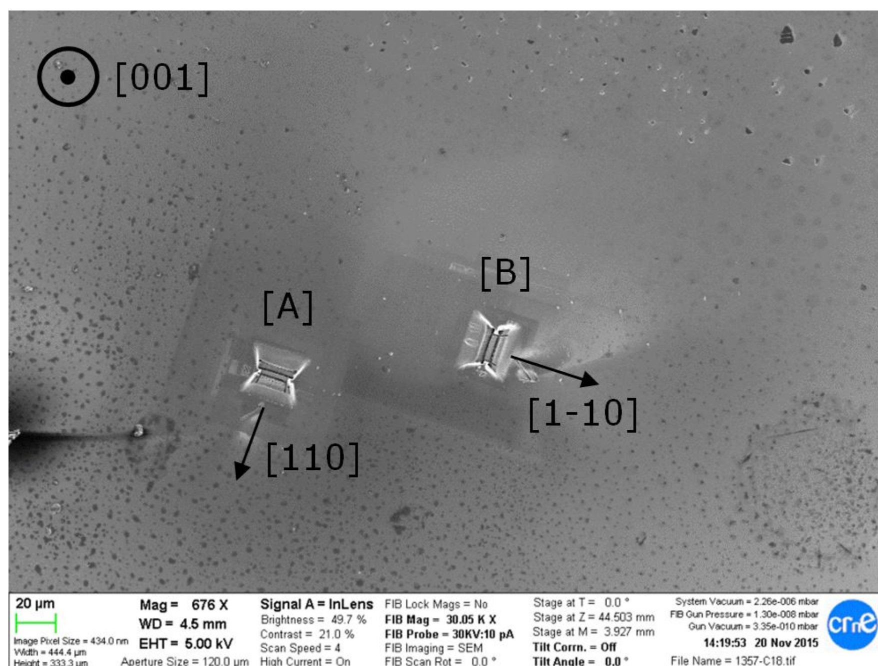

Figure 5.5 SEM image of the sample during the TEM lamella preparation in the two orthogonal [110] and [1-10] cross-section TEM orientations.

type of ordering, as expected for GaInP grown on a highly misoriented substrate.

Moreover, the variations in the degree of order amongst the different samples can be qualitatively inferred by comparing the ratio of intensities between the $\frac{1}{2}(111)$ superlattice spots and the usual zinc-blende spots in the same diffraction pattern. As the Sb/P ratio is increased, the relative intensity of the $\frac{1}{2}(111)$ spot becomes weaker, which indicates that Sb is actually decreasing the degree of order. This is in good agreement with the decrease in η with the Sb/P ratio presented in Table 5.1.

Several studies have shown that the microstructure of ordered GaInP consists of domains of an ordered material with uniform phase separated by antiphase boundaries (APBs) [20-23]. Figure

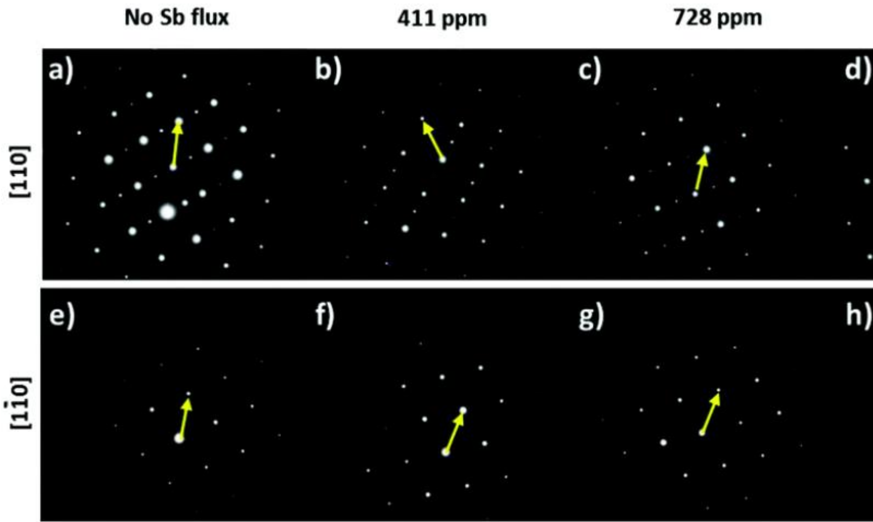

Figure 5.6 Comparison of the selected area diffraction patterns of the structures along the [110] zone axis (top panels) and [1-10] zone axis (bottom panels) as a function of the employed Sb/P ratio. Notice the superstructure reflections between the main spots in the direction parallel to g = (1-11) in only the [011] zone axis diffraction patterns. The yellow arrow indicates the [001] direction in all cases.

5.7 shows the dark field electron microscopy images obtained using the satellite spot $(\frac{1}{2}, \frac{1}{2}, \frac{1}{2})$ for different Sb/P ratios. All samples present a single-variant order domain structure separated by APB dark stripes. The bright regions are considered as domains of a given η parameter and the dark regions, their boundaries, where antiphase domains meet and overlap [24]. In our samples, the extension angle of the APBs (the angle of APB with respect to the plane of the interface) has been directly correlated with the use of Sb, yielding values even higher than 90º. Figure 5.7 (d) shows the evolution of the average value of APB angle vs. the Sb/P ratio employed.

More quantitative measurements concerning the domain size were also carried out. The average domain width is measured as the average horizontal extension of a domain limited by the dark stripes of the APBs. Domain size is found to vary from 45nm to 110 nm (from the

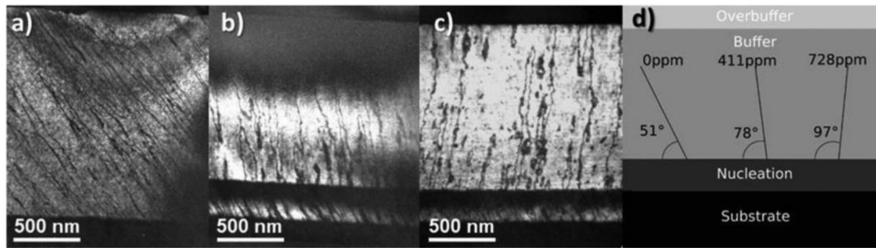

Figure 5.7 Dark field TEM images obtained along the [110] zone axis using the satellite spot g = $(\frac{1}{2}, -\frac{1}{2}, \frac{1}{2})$ (a) with no Sb; (b) with an Sb/P ratio of 411 ppm; (c) with an Sb/P ratio of 728 ppm. (d) Schematic representation of the change in orientation of ordered domains (angle θ_{APB} as a function of the Sb/P ratio).

interface to the upper surface) for all Sb fluxes. Given the variation of APB density between the different samples, it was interesting to study the dependence of the anisotropy of the conductivity of GaInP structures with respect to the degree of order and the presence of APBs.

5.6 Electrical characterization

Once the relationship between the order parameter and the Sb/P ratio is assessed, the anisotropy of the conductivity can be studied. The local conductivity of both [A] and [B] oriented samples was measured for each Sb/P ratio by *in-situ* TEM. A ramp from 1V to -1V, with 400 sampling points and an acquisition time of 100 ms for the entire ramp was used to measure the electrical resistance (R) of each GaInP structure in both directions.

Figure 5.8 shows the set-up for the *in-situ* experiments. As can be seen in the figure, a path was milled with FIB in order to control the current flow through the GaInP:Sb layer. The Pt tip of the TEM-STM holder was carefully approached to the interesting part of the sample, the GaInP:Sb layer, in order to perform the electrical measurements.

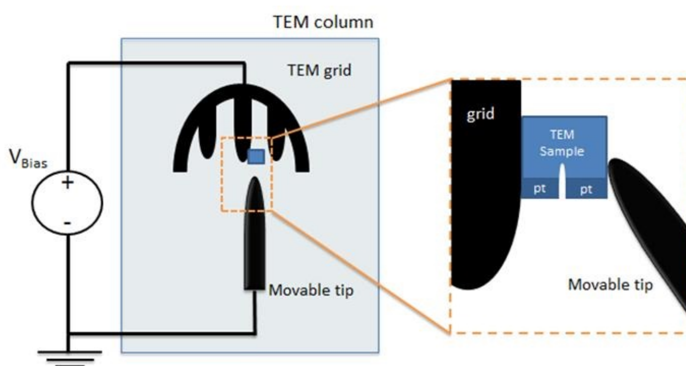

Figure 5.8 Schematic representation of the *in-situ* TEM-STM system.

In order to study the anisotropic behaviour of the electrical conductivity of the GaInP structures, the degree of the anisotropy was calculated as the ratio between the resistivity in the [A] oriented sample and the resistivity of the [B] oriented sample for three samples grown with different Sb/P ratios.

It is worth to mention now that the current flows through the [1-10] direction in the case of the [A] oriented lamella preparation and along [110] direction in the [B] oriented sample. For this reason, from now on we will name these ρ values as $\rho_{[1-10]}$ and $\rho_{[110]}$.

The resistivity (ρ) was calculated from R measurements using the geometric parameters of the GaInP structures obtained from the TEM images (as an example, see Figure 5.8 (b)) and considering the thickness of the TEM lamella to be 100 nm (see table 5.2).

Figure 5.9 shows the graphical representation of the ratio of resistivities vs the Sb/P ratio. As can be seen in the figure, as the Sb/P ratio increases, the change in the resistivity between the [1-10] and [110] directions decreases, or in other words, as the degree of order decreases the anisotropy of the electrical conductivity decreases too.

Sb/P (ppm)	$R_{[1\bar{1}0]}$ ($M\Omega$)	$R_{[110]}$ ($M\Omega$)	$\rho_{[1\bar{1}0]}$ ($\Omega \cdot m$)	$\rho_{[110]}$ ($\Omega \cdot m$)	$\frac{\rho_{[1\bar{1}0]}}{\rho_{[110]}}$	η
0	15.2	3.4	63.7	11.5	5.54	0.53
411	10.9	3.5	43.9	10.6	4.14	0.48
1721	1.5	1.4	5.46	4.95	1.10	0.29

Table 5.2 Important parameters: Sb/P ratio, resistance in direction [1-10] ($R_{[1\bar{1}0]}$), resistance in direction [110] ($R_{[110]}$), resistivity in direction [1-10] ($\rho_{[1\bar{1}0]}$), resistivity in direction [110] ($\rho_{[110]}$), ratio between the resistivity in the [1-10] direction and the resistivity in the [110] direction ($\frac{\rho_{[1\bar{1}0]}}{\rho_{[110]}}$) and order parameter ($\eta$).

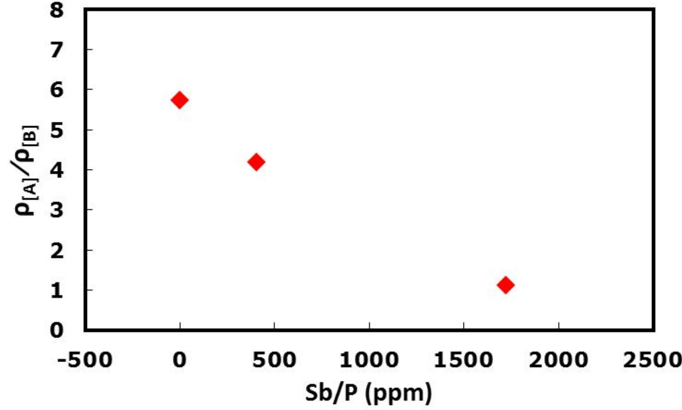

Figure 5.9 Ratio of the resistivities along the [1-10] and [110] directions as a function of the Sb/ratio.

Furthermore, the resistivity increases with the order parameter when the current flows perpendicular to the APBs (i.e. $\rho_{[1-10]}$), and it is kept relatively independent from the order parameter when the current flows parallel to the APBs (i.e. $\rho_{[110]}$). This is an important result, as it shows the role of the APBs as recombination centers, and offers a direct insight into the electrical anisotropy of the system.

Thus, from the direct measurement of the local conductivity of GaInP structures using *in-situ* TEM, the dependence of the anisotropy behavior with the Sb/P ratio, and, therefore, with the order parameter,

has been demonstrated. In fact, these results are totally consistent with the macroscopic study of the tranport anisotropy in GaInP structures presented by Chernyak et al. in 1997 [25]. They attributed the observed anisotropy to the ordered domain boundary scattering and noted that the higher band gap associated with domain boundaries could act as a barrier and affect the diffusion length.

5.7 Conclusions

In this chapter, the ordering of GaInP layers grown with different amounts of Sb/P ratio in the gas phase during the epitaxial growth by MOVPE on Ge(001) substrates with a 6° misorientation towards the nearest [111] axis has been shown. The type of ordering observed is $CuPt_B$ single variant and it is unaffected by the use of Sb during the epitaxial growth. The relative intensities of the satellite spots becomes weaker with increasing Sb flux, in good agreement with the reduction of the order parameter as determined from previous PL measurements.

Moreover, with *in-situ* TEM, the anisotropy of the conductivity between [110] and [1-10] orthogonal directions has been assessed. From the electric measurements through the GaInP:Sb layer for the two orthogonal [A] and [B] oriented samples, it has been observed that, as the degree of order decreases, the anisotropy of the electrical conductivity decreases too. Furthermore, we have shown that the resistivity increases with the order parameter when the current flows perpendicular to the APBs, and it is kept relatively independent from the order parameter when the current flows parallel to the APBs.

A publication concerning the results in this chapter is currently under preparation.

5.8 References

[1] J. L. Joseph L. Shay and J. H. Jack H. Wernick, Ternary chalcopyrite semiconductors: growth, electronic properties, and applications, vol. 7. Pergamon Press, 1975.

[2] H. Welker, "Über neue halbleitende Verbindungen II," Zeitschrift fur Naturforsch. - Sect. A J. Phys. Sci., vol. 8, no. 4, pp. 248–251, 1953.

[3] N. J. Ekins-Daukes, "III-V solar cells," in Solar Cell Materials: Developing Technologies, Chichester, UK: John Wiley & Sons, Ltd, pp. 113–143, 2014.

[4] T. N. Lin, S. R. M. S. Santiago, J. A. Zheng, Y. C. Chao, C. T. Yuan, J. L. Shen, C. H. Wu, C. A. J. Lin, W. R. Liu, M. C. Cheng, and W. C. Chou, "Enhanced conversion efficiency of III–V triple-junction solar cells with graphene quantum dots," Sci. Rep., vol. 6, no. 1, p. 39163, 2016.

[5] M. A. Green, K. Emery, Y. Hishikawa, W. Warta, and E. D. Dunlop, "Solar cell efficiency tables (Version 45)," Prog. Photovoltaics Res. Appl., vol. 23, no. 1, pp. 1–9, 2015.

[6] L. Yang, S. Pillai, and M. A. Green, "Can plasmonic Al nanoparticles improve absorption in triple junction solar cells?," Sci. Rep., vol. 5, no. 1, p. 11852, 2015.

[7] M. D. Yang, Y. K. Liu, J. L. Shen, C. H. Wu, C. A. Lin, W. H. Chang, H. H. Wang, H. I. Yeh, W. H. Chan, and W. J. Parak, "Improvement of conversion efficiency for multi-junction solar cells by incorporation of Au nanoclusters.," Opt. Express, vol. 16, no. 20, pp. 15754–15758, 2008.

[8] G. Timò, G. Abagnale, N. Armani, E. Malvisi, G. Carbi, F. Farina, and B. Schineller, "Novel approaches to MOVPE material deposition for high efficiency Multijunction Solar Cells," in Crystal Research and Technology, vol. 49, no. 8, pp. 606–613, 2014.

[9] F. Dimroth, M. Grave, P. Beutel, U. Fiedeler, C. Karcher, T. N. D. Tibbits, E. Oliva, G. Siefer, M. Schachtner, A. Wekkeli, A. W. Bett, R. Krause, M. Piccin, N. Blanc, C. Drazek, E. Guiot, B. Ghyselen, T. Salvetat, A. Tauzin, T. Signamarcheix, A. Dobrich, T. Hannappel, and K. Schwarzburg, "Wafer bonded four-junction GaInP/GaAs//GaInAsP/GaInAs concentrator solar

cells with 44.7% efficiency," Prog. Photovoltaics Res. Appl., vol. 22, no. 3, pp. 277–282, 2014.

[10] C. Y. Wen, J. Tersoff, K. Hillerich, M. C. Reuter, J. H. Park, S. Kodambaka, E. A. Stach, and F. M. Ross, "Periodically changing morphology of the growth interface in Si, Ge, and GaP nanowires," Phys. Rev. Lett., vol. 107, no. 2, p. 25503, 2011.

[11] F. Lenrick, M. Ek, K. Deppert, L. Samuelson, and L. Reine Wallenberg, "Straight and kinked InAs nanowire growth observed in situ by transmission electron microscopy," Nano Res., vol. 7, no. 8, pp. 1188–1194, 2014.

[12] V. T. Fauske, D. C. Kim, A. M. Munshi, D. L. Dheeraj, B.-O. Fimland, H. Weman, and A. T. J. van Helvoort, "In-situ electrical and structural characterization of individual GaAs nanowires," vol. 522, no. 1, p. 12080, 2014.

[13] R. Straubinger, A. Beyer, T. Ochs, W. Stolz, and K. Volz, "In situ thermal annealing transmission electron microscopy (TEM) investigation of III/V semiconductor heterostructures using a setup for safe usage of toxic and pyrophoric gases," Microsc. Microanal., vol. 23, no. 4, pp. 751–757, 2017.

[14] E. Barrigon, B. Galiana, and I. Rey-Stolle, "Reflectance anisotropy spectroscopy assessment of the MOVPE nucleation of GaInP on germanium (100)," J. Cryst. Growth, vol. 315, no. 1, pp. 22–27, 2011.

[15] E. Barrigón, L. Barrutia, and I. Rey-Stolle, "Optical in situ calibration of Sb for growing disordered GaInP by MOVPE," J. Cryst. Growth, vol. 426, pp. 71–74, 2015.

[16] L. Barrutia, E. Barrigón, L. López-Conesa, J. Rebled, S. Estradé, F. Peiró, I. Rey-Stolle, and C. Algora, "On the use of Sb to improve the performance of GaInP subcells of multijunction solar cells," in 2015 IEEE 42nd Photovoltaic Specialist Conference (PVSC), pp. 1–4, 2015.

[17] S. Wei, D. B. Laks, and A. Zunger, "Dependence of the optical properties of semiconductor alloys on the degree of long-range order," Appl. Phys. Lett., vol. 62, no. 16, pp. 1937–1939, 1993.

[18] P. Ernst, C. Geng, F. Scholz, H. Schweizer, Y. Zhang, and A. Mascarenhas, "Band-gap reduction and valence-band splitting of ordered GaInP," Appl. Phys. Lett., vol. 67, no. 16, pp. 2347–2349, 1995.

[19] R. T. Lee, C. M. Fetzer, S. W. Jun, D. C. Chapman, J. K. Shurtleff, G. B. Stringfellow, Y. W. Ok and T. Y. Seong, "Enhancement of compositional modulation in GaInP epilayers by the addition of surfactants during organometallic vapor phase epitaxy growth," J. Cryst. Growth, vol. 233, no. 3, pp. 490-502, 2001.

[20] Y. Ohno, "Microstructure of a CuPt-ordered GaInP alloy revealed by cross-sectional scanning tunneling microscopy," Japanese J. Appl. Physics, Part 1 Regul. Pap. Short Notes Rev. Pap., vol. 45, no. 3 B, pp. 2357–2360, 2006.

[21] G. Hahn, C. Geng, P. Ernst, H. Schweizer, F. Scholz, and F. Phillipp, "Investigations on domain boundaries in ordered GaInP using stereo transmission electron microscopy," Superlattices Microstruct., vol. 22, no. 3, pp. 301–305, 1997.

[22] E. Dobročka, I. Vávra, and L. R. Wallenberg, "Simulation of electron diffraction patterns from III-V alloys with CuPt ordering: Effect of clusters and antiphase boundaries," J. Appl. Phys., vol. 89, no. 5, pp. 2653–2664, 2001.

[23] C. S. Baxter, W. M. Stobbs, and J. H. Wilkie, "The morphology of ordered structures in III-V alloys: inferences from a TEM study," J. Cryst. Growth, vol. 112, no. 2–3, pp. 373–385, 1991.

[24] G. Hahn, C. Geng, P. Ernst, H. Schweizer, F. Scholz, and F. Phillipp, "Investigations on domain boundaries in ordered GaInP using stereo transmission electron microscopy," Superlattices Microstruct., vol. 22, no. 3, pp. 301–305, 1997.

[25] L. Chernyak, A. Osinsky, H. Temkin, A. Mintairov, I. G. Malkina, B. N. Zvonkov, Y. N. Safanov, "Transport anisotropy in spontaneously ordered GaInP alloys," Appl. Phys. Lett., vol. 70, no. 18, pp. 2425-2427, 1997.

Chapter 6

Resistive switching studies of ReRAM devices

6.1 ReRAM memories

Resistance random access memory (ReRAM) consists in a switching layer sandwiched between two electrodes, typically formed by a metal-insulator-metal (MIM) structure. The intrinsic physical phenomenon behind ReRAMs is the resistive switching (RS), which means that the device can be freely programmed into a high resistance state (HRS or OFF state) or a low resistance state (LRS or ON state) under external electrical stimuli. In most cases, the current is restricted to a local region with high conductance known as a conducting filament (CF) in the LRS and flows uniformly through the device, decreasing the conductivity, in the HRS[1,2]. The switching event from the HRS

to the LRS and the corresponding voltage are denoted as SET process and V_{SET}, respectively. In contrast, the switching event from the LRS to the HRS and the corresponding voltage are denoted as RESET process and V_{RESET}, respectively.

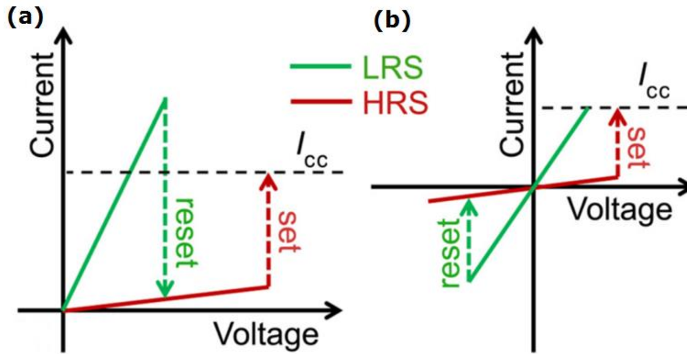

Figure 6.1 (a) Unipolar and (b) bipolar switching. Icc denotes the compliance current, which is adopted during the set process to prevent permanent breakdown.

ReRAMs can be classified into two types according to the operating electrical polarity. The 'unipolar' one, where the switching mechanism is independent of the polarity of the operating voltage, as shown in figure 6.1 (a), and the 'bipolar' one, where the set and reset processes must occur with opposite voltage polarities, as shown in figure 6.1 (b). The physical mechanism in the unipolar type is generally interpreted as a Joule heating effect, which means that the operating electrical polarity does not depend on the polarity of the operating voltage. Figure 6.2 (a) depicts an example of unipolar switching, showing the thermally activated conductive filament dissolution due to radial diffusion. In contrast, the physical mechanism in the bipolar type is typically regarded as a redox reaction and an electrochemical migration. Figure 6.2 (b) shows an example of bipolar switching by the drift of oxygen vacancies under an applied field. Hence, the operating electrical polarity depends on the polarity of the operating voltage[3].

In order to avoid a permanent breakdown of the device, a limitation of the current is typically applied. The limit of the current allowed is known as the compliance current (CC). It is an important parameter to be considered in the set process for both unipolar and bipolar ReRAMs.

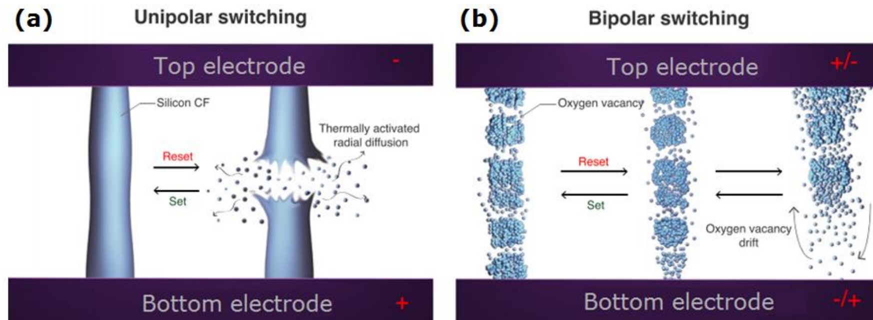

Figure 6.2 Schematic representation of (a) unipolar switching, including thermally activated conductive filament dissolution due to radial diffusion, and (b) bipolar switching by the vertical drift of oxygen vacancies under the applied field[4].

The resistive switching (RS) phenomenon was first reported in a series of binary oxides by Hickmott et al. in 1962 [5]. Hickmott observed large negative differential resistance in five thin anodic oxide films including SiO_x, Al_2O_3, Ta_2O_5, ZrO_2 and TiO_2. Subsequently, more materials were demonstrated to show RS, and the switching mechanisms started to be explored as well.

Since the late 1990s, the interest in RS was reignited in the search for an alternative to Si-based memories. The first practical application of ReRAMs was reported by Zhuang et al.[6]. They fabricated a 64-bit ReRAM based on $Pr_{0.7}Ca_{0.3}MnO_3$ using a CMOS process.

In recent years, the range of suitable materials for ReRAMs has been expanded to metal oxides such as TiO_2 [7], $SrTiO_3$ [8,9], NiO [10], CuO [11], ZnO [12], MnO_x [13], HfO_x [14], Ta_2O_5 [15]. ReRAMs based on chalcogenides [16], polymers [17], atomic switches [18], spintronic

systems [19] and quantum systems [20] can also be found in the literature. Biological materials and mechanisms such as sweat ducts [21], leaves [22], blood [23], slime mould [24], synapses [25] and neurons [26] are also described as memristive.

On the other hand, the most critical problem for the development of ReRAM technology is the detailed understanding of both the mechanisms of conductive filament formation and switching mechanism. The nanometric nature of the switching region and its random location in the device make it extremely difficult to characterize. In this sense, *in-situ* TEM has been demonstrated as a valuable tool to explore ReRAMs switching mechanisms.

Interestingly, the detailed nucleation and growth processes of conducting filaments have been directly recorded by *in-situ* TEM in some materials. In this sense, D.H. Kwon et al. [27] demonstrated with *in-situ* biasing and high resolution TEM (HRTEM) studies that in Pt/TiO_2/Pt ReRAM devices, switching occurs by the formation and disruption of Ti_nO_{2n-1} filaments of Magnéli phase. Also using *in-situ* TEM, Q. Liu et al. [28] obtained in ZrO_2 based ReRAM devices real-time observations of the CF formation and dissolution processes, based on a local redox reaction inside the ZrO_2-electrolyte system. X. Wu et al. [29,30] observed the formation and dissolution of nanofilaments in Ni/HfO_2 based ReRAM devices by TEM in real time, showing oxygen ion drift and a subsequent Ni diffusion/migration into the dielectric and the substrate from the top electrode. The Reset process was associated with the partial dissolution of the CFs due to thermally enhanced diffusion of Ni atoms induced by Joule heating[29,30]. Thus, *in-situ* studies have been proved to be a useful tool to improve the understanding of the ReRAMs switching mechanisms[31-34].

In this chapter, three different ReRAM systems and the structural and chemical modifications at the nanoscale after CF formation and SET, RESET cycling will be analyzed by TEM in: (1) silicon-aluminium oxynitride (SiAlON) thin films grown by pulsed laser deposition (PLD); (2) a HfO_2 based ReRAM inkjet-printed structure; and, finally, (3) a Ni/HfO_2/Si structure grown by Atomic Layer Deposition (ALD).

6.2 Al/SiAlON/Si

The SiAlON structure was grown and electrically characterized by the group of Prof. Blas Garrido at the Electronic and Biomedical Engineering Department of UB. The SiAlON ReRAM sample consists of a SiAlON layer and an Al electrode grown onto a p-type (100)-Si substrate (see figure 6.3).

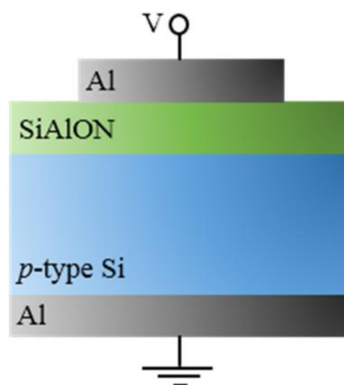

Figure 6.3 Cross-section sketch of the SiAlON ReRAM structure.

Here, the main objective of the TEM characterization is the elucidation of the forming mechanism of CF in SiAlON ReRAM structures under real operation conditions. The electroforming was made *ex-situ*, at device level, and then the samples were characterized

by TEM in order to correlate the macroscopic effects of the CF formation with the CF nanoscale features.

6.2.1 Sample growth

SiAlON thin films (140 nm-thick) were grown onto p-type (100)-Si substrates by means of pulsed laser deposition (PLD). The ablation of the SiAlON target was carried out at room temperature in a base pressure of 1×10^{-6} mbar, using a 193 nm ArF-excimer laser with a pulse duration of 20 ns and at an energy density of 4.1 $J \cdot cm^{-2}$ per pulse. After deposition, the films were submitted to an annealing process at 700 °C in air. X-ray photoelectron spectroscopy measurements determined a SiAlON composition of Si (45%), Al (3%), N (40%) and O (12%) [35]. The device structure was completed by fabricating a vertical Metal-Insulator-Semiconductor (MIS) structure, where the metal, insulator and semiconductor materials were Al, SiAlON and the Si substrate, respectively. The top and bottom electrode metallizations were done via electron beam evaporation of Al, where the top electrode was properly patterned in the form of 150 µm-diameter circular dots by using a chromium shadow mask, whereas a full-area Al deposition was applied on the rear side of the Si substrate.

6.2.2 Electrical characterization

The electrical characterization of the devices was performed by means of an Agilent B1500 semiconductor device analyser and a Cascade Microtech Summit 1100 probe station, where the devices under study are screened from external electromagnetic fields by a Faraday cage.

This hardware-software combined system is suitable for switching characterization thanks to the possibility to set a protocol using the current-voltage (I-V) sweep mode, with a compliance current when necessary.

To elicit the memristive behaviour, first of all the electroforming process was produced in the SiAlON devices and, afterwards, the two resistive states were obtained using voltage ramps at different polarizations. Figure 6.4 shows the electroforming process in the device, which exhibits characteristic ramps due to the switching between the high and the low resistance states. Note that the current is represented in logarithmic scale due to the huge resistance ratio between both states. The switching between the two resistive states describes a cycle where the following regions can be defined and are labelled in the figure: (1) the pristine device is submitted to a positive increasing ramp up to 20 V, exhibiting a highly resistive conduction. At voltages close to 20 V, (2) there is a sudden increase in the current, and, thus, the device switches from the HRS to the LRS. The current is limited to $I_{CC} =$ 0.5 mA in the device by using a variable resistor in series in order to prevent the irreversible breakdown of the device. The resistance in the LRS can only be determined once the voltage is lowered to obtain currents well below this limit, recovering the real I-V curve in the LRS. In the region labelled as (3), the current remains constant at the current compliance when reducing the voltage. At voltages below 0.1 V, (4) a linear relationship between the applied voltage and the obtained current can be observed, with a large slope that evidences the creation of conductive paths between the two electrodes; the device remains in this LRS under low negative bias. At large enough negative voltages without the limitation of the current compliance, (5) the current rapidly increases and remains independent of the applied voltage until (6) it gets abruptly reduced from the mA range to some µA. This

behaviour suggests that the conductive paths have been interrupted and the device has switched back to the HRS. At this point, (7) the I-V curve remains in this HRS, with a conduction behaviour typical of insulating materials. To complete a memristive cycle, (8) the voltage is positively increased again following an insulating I-V curve, but far more conductive than for the pristine device. Finally, (9) there is a sudden current increase for voltages around 15 V, achieving again the LRS. The cycle continues at point (3) and it is repeated at the following cycles. Therefore, the switching to the LRS is obtained by applying a writting voltage of $V_{SET} > 15$ V (keeping the current compliance active), and the HRS is attained after $V_{RESET} < -5$ V is applied (without current compliance)[36].

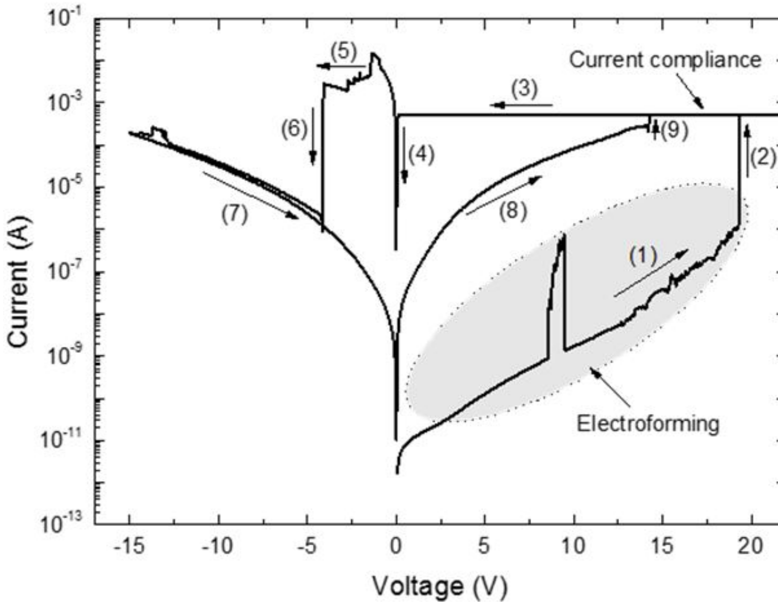

Figure 6.4 Complete cycle of a typical I-V curve, showing the different resistance states. The cycle steps are labelled by their corresponding number in the graph. Voltage bias is applied at the top electrode, whereas the back contact is grounded.

6.2.3 TEM preliminary characterization

TEM images were acquired in a cross-section configuration from a pristine device prepared by FIB using the lift-out technique. During the sample preparation no presence of defects along the electrode surface was observed (figure 6.5).

Figure 6.5 SEM image of the surface of a pristine device.

Figure 6.6 depicts the TEM images showing the Al and SiAlON layers on top of the Si substrate, presenting a good uniformity, with layer thicknesses of 70 nm and 140 nm for the Al and SiAlON layers, respectively. High resolution analysis revealed an atomically-sharp interface between the crystalline Si substrate and the amorphous SiAlON layer, with a roughness of about 3 monolayers, whereas the interface between the SiAlON and the Al electrode exhibits an enhanced roughness. Figure 6.7 shows the HRTEM images of the Si substrate/SiAlON layer and the SiAlON layer/Al electrode interfaces.

6.2.4 Structural and compositional analysis after the electroforming process

In order to shed light on the structural modifications after the electroforming, an in-depth study at the nanoscale after the

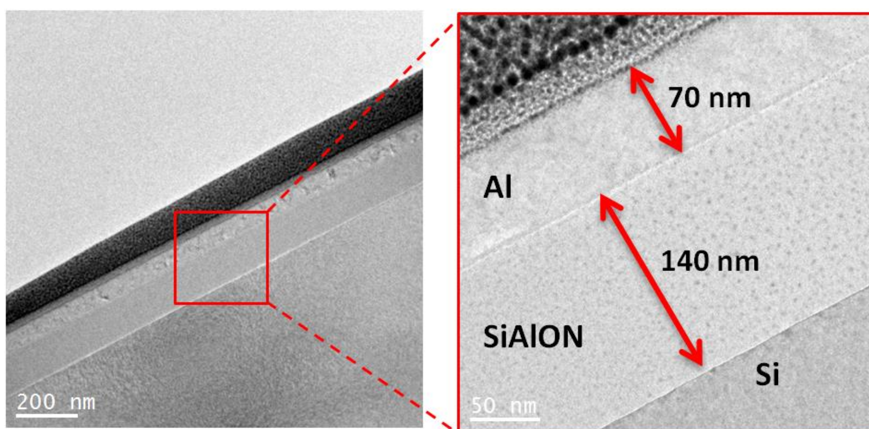

Figure 6.6 TEM image of the cross-section of a pristine device.

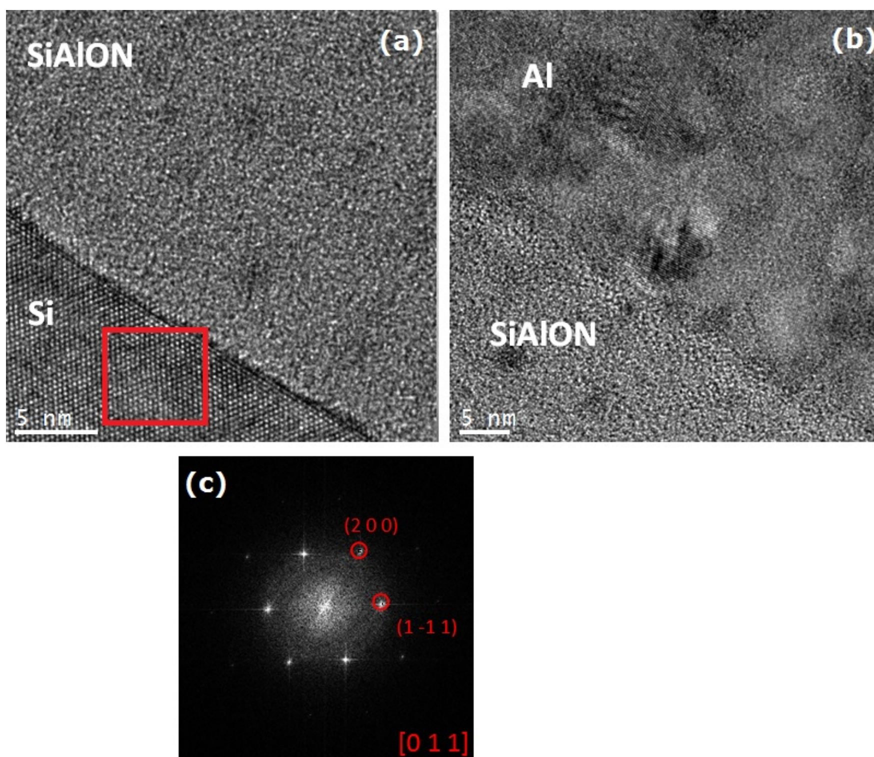

Figure 6.7 HRTEM images of (a) the Si substrate/SiAlON and (b) the SiAlON/Al electrode interfaces respectively. (c) FFT of the highlighted area.

electroforming process was addressed. Figure 6.8 shows a SEM image of the surface of a device after the electroforming process. Some irregularities can be seen on the surface, randomly distributed, with lateral sizes that range from some hundreds of nanometres to a few micrometres, which is in contrast with the smooth and homogeneous surface in pristine devices.

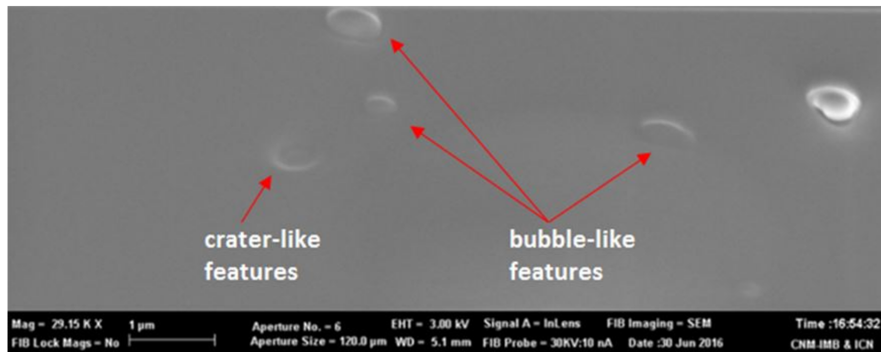

Figure 6.8 SEM image of the biased sample. Bubble-like and crater-like features are observed in the biased samples.

The formation of some of these circular shaped irregularities could even be observed during the electroforming process by optical microscopy; based on this, they were tentatively ascribed to structural modifications during the electroforming process, and therefore could be of interest to understand the resistive switching properties of the SiAlON devices.

Samples after the electroforming process were also prepared for TEM observation in a cross-section configuration by using FIB, in order to explore the structure underneath the circular bumps (see figure 6.9).

Figure 6.10 corresponds to TEM images of the lamella containing a bubble-like feature. Figure 6.10(a) clearly shows that the Al-electrode is locally bent and separated from the SiAlON layer, forming a bubble,

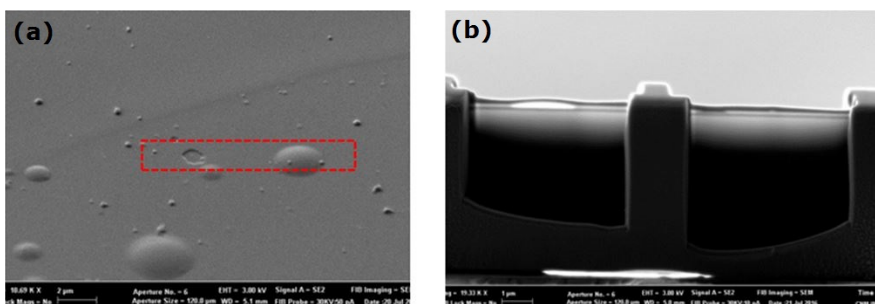

Figure 6.9 FIB images of (a) the surface of the device and (b) the TEM specimen being prepared from the highlighted region in (a).

whereas the latter is perfectly stacked on top of the substrate. In figure 6.10(c), a higher magnification image of the highlighted zone in figure 6.10(b) is displayed, where the different layers of the device are observed in the edge of the bubble, all of them continuously and perfectly stacked. However, when moving to the centre of the bubble there is an obvious detachment of the Al top electrode from the SiAlON layer, thus causing a physical deformation that can be observed from the top of the devices (the separation is around 200 nm in height). The contrast of the region between the electrode and the SiAlON layer corresponds to a void region, suggesting that this surface inhomogeneity displays a bubble-like structure, which was presumably filled by gas during the electroforming process. Figure 6.11 shows a composition of HRTEM images along the bubble-like feature.

Considering the chemical reduction of the active layer during the electroforming process reported in the literature and the atomic species of our SiAlON layer, the only gases that can possibly produce those bubbles are either O_2 or N_2. Thus, the positive bias applied to the top electrode should induce the migration of negatively-charged O or N ionic species from the SiAlON layer towards the top electrode. Whereas some authors reported O_2 release during both the electroforming process and for the formation of new conductive filaments in oxides

[37,38], devices based on nitrides have been observed to release N_2 during the resistive switching process, which would also promote the formation of gas bubbles [39].

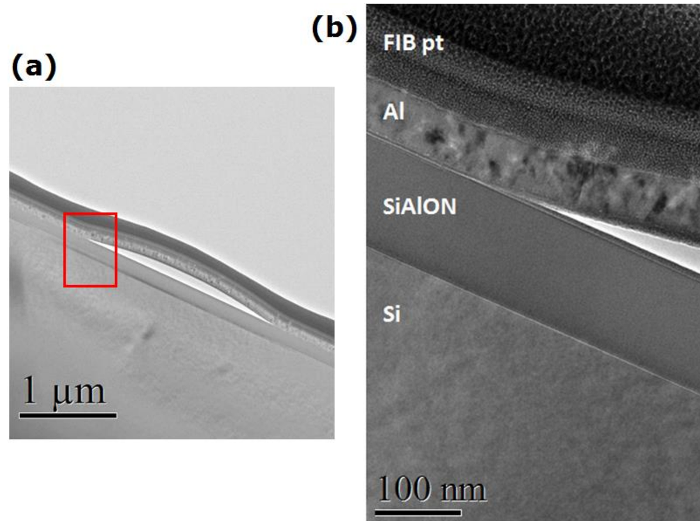

Figure 6.10 (a) Cross-section TEM image of a bubble. (b) Detailed image at the edge of the bubble, i.e., the red framed region in (a).

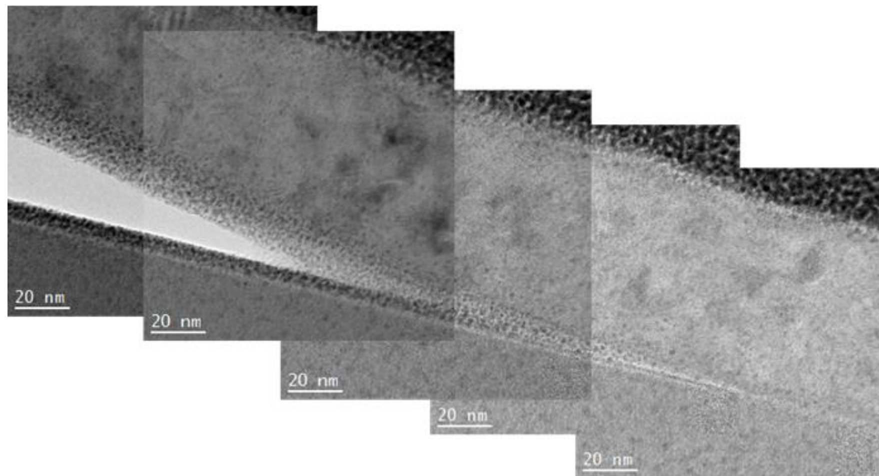

Figure 6.11 HRTEM image composition of the bubble-like feature.

Nevertheless, the creation of bubble-like features is not the only mechanism that governs the formation of topological irregularities in the surface. Figure 6.12 shows a cross-section TEM image corresponding to another feature in the surface. It is evident from the figure that in this region there is a local thickness increase of the layer beneath the Al-electrode, with a non-uniform contrast. In fact, the image reveals a precipitate on top of the SiAlON layer, which bends the Al contact (see the dotted-framed region of figure 6.12). The precipitate presents a width of 250 nm and a height of 130 nm, showing an irregular shape. Immediately under this precipitate there is a darker region within the SiAlON layer, suggesting a compositional modification of this active layer that is presumably related to the formation of the precipitate on top. It is important to note that this feature is not observed underneath the bubbles, where the SiAlON layer seems to remain unaltered.

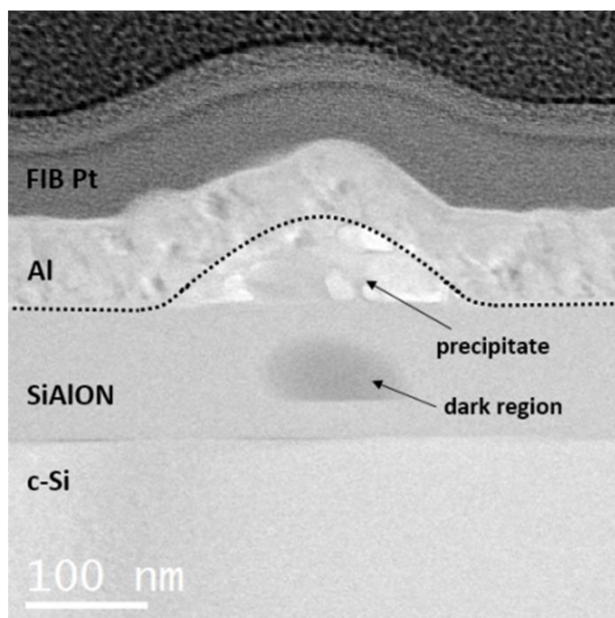

Figure 6.12 TEM image of the cross section of a different feature, showing a precipitate beneath the Al electrode and a dark region within the SiAlON layer.

In order to assess the local composition, low-loss EELS analyses of these regions were carried out in STEM mode. Figure 6.13(a) and figure 6.13(b) correspond to the STEM-HAADF images of the analysed regions (a bubble and a precipitate). Figure 6.13(c) and figure 6.13(d) show the colour-coded maps corresponding to the energy value of the bulk plasmon peak observed in the low energy loss region of the spectra in the considered areas. The colour scale ranges from 14 eV (red) to 26 eV (purple). The low-loss region of the spectra of the elements and compounds of relevance for this analysis are displayed in figure 6.13(e) (plasmon values of Si (∼16.7eV), SiO_2 (∼23eV), Si_3N_4 (∼24eV), Al (∼15 eV) and Al_2O_3 (23.8 eV) are obtained from EELS databases[40,41]).

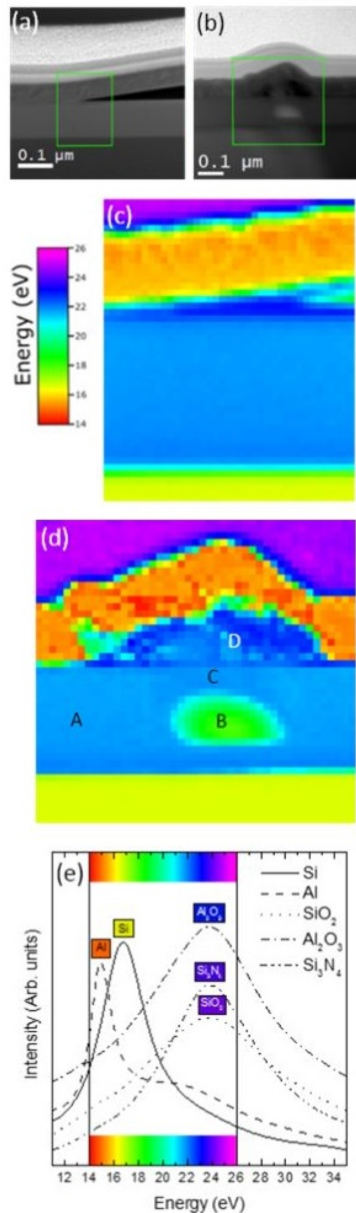

Figure 6.13 STEM HAADF images corresponding to (a) an edge of a bubble and (b) a precipitate. (c) and (d) show the colour-coded plasmon energy maps of the highlighted regions in (a) and (b), respectively. (e) Low loss spectra of Si, Al, SiO_2, Al_2O_3 and Si_3N_4, showing the plasmon of Si (∼16.7eV), SiO_2 (∼23eV), Si_3N_4 (∼24eV), Al (∼15 eV) andAl_2O_3 (23.8 eV), where the colour scale employed in (c) and (d) is also included and correlated to the chemical composition according to the plasmon energy.

In figure 6.13(c), a homogeneous contrast can be observed for all the layers, both at the edge and in the middle of the bubble, which indicates that there is no modification of the plasmon energy of the different layers (SiAlON and Al), i.e., no modifications of their stoichiometry. Moreover, there is a clear shift to higher energies of the plasmon peak at the interfaces that can be attributed to partial oxidation because of their exposure to the atmosphere during the different steps of the device fabrication. However, the interface between the SiAlON and Al layers presents higher plasmon energies than for both materials, pointing to a higher content of either O or/and N. Due to the fact that the composition is homogenous around this region and the fact that the bubble must be filled by gas (either O_2 and/or N_2), the compositional variation at the SiAlON/Al interface could be related to O or N migration from other regions of the device, forming SiO_2 and/or Si_3N_4 or Al_2O_3, which results in an effective plasmon shift to a higher energy.

The same analysis was carried out in the region where a precipitate is observed (figure 6.13(b) and figure 6.13(d)). The region labelled as A in figure 6.13(d) presents a plasmon peak at 21.8 eV, corresponding to the SiAlON layer, which energy is substantially lower than the plasmon peak for SiO_2 or Si_3N_4, but larger than the one corresponding to pure crystalline Si. The SiAlON region labelled as B in figure 6.13(d) presents a different plasmon energy, centred around 18.0 eV (green colour in the image), which evidences that this region has a different composition than the rest of the SiAlON layer. The fact that the plasmon energy of this region has decreased with respect to its surroundings indicates a larger concentration of either Si and/or Al, with some degree of oxidation or nitridation (i.e., formation of a silicon rich oxynitride). Therefore, these results suggest that there has been some out-diffusion of O (and probably N) from this region

towards other parts of the structure (for instance, towards the top electrode as suggested by figure 6.13(c)), which takes place during the electroforming process.

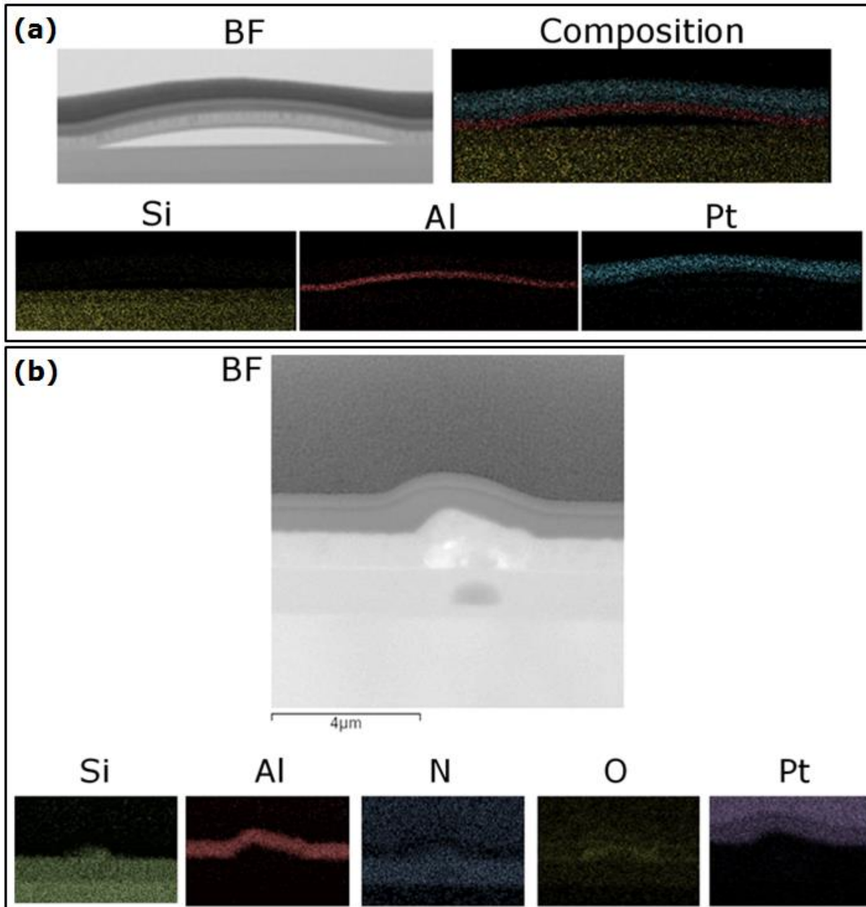

Figure 6.14 EDX map of (a) a bubble-like feature and (b) a precipitate for Si, Al, N, O and Pt and the Bright Field TEM image of the observed region.

The region just above B, labelled C, displays a plasmon peak around 22.2 eV, close but with a slightly larger energy than the one corresponding to the SiAlON layer, which can be attributed to a higher presence of O and/or N. Finally, the region labelled D in figure 6.13 (d) presents a plasmon peak around 23 eV, which indicates a region rich in

O or N between the SiAlON and Al layers. In addition, the Al contact presents a more irregular plasmon energy distribution, indicating a compositional modification probably caused by the precipitate. In addition, energy-dispersive X-ray spectroscopy measurements in the same region assessed the presence of Si, Al, O and N within the SiAlON layers (figure 6.14).

In order to determine whether the shift of the plasmon peak is due to the interdiffusion of N or O, or both, further EELS experiments were carried out. Figure 6.15 shows the composition density maps of the precipitate obtained from core-loss EEL spectrum images after removing the background signal, integrating the area under the K edge of N at 401 eV (figure 6.15(b)) and the K edge of O at 532 eV (figure 6.15(c)). The results of the core loss EELS study clearly show that the shift of the plasmon peak is due to the distribution of both oxygen and nitrogen through the SiAlON layer. In addition to their presence in the precipitate, the region just below (labelled B in figure 6.13(d)) shows a lower concentration of these two elements. The fact that the Al-electrode exhibits a more intense oxygen signal than the SiAlON layer could be ascribed to the different probability of electron-matter interaction of Al and SiAlON. The results displayed in figure 6.13(d), where the Al-electrode presents a plasmon peak closer to Al than to Al_2O_3, are in good agreement with this assumption. However, a high concentration of oxygen at the interface between the precipitate and the Al electrode is also observed, thus indicating an oxygen diffusion from the SiAlON layer into the elelectrode.

6.2.5 Discussion

Due to the fact that both oxygen and nitrogen ions are negatively charged, the composition results presented so far suggest that these

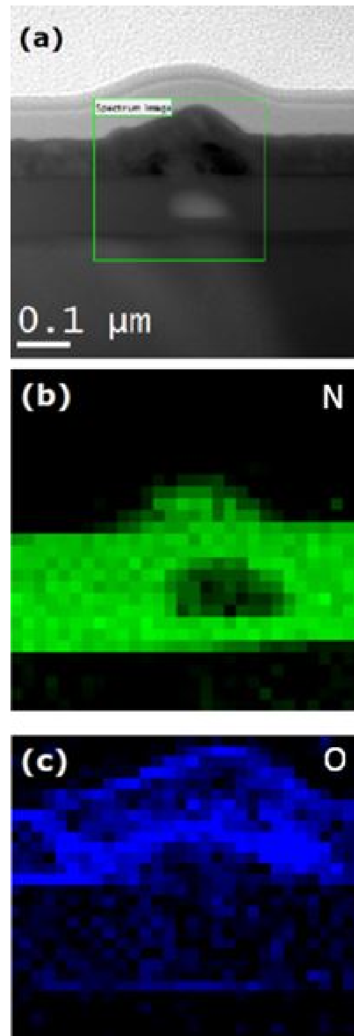

Figure 6.15 (a) STEM HAADF image corresponding to the precipitate under analysis. (b) and (c) show the composition density maps obtained from the core-loss EEL spectrum of the highlighted region. Compositional maps are obtained from the areal density of the K edge of N at 401 eV (green) and the K edge of O at 532 eV (blue).

ions drift towards the top electrode when polarized under positive bias. During the upward diffusion of O^{2-} and N^{3-} ions, a non-negligible concentration of these ions is partially trapped in the intermediate region (label C in figure 6.13(d)), as demonstrated by a subtle shift

to higher energies observed when analysing the latter. Part of the remaining (i.e., still diffusing) ions arrive to the precipitate (label D), again inducing a plasmon blueshift in this region due to enhanced SiO_2 and Si_3N_4 formation. If the diffusing O^{2-} and N^{3-} ions concentration is higher than the precipitate can absorb, these ions may actually reach the SiAlON/Al interface, where they are discharged forming O_2 and N_2 gas, which is in turn further diffused through the interface and accumulated in random areas. After a certain gas pressure is reached, the top electrode will mechanically stress the weakest part of the layer, resulting in a layer bending that gives rise to the observed bubble-like structure on top of the devices. From the analysis of both features it is then plausible to assume that the bubble-like structures can be the final step of the proto-precipitate feature, in a process that started with ion migration from the SiAlON layer and ended up stressing (and bending) the Al contact layer by O_2 and N_2 gas saturation at the Al/SiAlON interface.

In summary, the described observations of the device cross-section morphology under external polarization, as well as the chemical composition analysis of the regions under study, give evidence of the diffusion of O^{2-} and N^{3-} ions through the SiAlON layer. In fact, the observed structural modification may be responsible for the creation of conductive paths, and therefore for the generation of memristive behaviour, as corroborated by the electrical characterization. The combination of electrical and structural results therefore demonstrates that SiAlON exhibits memristive properties similar to those of metal oxides or nitrides, where the presence of oxygen and nitrogen vacancies plays a key role in the switching between the different resistance states.

6.3 Ag/HfO_2/Pt/Si inkjet-printed structure

The inkjet printed HfO_2 structure was grown and electrically characterized by the group of Dr. Albert Cirera at the Electronic and Biomedical Engineering Department of University of Barcelona.

The inkjet-printed HfO_2 based ReRAM sample consists of a bottom electrode (50nm) on top of a Si substrate, followed by a 300 nm thick HfO_2 dielectric layer and a 700 nm thick Ag top electrode. The resulting Pt/HfO_2/Ag MIM stack is sketched in Figure 6.16

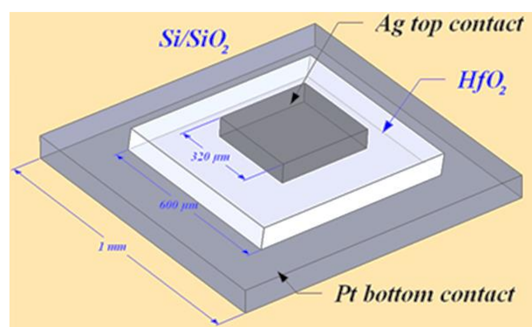

Figure 6.16 3D sketch of the HfO_2-based ReRAM device.

Inkjet printing is considered as one of the most promising techniques for non-contact and low-cost printed electronics production. It is applicable to large areas and is compatible with flexible or irregular substrates [42,46]. It represents an additive and non-contact process without the need of high temperatures, photolithography, high vacuum or etching steps which typically occur in traditional micro fabrication techniques [47], making mass-produced printable electronics possible.

The goal of this section is the study of the resistive switching mechanism in the fully inkjet-printed HfO_2 based ReRAM.

6.3.1 Sample growth

The sample fabrication was carried out by means of a Fujifilm Dimatix DMP 2831 inkjet printer, equipped with cartridges with a droplet volume of 1 pL and 10 pL, respectively, for conductive ink and 2D materials. Two types of inks were used to inkjet-print the final MIM structure: a conductive Ag-nanoparticles (NPs)-based ink and HfO_2 NPs ink as high-k dielectric (Torrecid S.L.). Contact leads were printed using Ag NPs-based ink from Advanced Nano Product (DGP-HR, 30% w/w). Further details on the HfO_2 NPs ink formulation and printing can be found elsewhere[48].

The ReRAM MIM devices were fabricated on top of oxidized Si (Si/SiO_2) substrates. First, a Pt thin film (50 nm) was deposited as bottom electrode by sputtering on a Ti layer (15 nm). Afterwards, a HfO_2 NPs-based layer (300 nm) was selectively printed over the bottom electrode covering an area of 0.1 mm^2, while keeping the substrate temperature constant at 30 °C. A post-deposition annealing process at 240 °C was then carried out for 3 h in a vacuum furnace, to ensure the elimination of the solvents. Finally, a 300-nm-thick Ag electrode was printed on top of the structure.

6.3.2 Electrical characterization

The electrical characteristics of the resulting devices were studied with a Keithley 4200 Semiconductor Parameter Analyzer. For the acquisition of transport data, the devices characterization was carried out at room temperature (∼24 °C) using a four-probe configuration.

Figure 6.17 plots two consecutive current-voltage curves (randomly selected from a set of highly-reproducible measurements) from an

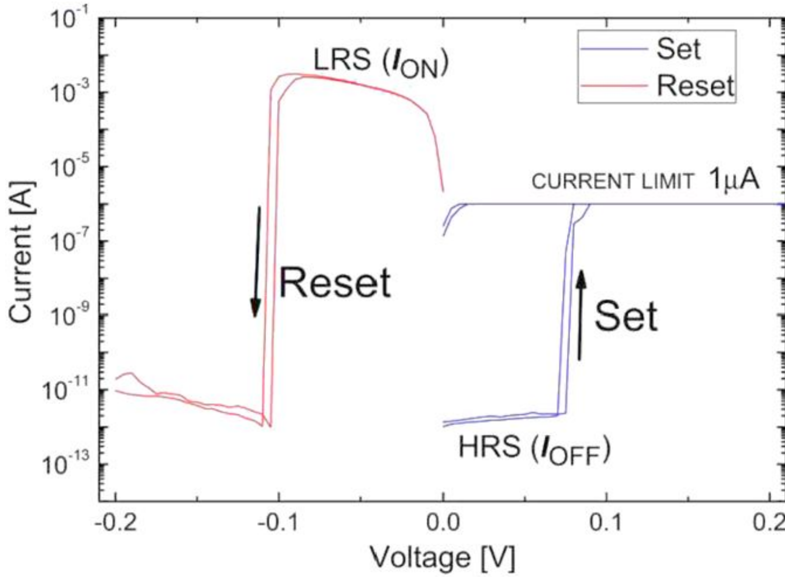

Figure 6.17 Representative bipolar switching I-V curves of two consecutive cycles measured on an inkjet-printed ReRAM device. The current compliance limit is established at 1µA to ensure avoiding the permanent breakdown of the dielectric. Blue and red lines correspond to the Set and Reset processes, respectively.

inkjet-printed memory device, after electroforming was carried out. The I-V measurements exhibit a typical bipolar resistive switching feature. On one hand, for positive voltages (Set process, blue lines in the figure) the current compliance, fixed at 1 µA, is reached at around 0.1 V. On the other hand, without any current limitation, for negative voltages (Reset process, red lines in the figure) a current of around 1 mA (I_{ON}) at -0.05 V is registered, corresponding to the LRS state (ON state). When the negative voltage ramp reaches -0.1 V, the large current immediately descends to ~5 pA (I_{OFF}), around 9 orders of magnitude lower, indicating that the sample has switched to the HRS state (OFF state).

6.3.3 Preliminary TEM characterization

In order to establish a correlation between the structural arrangement taking place within the dielectric layer and the consequent electrical switching mechanism of the inkjet-printed ReRAM devices, SEM and TEM characterization of the devices was carried out, starting by the assessment of the thickness and composition of the layers in pristine devices. Inspections by SEM of pristine samples reveal no unexpected features in the sample surface. TEM images were acquired in a cross-section configuration from a pristine device prepared by FIB using the lift-out technique (See figure 6.18).

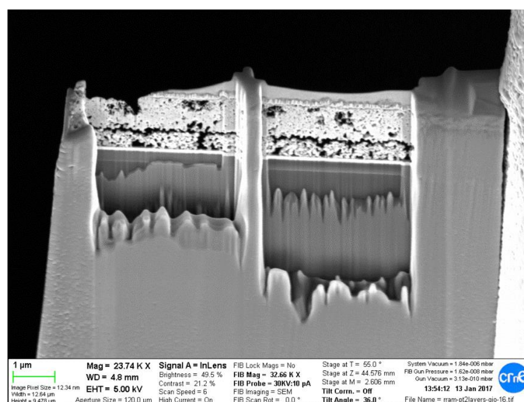

Figure 6.18 SEM image of the TEM lamella of the inkjet-printed HfO_2 based ReRAM device.

TEM images (figure 6.19 and figure 6.20) show the inkjet-printed ReRAM device on the Si/SiO_2 substrate: first a bottom electrode, with a Ti layer of 17-nm-thick and a Pt layer with a thickness of 80nm; the 300-nm-thick HfO_2 layer; and the 700-nm-thick top electrode layer of Ag. Moreover, as can be seen in the TEM images, the as-printed HfO_2 layer appears as a series of nanoparticles (NPs), sphere shaped with an average diameter of ~25 nm, forming a uniformly-deposited polycrystalline layer[49].

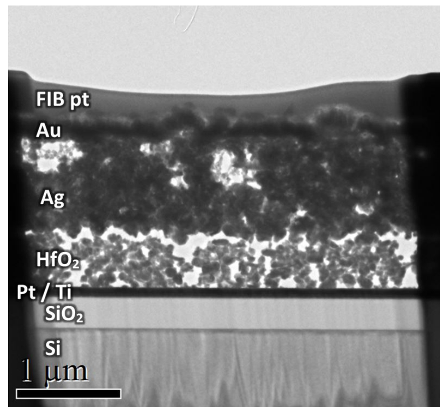

Figure 6.19 TEM image of the pristine sample showing the inkjet-printed ReRAM device with a Pt(80 nm)/Ti(17 nm) double layer bottom eletrode, the 300-nm-thick HfO_2 layer and the 700-nm-thick top electrode layer of Ag printed on the Si/SiO_2 substrate.

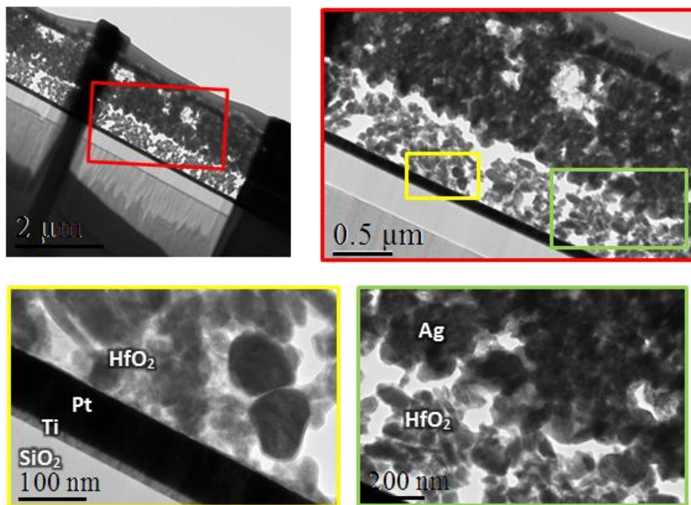

Figure 6.20 Increasingly higher magnification TEM images of the inkjet-printed device, showing the HfO_2 and Ag layers as aggregates of NPs.

6.3.4 Compositional analysis after the electroforming process

After the electroforming process and several Set-Reset switching cycles, SEM images of the memory cell were acquired (see figure 6.21). The

samples present clear randomly-distributed bubble-like features with diameters of ∼1 µm. Actually, these sort of features, typically observed in ReRAM devices (as the ones found in SiAlON based ReRAMs in the previous section), are usually attributed to oxygen diffusion during the Set-Reset cycles.

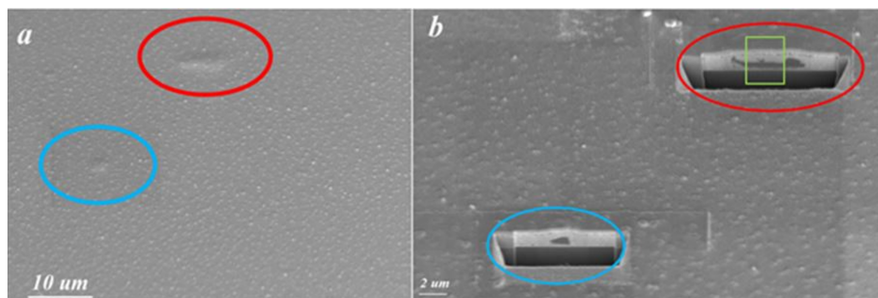

Figure 6.21 (a) SEM image of bubble-like features in a biased device; (b) FIB cross-sectional image of the detected bubbles.

In order to determine the nature of these bubble-like features, a preliminary study was performed by SEM. A TEM lamella was then prepared just where the feature was observed by FIB, using the lift-out technique (figure 6.22). SEM images reveal the presence of a feature between the Ag and HfO_2 layer which bends the surface of the device.

Figure 6.23 shows the TEM images of the sample after the electroforming, showing the presence of the clustering between the HfO_2 and Ag layers. Figure 6.24 displays the corresponding EELS study across the sample, confirming that the changes in the morphology of the devices are due to the presence of a Si agglomeration at the top Ag-HfO_2 interface. Moreover, no evidence of Ag electromigration was detected during the spectroscopy studies.

Finally, in order to perform an in-depth study of the Si cluster found at the Ag-HfO_2 interface, HRTEM images were obtained for both the Si cluster and Si substrate. As can be seen in figure 6.25,

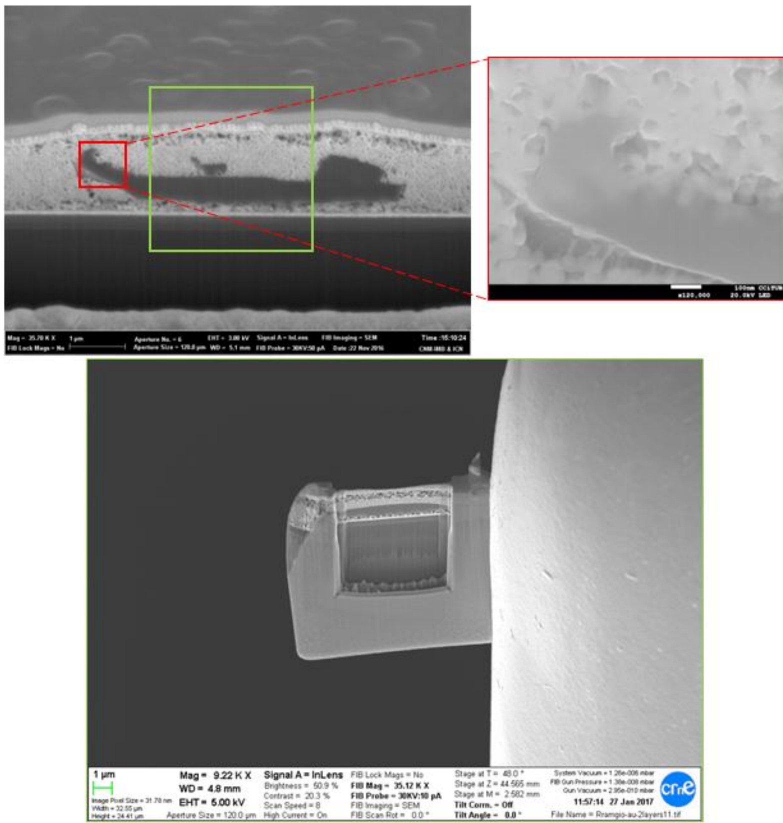

Figure 6.22 (a) FIB images of the feature found between the Ag and HfO_2 layers of the device and (b) the TEM specimen prepared in the highlighted region in (a).

the Si clustering presents a crystalline structure, identical to that of the the Si substrate (the holder had to be tilted 18° with respect to the substrate in order to recover zone axis conditions), evidencing the diffusion of the Si through the layers during the electroforming.

6.3.5 Discussion

The inkjet-printed memory cell consists of an electrochemically active electrode (Ag, top electrode), a reducible transition metal oxide layer

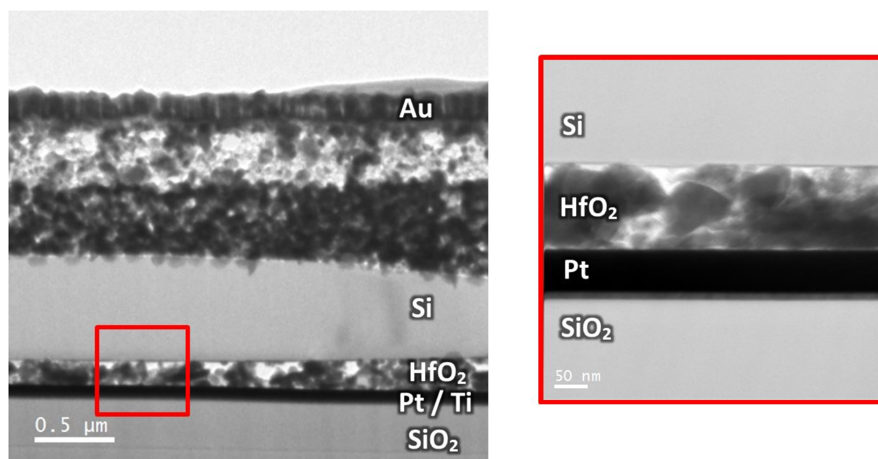

Figure 6.23 TEM images of the biased sample.

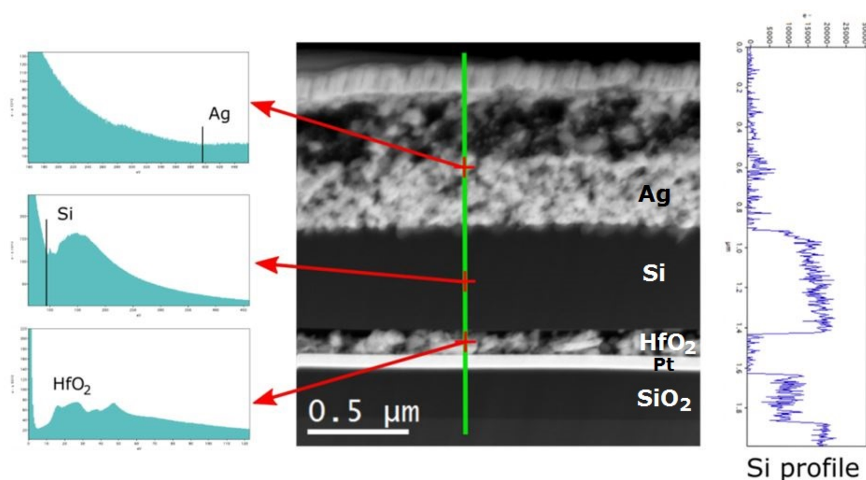

Figure 6.24 STEM image of the biased sample (center) together with the EELS data acquired along the highlighted line. Left: single spectra from the Ag layer, the Si precipitate and the HfO$_2$ layer, as indicated with red arrows. Right: Si intensity profile along the highlighted line.

(HfO$_2$) and an inert (not electrochemically active) electrode (Pt). In such a structure, the HfO$_2$ stoichiometry plays an important role. In our device, the estimated O:Hf ratio is ∼1.85 [50], thus resulting in oxygen deficiency; in turn, this leads to a high concentration of oxygen vacancies within the dielectric layer.

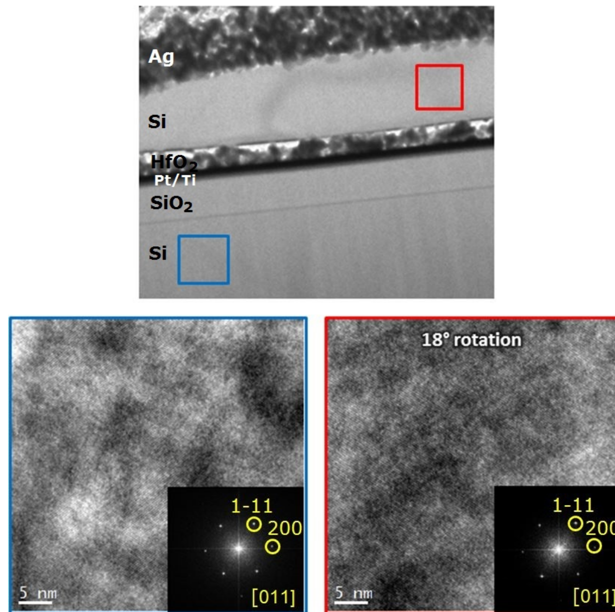

Figure 6.25 HRTEM images of the sample showing the crystallinity of the Si clustering in red and the Si substrate in blue and the corresponding FFTs (insets). The Si precipitate and the Si substrate do not present the same zone axis.

It has been recently reported that transport through highly-defective HfO_2 may take place via trap-assisted tunneling [51]. Nevertheless, although this mechanism is plausible taking into account the material characteristics, tunneling is strongly dependent on both the dielectric/metal band offsets and the applied electric field. In fact, at the low electric fields employed, other mechanisms may become more favorable. In particular, in wide-band gap materials with a high density of intrinsic defects, such as HfO_2 or ZrO_2, [52,53] charge transport usually takes place via thermally-activated charge hopping through intra-band gap allowed (defect) states, the so-called Poole-Frenkel mechanism [54]. In any case, within the frame of both proposed mechanisms for the HRS, the randomly distributed oxygen vacancies near the grain boundaries of the polycrystalline

inkjet-printed HfO_2 [55,56] are responsible for the very low currents registered in the pristine state of the memory cell.

Given the current level difference between HRS and LRS states (about 9 orders of magnitude), the transport mechanisms taking place within every state must necessarily differ, which follows from a structural modification of the film when Reset state is switched into Set. In this case, the increase in the positive voltage induces the loosely-bound oxygen ions in lattice positions (as a consequence of the breakage of the metal-oxygen bonds, Hf-O) to diffuse towards the Ag top electrode. This ionic diffusion leads to the creation of new oxygen vacancies (generated from the released O ions, causing a change of the inkjet-printed film stoichiometry) that randomly accumulate close to the inert Pt bottom electrode. When the applied voltage stress overcomes a critical threshold for the dielectric layer, the oxygen vacancies defects reach a local density that promotes the formation of a CF through the whole dielectric thickness. Therefore, a current, flowing preferentially at the grain boundaries [54], switches the memory device from pristine state to the LRS. In this state, the vertical arrangement of oxygen vacancies (i.e., the CF), can be seen as a quasi-continuum of (defect-related) electronic allowed levels. Since the high oxygen vacancies density dramatically reduces the inter-state distance, trap filling is not achieved (i.e., constant charge flow is possible), carrier transport probability through the CF thus increases, and either trap-assisted tunneling or thermal hopping no longer apply. Instead, one can see the new set of electronic states as a mini-band settled deep within the HfO_2 band gap, through which quasi-Ohmic transport takes place. [57]

The structural modification cycle ends during the Reset process, when the applied negative voltage drives back the oxygen ions from

the top electrode to the inert bottom electrode. In this case, as the maximum current flows through the CF, the diffused-back O^{2-} anions randomly fill the previously-formed VO within the CF crystalline sites. Once this stochastic total re-oxidation of the CF occurs [48], the memory device switches from LRS to HRS due to the abrupt increase in the electrode/dielectric barrier height, and, again, purely dielectric-based mechanisms govern charge transport.

Yang et al. demonstrated enhanced switching uniformity and stability in TiO_2-based ReRAM due to the diffusion of the underlying Ti through the Pt bottom electrode, which in turn reacted with the metal-oxide layer, consequently generating oxygen vacancies in the dielectric film [58]. In our case, Si diffusion is detected instead of Ti. This phenomenon probably enhances the uniformity of the RS and the stability of the ReRAM. In collaboration with the group of Dr. Cirera, it has been demonstrated that when no Si diffuses through the HfO_2 (by using an Au electrode instead of Pt), the current distributions are less uniform and in some cases the ReRAM can be damaged by the excess of O- atoms in the Ag-HfO_2 interface. The lack of diffusion of Ti is explained by the annealing temperature used to deposit the inks, which is usually around 200°C, as it is necessary to anneal the Ti/Pt electrode over 600°C to promote the Ti diffusion [57]. Moreover, the generated Si interlayer seems to be the material that acts as a series resistance to the CF generated from the oxygen vacancies type defects, promoting a controlled self-compliance current.

6.4 $Ni/HfO_2/Si$

The $Ni/HfO_2/Si$ structure was grown and electrically characterized by the group of Prof. Francesca Campabadal from Institut de Microelectrònica de Barcelona, IMB-CNM (CSIC).

This section focuses on the elucidation of the forming mechanism of CF in $Ni/HfO_2/Si$ ReRAM structures under real operation conditions of ReRAM devices. Samples were brought *ex-situ*, at device level, to the different states of the device: HRS, LRS and hard breakdown (HBD) and then were characterized at the nanoscale by HRTEM, EELS and EDX techniques. Finally, *in-situ* biasing TEM experiments were performed to study the formation of the CF in real time and to understand the physical mechanism behind the CF formation in ReRAM devices based on HfO_2.

6.4.1 Sample growth and electrical characterization

The $Ni/HfO_2/Si$ sample consists of a 20 nm-thick layer of HfO_2 and a 200 nm-thick Ni electrode grown onto an n-type (100)-Si substrate. Figure 6.26 shows a schematic cross-section of the studied $Ni/HfO_2/Si$ structures.

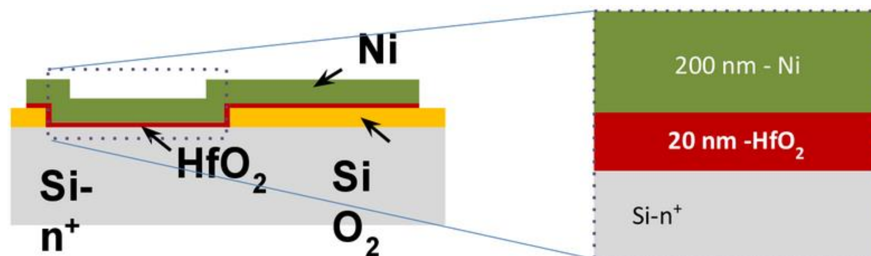

Figure 6.26 Cross-section sketch of the $Ni/HfO_2/Si$ devices under study.

The Ni/HfO_2/Si devices were fabricated on (100) n-type CZ silicon wafers with a resistivity of (0.007-0.013) $\Omega \cdot$ cm following a field isolated process. The 20 nm-thick HfO_2 layer was deposited at 225°C by atomic layer deposition (ALD) using tetrakis(dimethylamido)hafnium and H_2O as a precursors, and N_2 as a carrier and purge gas. The top metal electrode, consisting of a 200 nm-thick Ni layer, was deposited by magnetron sputtering and patterned by lift-off. The resulting MIS structures are square cells with 5×5 μm^2 and 2×2 μm^2 areas, with the contact pad on top of the field oxide.

The current-voltage (I-V) measurements were performed using a HP-4155B semiconductor parameter analyzer at 300 K. The voltage was applied to the top Ni electrode, while the Si substrate was grounded. As already reported [59], these structures show unipolar resistive switching, with the Set and Reset processes at the same voltage polarity and with the best performance for negative biases.

The forming of the CF was produced by applying a negative voltage ramp that was stopped when the current reached 100 μA. The forming occurred at voltages of around -12 V. After that, five RS cycles were performed in order to reach a stable state of the CFs (see Figure 6.27(d)). Finally, the samples were left either at the HRS or at the LRS. Figures 6.27(a) and 6.27(b) show the last I-V curves recorded for samples left at the HRS and LRS, respectively.

In addition, the hard breakdown (HBD) of the samples, which corresponds to the state where the device has a permanent damage and therefore it cannot switch anymore between the LRS and HRS state, was also analyzed. For that, the negative voltage ramp was applied with a current limit of 100 mA (the maximum current limit of conventional semiconductor parameter analyzers). In figure 6.27(c) the recorded I-V curves before and after hard breakdown are shown,

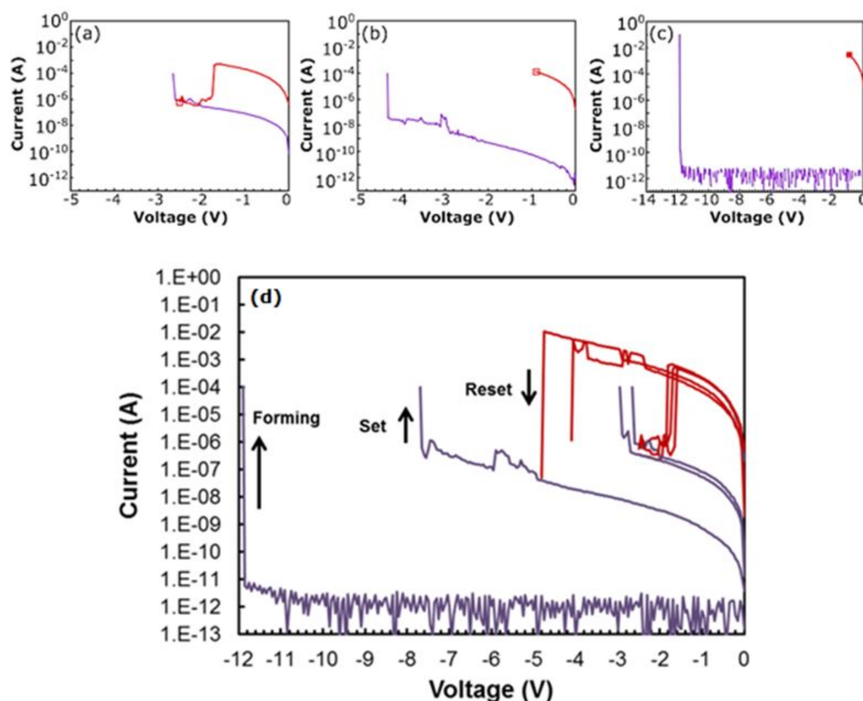

Figure 6.27 Last I-V curves after 5 RS cycles of the studied samples that were left at the (a) HRS, (b) LRS and (c) recorded I-V curves before and after hard breakdown of the studied sample in HBD state. The square symbol indicates the last measurement point. Measurements were obtained at device level with a semiconductor parameter analyzer.(d) Example of the current-voltage characteristics measured during five RS cycles performed in the sample in order to reach a stable state of the CFs.

indicating that, after hard breakdown, the conductivity is much larger than for samples at LRS.

6.4.2 Preliminary characterization

First, thickness and composition of the layers in pristine devices with the Ni electrode were assessed by TEM. TEM bright field and HRTEM images (figure 6.28) show a polycrystalline Ni electrode, 230 nm thick, an also a polycrystalline HfO_2 layer, 19 nm thick, on the monocrystalline Si substrate.

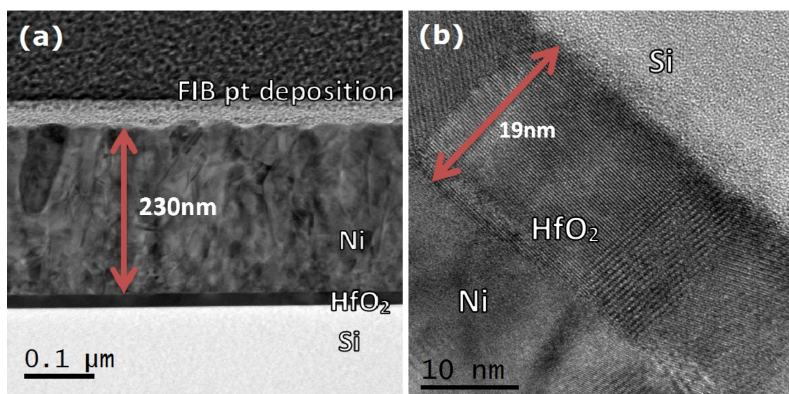

Figure 6.28 (a) TEM bright field and (b) HRTEM images of the pristine Ni/HfO_2/Si structure.

6.4.3 Assessment of the devices after the electroforming process

In order to detect the presence of a CF through the HfO_2 layer, the Ni electrode was etched off by means of a (H_2O:HNO_3) (4:1) solution. After Ni removal, surface features visible in Atomic Force Microscopy (AFM) observations revealed the location of CFs. S. Claramunt et al. observed through conductive AFM (CAFM) characterization that the CFs were formed in a unique spot with higher conductivity seen as a hillock in the topography image after the removal of the Ni electrode [60]. A schematic cross-section of the studied Ni/HfO_2/Si devices is presented in figure 6.29 showing the pristine device and also the device after the electroforming before and after the removal of the Ni electrode. TEM lamella samples were prepared precisely at the hillock site (see Figure 6.30) by Focused Ion Beam using the lift-out technique and an in-depth analysis based on HRTEM and STEM imaging combined with EELS and EDX studies was carried out.

Figure 6.31 displays the TEM images and the EELS studies carried out for each different state of the ReRAM device (HRS, LRS, and

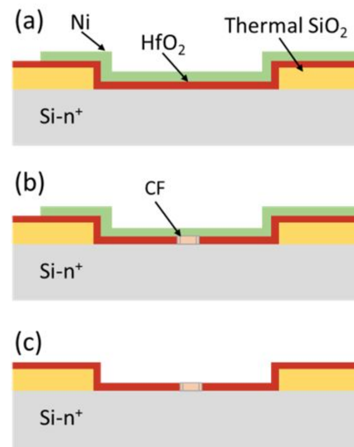

Figure 6.29 Sketch of (a) the pristine device and the device after the electroforming (b) before and (c) after the removal of the Ni electrode.

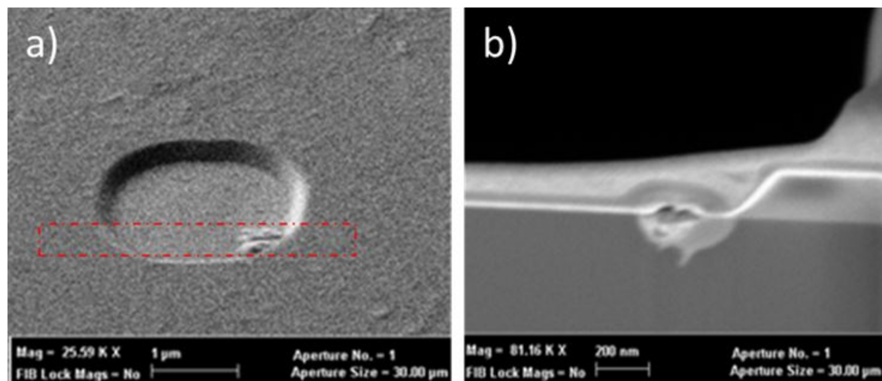

Figure 6.30 SEM images of the TEM specimen preparation process in the highlighted area of the sample. During the preparation, special attention was paid in order to ensure the hillock feature was included in the lamella.

HBD). The left column presents a general view of the CF region which is seen at higher magnification in the central column. Compositional density maps are shown in the right column of Figure 6.31, obtained from EELS spectrum images removing the background signal and integrating the area under the plasmon of HfO_2 at 15.5 eV [61] (blue), the $M_{2,3}$ edge of Ni at 68 eV (red) and the $L_{2,3}$ edge of Si at 99 eV (green).

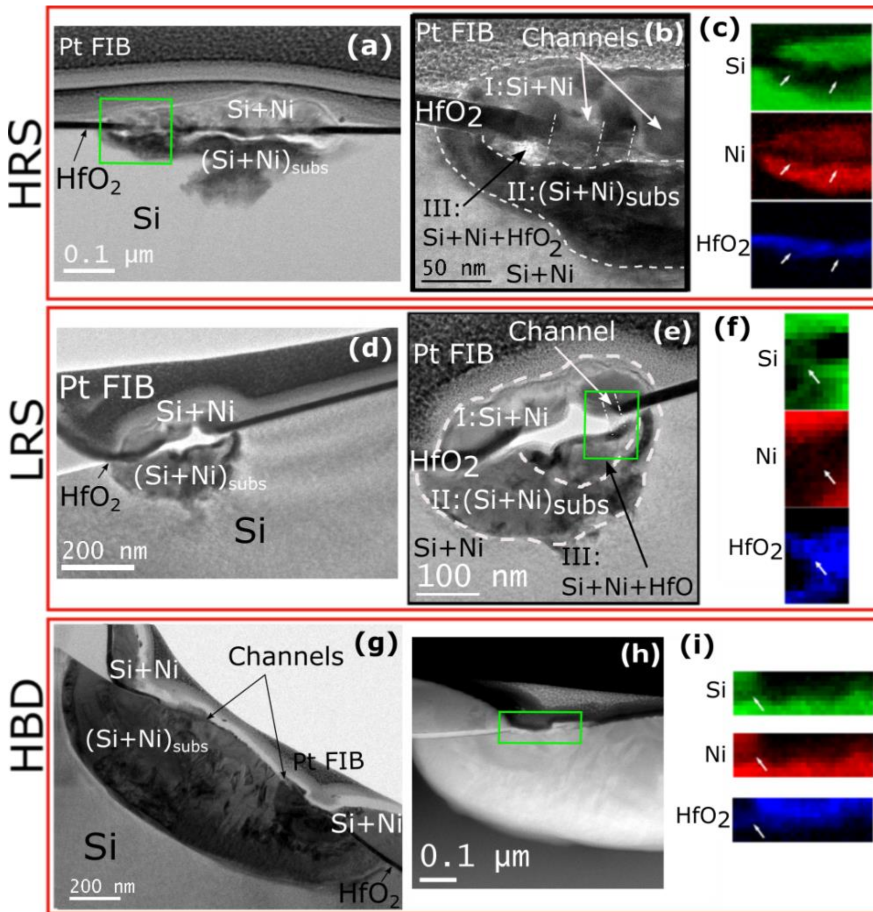

Figure 6.31 From top to bottom results for HRS, LRS and HBD showing TEM images and EELS spectrum imaging results. Green square shows the area corresponding to the spectrum image. Compositional maps are obtained from the areal density of the plasmon of HfO_2 at 15,5 eV (blue), the $M_{2,3}$ edge of Ni at 68 eV (red) and the $L_{2,3}$ edge of Si at 99 eV (green). EELS results reveal the presence of Si, Ni and HfO_2 in the conductive channels, highlighted with white arrows in the figure, and a diffusion of Ni towards the Si substrate and vice versa.

In the case of HRS (Figure 6.31 (b)), two semi-spherical structures consisting of a Ni-Si compound are observed, one in the Si substrate (region II in Figure 6.31 (b)) and the other one in the Ni electrode (region I). Also, a conductive channel [60] where the CFs are present is observed. The conductive channel and the semi-spherical structure

of the substrate present the same crystallographic orientation as the n^+ doped Si substrate but the semi-spherical Ni-Si structure of the Ni layer is found to be polycrystalline. Another semi-spherical shaped structure in the Si substrate next to the HfO_2 layer (region III) is also observed, corresponding to a Ni-Si-HfO_2 compound. Interestingly, several crystalline conductive channels of a Ni-Si-HfO_2 compound are found to lie across the HfO_2 layer. Thus, not only diffusion from the Ni towards the Si substrate exists, but also Si migration towards the Ni electrode through the HfO_2 layer is observed. Figure 6.32 shows the results of the EDX mapping for the HRS sample, in good agreement with the results obtained from EELS analyses.

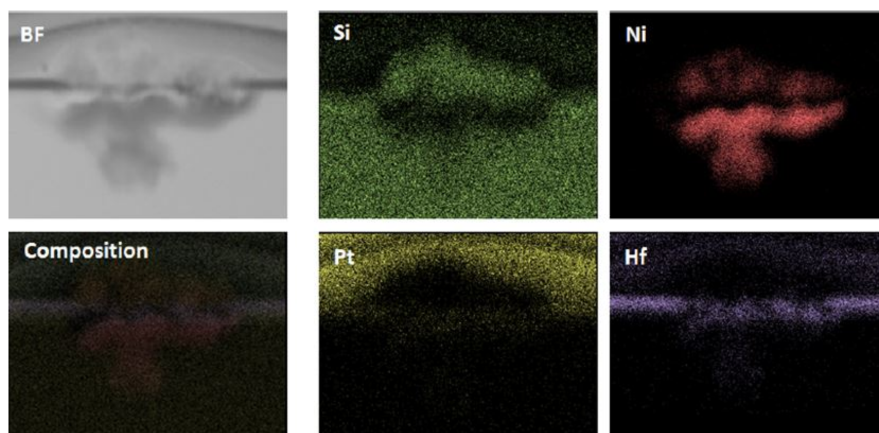

Figure 6.32 EDX map of the HRS state for Si (yellow), Ni (red), Pt (green) and O (blue), the color composition of all these elements and the bright field TEM image of the observed region.

LRS (figure 6.31 (e)) sample presents one crystalline conductive channel composed of a Ni-Si-HfO_2 compound. Besides, as in the HRS case, diffusion from the Ni electrode to the Si substrate and vice-versa is observed, forming two semi-spherical structures of a Ni-Si compound (region I in the electrode, region II in the substrate) and another one corresponding to a Ni-Si-HfO_2 compound (region III) in between. Notice that the white region at the interface between regions I and

II corresponds to a vacuum gap between the Ni electrode and the substrate. Similar regions have been observed for samples inspected in the HRS (see figure 6.31(a)) and HBD state (see figure 6.38). Figure 6.33 shows the results of the EDX mapping for the LRS sample.

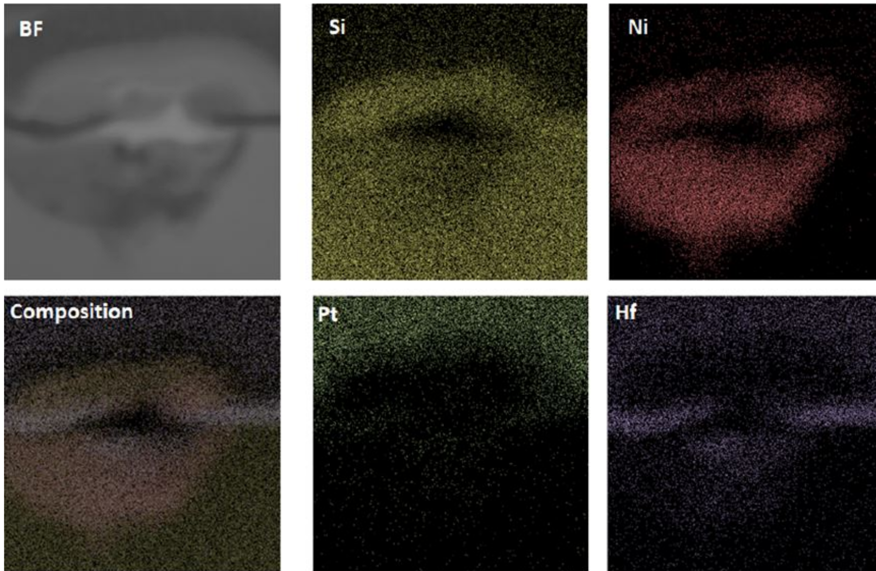

Figure 6.33 EDX map of the LRS state for Si (yellow), Ni (red), Pt (green) and O (blue), the color composition of all these elements and the bright field TEM image of the observed region.

Finally, for the HBD state (figure 6.31 (g)), several crystalline conductive channels and the two semi-spherical structures of Ni-Si compound are observed, but the Ni-Si structure in the substrate has a perfect semi-spherical shape and a diameter one order of magnitude larger than in the cases of the LRS and HRS. Figure 6.34 depicts the results of the EDX mapping showing the Ni and Si difussion, in good agreement with EELS results.

Figure 6.35 shows a composition of HRTEM images along the features produced during the electroforming for the HBD sample.

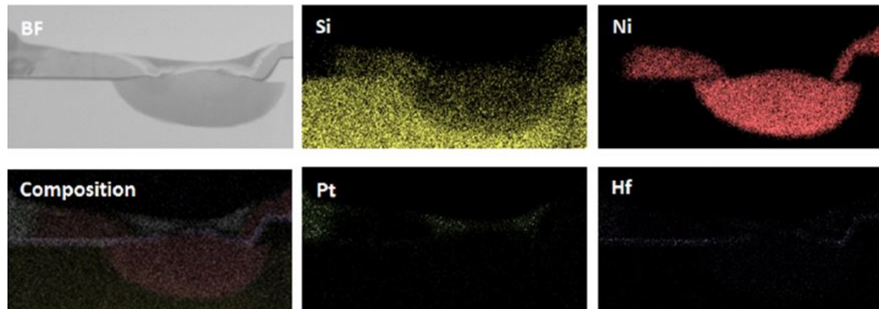

Figure 6.34 EDX map of the HBD state for Si (yellow), Ni (red), Pt (green) and O (blue), the color composition of all these elements and the bright field TEM image of the observed region.

Figure 6.36 shows an example of the boundary between the Si substrate and the Ni-Si compound structure with the corresponding FFT of the highlighted area (Ni-Si structure with the same zone axis as the n^+ doped Si substrate). For all cases of biased samples, Fast Fourier Transforms (FFT) of HRTEM images of the Si substrate and Ni-Si compound suggest the presence of a $NiSi_2$ phase, which has a cubic structure (a=0.5406 nm) very similar to the Si structure (a = 0.5431 nm). Nevertheless, multiple grain boundaries in the whole Ni-Si structure in the substrate are observed (see figure 6.37). In the literature, similar diffusion effects of Ni towards the Si substrate in CMOS devices have been observed [62,63].

In order to rule out any influence of the Ni removal process in the obtained results, a TEM lamella of a HBD sample with an intact Ni electrode was prepared by FIB, cutting the whole device slice by slice, and observing simultaneously with SEM until an evidence of the dielectric rupture became visible. Figure 6.38 displays the obtained TEM and EELS results. Again, a crystalline conductive channel of a Ni, Si and HfO_2 compound, and two structures, in the Si substrate and in the Ni layer, consisting of a Ni-Si compound are observed. Thus, diffusion from the Ni towards the Si substrate and vice versa is

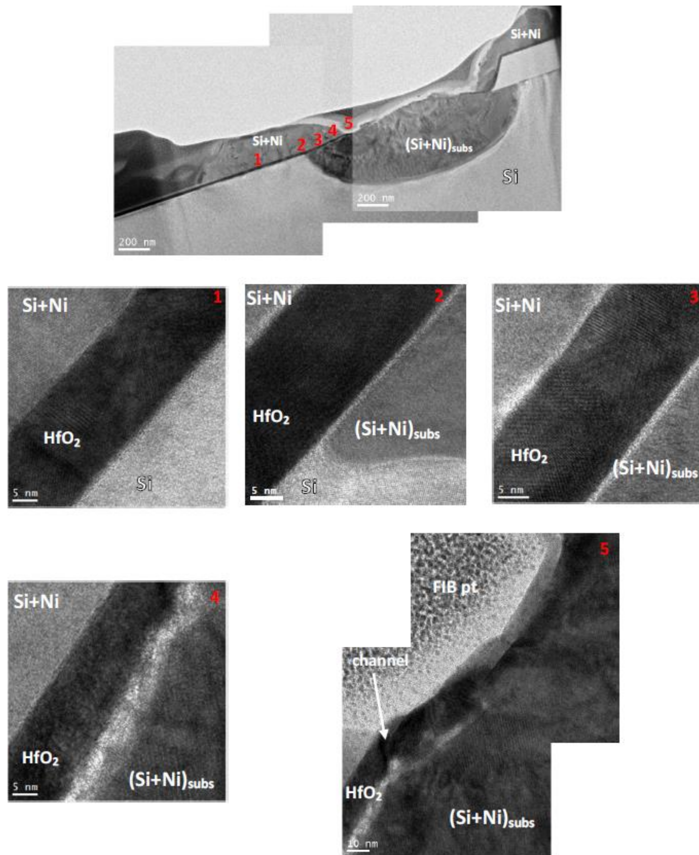

Figure 6.35 HRTEM images of the HBD state along the features produced during the electroforming.

also present. Hence, the results obtained in the sample with the Ni electrode are totally consistent with the ones with the Ni electrode previously removed.

6.4.4 *In-situ* polarization

In order to study the physical mechanism behind the CF formation in HfO_2 based ReRAM devices, *in-situ* TEM experiments were performed. A TEM lamella for the *in-situ* studies was prepared. Several cuts were

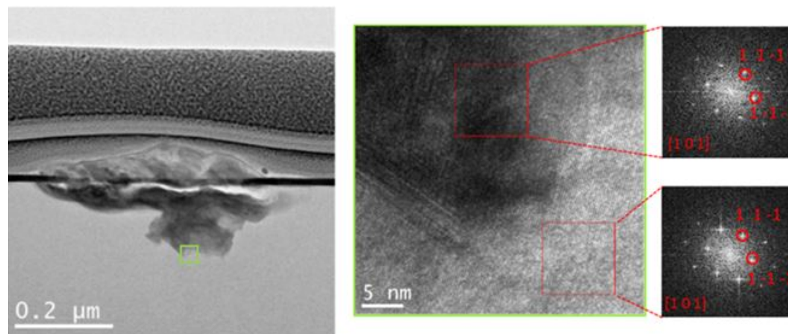

Figure 6.36 Bright Field TEM and HRTEM images of the HRS sample with the corresponding FFTs of the highlighted areas, for the Si substrate and the Ni-Si structure.

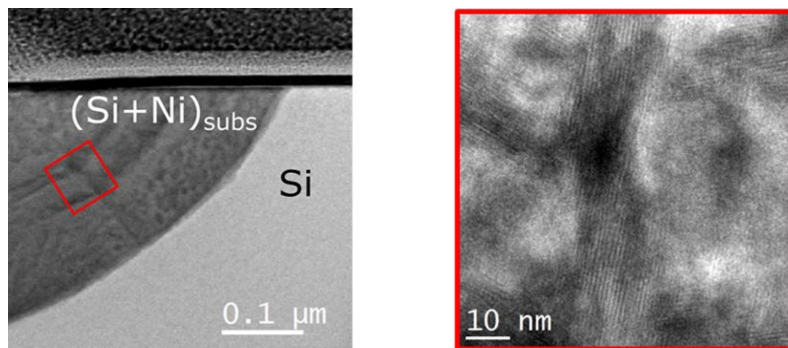

Figure 6.37 HRTEM images of the HBD state along the features produced during the electroforming.

carefully made by milling with FIB in the electrotransparent part of the lamella (as shown in figure 6.39 (b) highlited with red arrows) in order to avoid the short-circuits between the Pt FIB deposition and the TEM grid and allowing the flow of current through the ReRAM device. Notice that, as more cuts are done, more individual devices are obtained for the *in-situ* experiments. As can be seen in figure 6.39 (c), the Pt tip of the TEM-STM holder was carefully approached to the desired part of the sample in order to perform the electrical measurements.

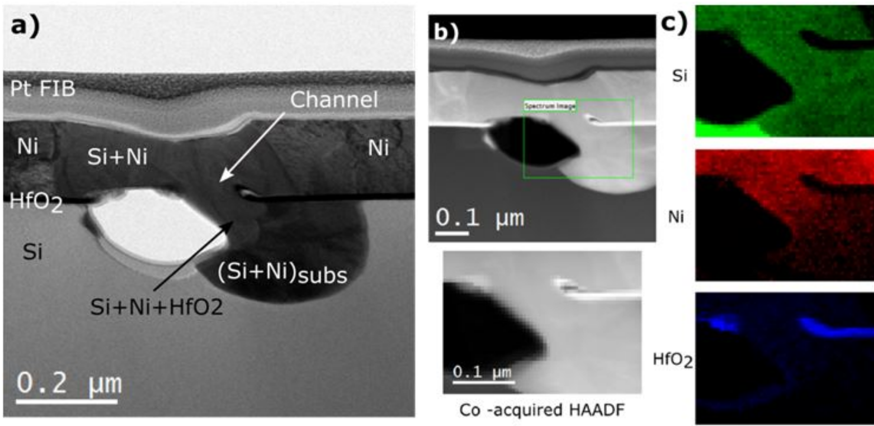

Figure 6.38 Cross-section of a sample previously to Ni removal. (a) Bright field TEM image of the sample with Ni electrode, (b) general image and HAADF co-acquired signal of the area corresponding to the spectrum image, and (c) EELS results of the sample with the Ni electrode. Compositional maps are obtained from areal density of the plasmon of HfO_2 at 15.5 eV (blue), the $M_{2,3}$ edge of Ni at 68 eV (red) and the $L_{2,3}$ edge of Si at 99 eV (green). The results obtained in the sample with the Ni electrode are totally in perfect agreement with the ones corresponding to the samples in which the Ni electrode was removed.

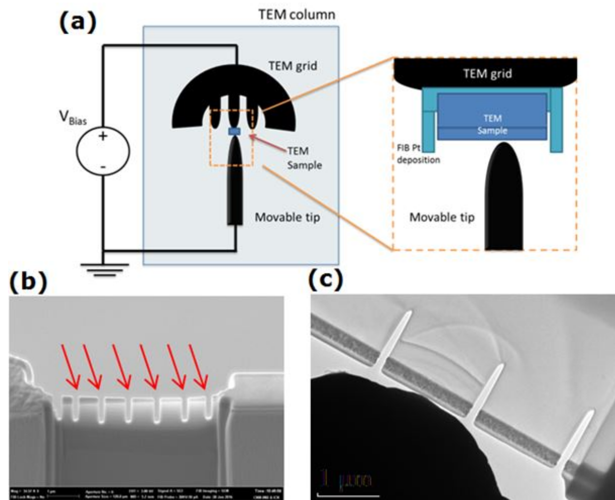

Figure 6.39 (a) Cartoon of the STM tip contacting the sample during the polarization. (b) FIB image of the cuts in the lamella (highlighted with red arrows). (c) TEM image of the STM tip contacting an individual device.

In a first step, an I-V curve was measured from 0 to 1V (values low enough to avoid structural changes in the sample) in order to evaluate the conductivity of the $Ni/HfO_2/Si$ sample. In a second step, a controlled bias of 10V was applied to the sample surface in order to induce the electroforming through the HfO_2 layer (figure 6.40 shows the current vs time measured during the experiment). Finally, in a third step, the conductivity of a $Ni/HfO_2/Si$ sample was measured again from I-V curves acquired at the same bias voltage range as in the first step. Figure 6.41 shows the I-V characteristics of the $Ni/HfO_2/Si$ sample before and after polarization, showing how the electrical resistance of the sample decreased due to the *in-situ* polarization, from 11MΩ before polarization to 5MΩ after polarization.

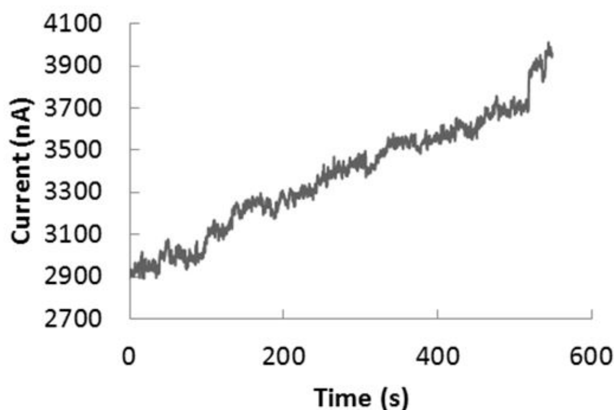

Figure 6.40 Current measured vs time applying a bias of 10V

Figure 6.42 depicts the results of the EELS study performed in the sample after the polarization. It reveals a diffusion of Ni towards the substrate through the HfO_2 layer, as expected from the studies in the *ex-situ* polarized samples.

Thus, an early CF formation is achieved in the devices inducing the electroforming inside the TEM by applying a constant bias with the TEM-STM system.

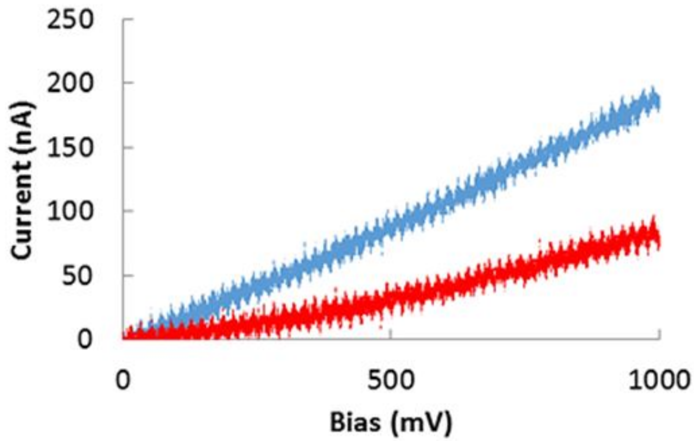

Figure 6.41 I-V characteristics of the Ni-HfO_2-Si sample before (red) and after (blue) polarization.

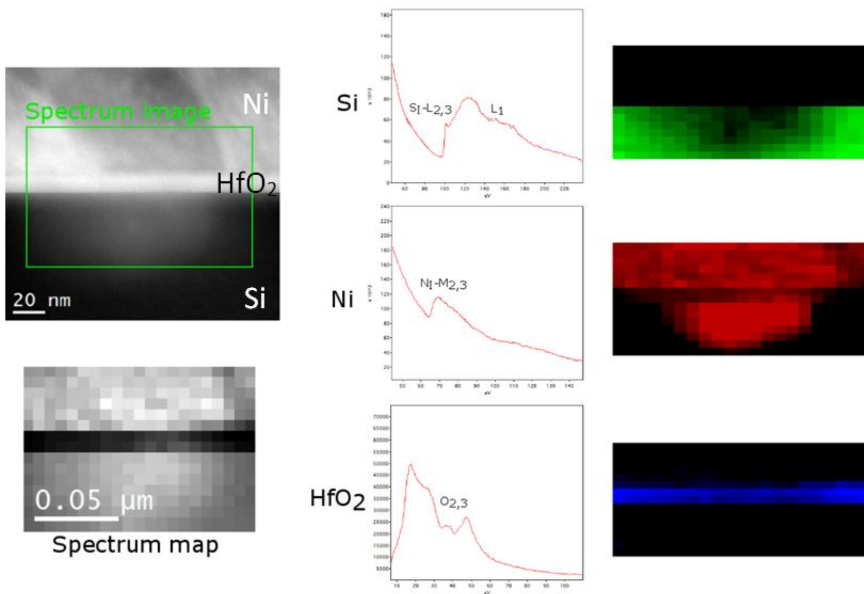

Figure 6.42 Low loss EELS spectrum imaging results. HAADF reference image shows the area corresponding to the spectrum image; bright contrast corresponds to areas with higher atomic number. Compositional maps are obtained from the areal density of the plasmon of HfO_2 at 15,5 eV (blue), the $M_{2,3}$ edge of Ni at 68 eV (red) and the $L_{2,3}$ edge of Si at 99 eV (green).

In order to achieve a complete electroforming inside the TEM, the lamella was attached directly to a wire, in order to use it as a sample support in the TEM-STM system. This way, the current that passes through the devices is increased. Nevertheless, because of the nature of the TEM-STM system, it is not possible to apply a compliance current (CC) during the experiment. For that reason, when the current is sufficient for the complete electroforming of the device, the CF are formed and consequently, the resistance of the device decreases and if, the CC is not applied, a permanent breakdown occurs. Figure 6.43 shows the measured current vs time during the experiment applying a constant bias of 10V. As can be seen in the figure, it is clear that the conductivity abruptly increases around the 2mA (because of a possible electroforming) and after that a HBD takes place. Figure 6.44 shows TEM images of a device before and after suffering the HBD using the TEM-STM system.

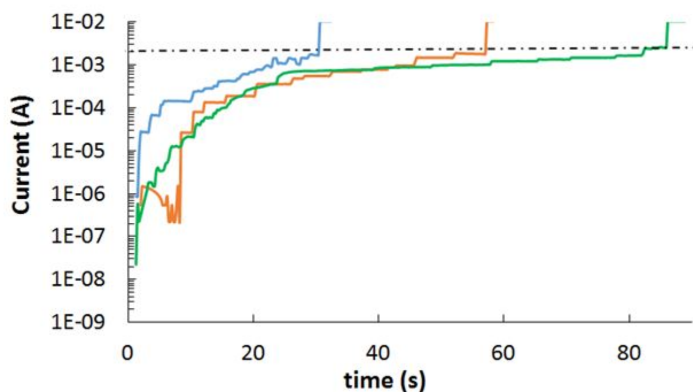

Figure 6.43 Current measured vs time applying a bias of 10V without CC for three Ni-HfO_2-Si devices.

Finally, the conductivity of a sample with a hard breakdown state polarized *ex-situ* has been recorded in order to compare the results with the conductivity of the sample polarized *in-situ* (figure 6.45). The resistance measured for this device is 40 kΩ, four orders of magnitude

lower than the one obtained with the *in-situ* early electroforming, and one order of magnitude greater than the value obtained when the electroforming is achieved (immediately after suffering a HBD) with the *in-situ* polarization.

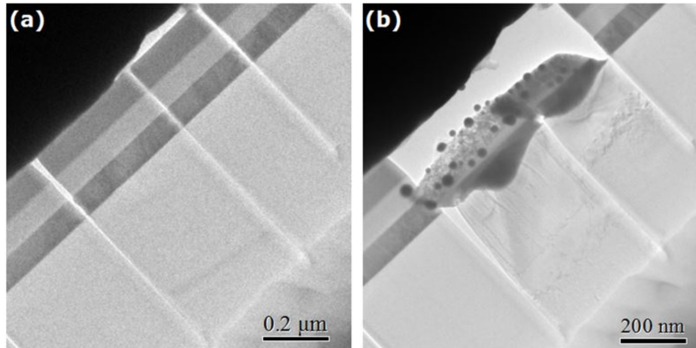

Figure 6.44 TEM images (a) before and (b) after HBD applying a bias of 10V by using the *in-situ* TEM-STM system.

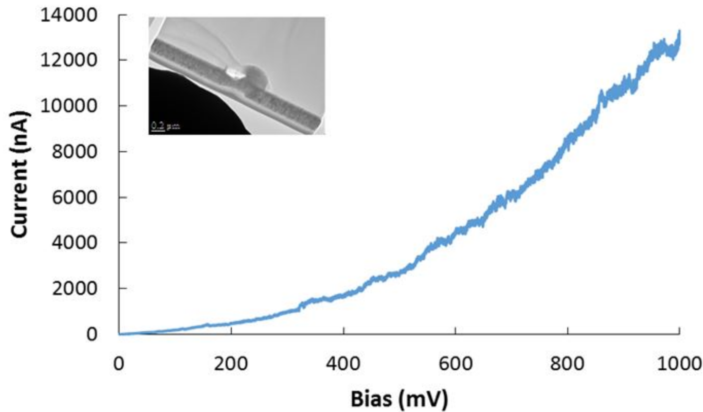

Figure 6.45 I-V characteristics of a Ni/HfO_2/Si device in a HBD state produced *ex-situ*.

6.4.5 Discussion

In summary, the presence of a CF due to interdiffusion of Si and Ni through the HfO_2 layer is clearly visible in the biased Ni/HfO_2/Si

devices. The obtained results indicate that the diffusion of Si from the substrate to the electrode and also of Ni from the electrode to the substrate through the HfO_2 layer drives the CF formation. Furthermore, the *in-situ* forming offers information on the early forming state of the CF: a Ni diffusion towards the Si substrate through the layer is observed. In view of all the experimental results, the mechanism of CF formation and evolution towards breakdown can be described as schematically shown in figure 6.46.

In the literature, similar diffusion processes of Ni into the Si substrate [62] and also the migration of the Si from the substrate to the dielectric layer [64-66] are observed in dielectric stacks. Besides, several authors [29,30] describe the migration of Ni from the electrode through the HfO_2 layer and into the Si substrate as a usual mechanism of the ReRAM behavior in HfO_2 devices. In the present work, a migration of Si to the Ni electrode is also observed, which has never been reported in ReRAM structures.

At this point, it is worth to mentioning the difficulties to elucidate the switching mechanism between LRS and HRS. Although we have observed differences between the number of conductive channels in the LRS and the HRS, we cannot directly compare them, as they are found in different devices. It must be taken into account that it is impossible to obtain a lamella of the very same device in LRS and HRS states since the preparation of a TEM thin foil is obviously a destructive procedure. Disentangling the specific differences between high and low resistance states in the same device is thus not possible. However, due to the multiple observations by TEM of the HfO_2 based ReRAM devices, we can speculate that the differences between the LRS and the HRS may be due to changes in the size and quantity of the CFs present in the device. Typically, multiple conductive channels are observed aggregated into a single conductive path.

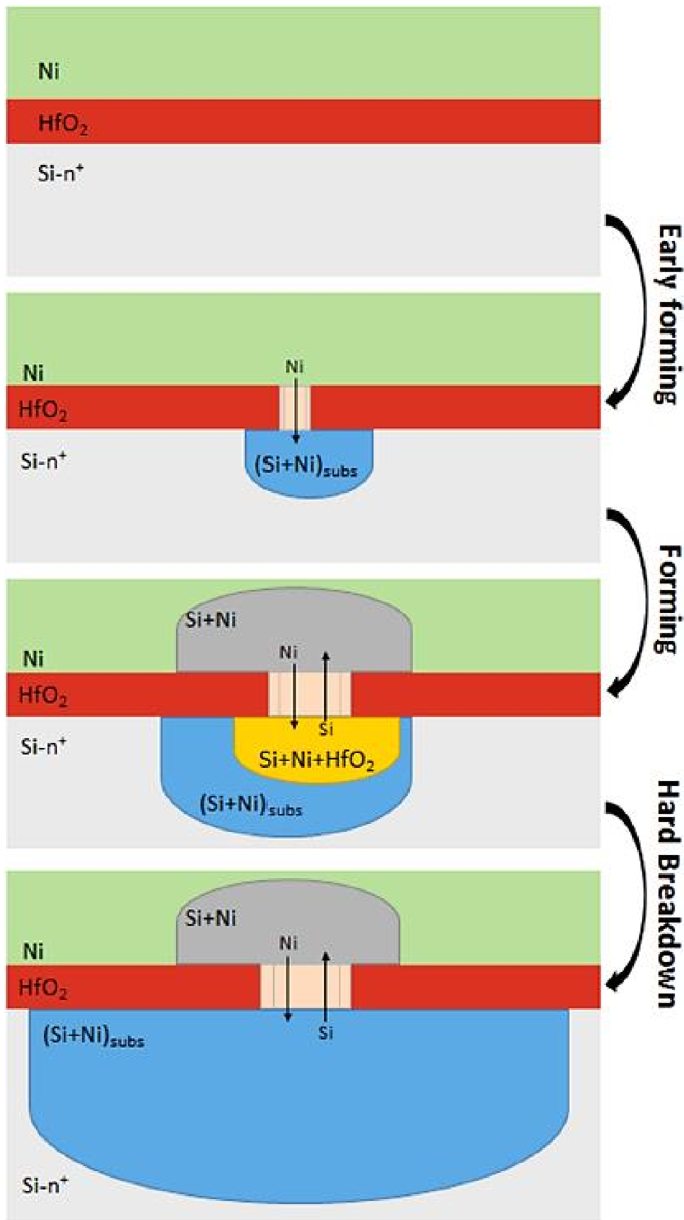

Figure 6.46 Schematic representation of the evolution of the dynamic mechanism behind the CF formation in $Ni/HfO_2/Si$ devices: pristine state (top), after forming the conductive channels (middle) and after a hard dielectric breakdown process (bottom).

Other reports about *in-situ* TEM approaches have unveiled the changes between the two states [27-30]; nevertheless, the dimensions and current values involved in this type of experiments are quite different from real operation conditions (ultra-high vacuum, geometric changes for TEM specimen preparation). Interestingly, our experimental approach for the study of the electroforming made *ex-situ* and removing the electrode in order to observe the position of the CF in the SEM, which has not been previously reported, unveils the mechanism of the CF formation in real operation conditions. Moreover the combination of the study of the CF made *ex-situ* and *in-situ* for the same devices allows us to observe the dynamics involved in the CF formation inside the TEM, and also observe the differences between the experiments inside the TEM and in real operation conditions.

In conclusion, the present work has brought to light the mechanism of CF formation in Ni/HfO_2/Si ReRAM structures. By an analysis based on HRTEM, EDX and EELS, several samples have been characterized in order to study all the different states (HRS, LRS, and HBD) of the ReRAM device. A mechanism of CF formation in ReRAM structures based on the diffusion of Ni from the electrode to the Si substrate and of Si from the substrate to the electrode through the HfO_2 layer is demonstrated. This work offers an extensive insight into the the physical and chemical nature of the CFs under real operation conditions of ReRAM devices.

6.5 Conclusions

In this chapter, the forming mechanism of CF in three different ReRAM systems has been analyzed by TEM and related analytical techniques.

In the case of SiAlON based ReRAM devices, TEM characterization evidenced the diffusion of O^{2-} and N^{3-} ions through the SiAlON layer as the mechanism responsible for the switching behaviour.

In the case of a HfO_2 based ReRAM inkjet-printed structure, EELS inspections discarded a silver electromigration effect, evidencing that the resistive switching mechanism is due to the formation of an oxygen vacancy-based conductive filament through the HfO_2 layer.

In the case of Ni/HfO_2/Si ReRAM devices, diffusion of Ni from the electrode to the Si substrate and vice versa through the HfO_2 layer has been demonstrated. Moreover, from *in-situ* TEM experiments, the diffusion of Ni and Si as the main drivers of the conducting mechanism in the studied ReRAM devices has been confirmed.

In future works, it would be interesting to focus on the *in-situ* characterization of CF formation of ReRAM devices with self-compliance.

Parts of the work presented in this chapter have been published in Applied Physics Express [67] and in Nanotechnology [36], both in 2018.

6.6 References

[1] F. Pan, S. Gao, C. Chen, C. Song, and F. Zeng, "Recent progress in resistive random access memories: Materials, switching mechanisms, and performance", Mater. Sci. Eng. R Reports, vol. 83, no. 1, pp. 1–59, 2014.

[2] R. Waser, R. Dittmann, C. Staikov, and K. Szot, "Redox-based resistive switching memories nanoionic mechanisms, prospects, and challenges", Advanced Materials, vol. 21, no. 25–26. WILEY-VCH Verlag, pp. 2632–2663, 2009.

[3] R. Waser, R. Dittmann, C. Staikov, and K. Szot, "Redox-based resistive switching memories nanoionic mechanisms, prospects, and challenges", Advanced Materials, vol. 21, no. 25–26. WILEY-VCH Verlag, pp. 2632–2663, 2009.

[4] A. Mehonic, S. Cueff, M. Wojdak, S. Hudziak, C. Labbé, R. Rizk, and A. J. Kenyon, "Electrically tailored resistance switching in silicon oxide", Nanotechnology, vol. 23, no. 45, p. 455201, 2012.

[5] T. W. Hickmott, "Low-frequency negative resistance in thin anodic oxide films", J. Appl. Phys., vol. 33, no. 9, pp. 2669–2682, 1962.

[6] W. W. Zhuang, W. Pan, B. D. Ulrich, J. J. Lee, L. Stecker, A. Burmaster, D. R. Evans, S. T. Hsu, M. Tajiri, A. Shimaoka, K. Inoue, T. Naka, N. Awaya, A. Sakiyama, Y. Wang, S. Q. Liu, N. J. Wu, and A. Ignatiev, "Novel colossal magnetoresistive thin film nonvolatile resistance random access memory (RRAM)", Dig. Int. Electron Devices Meet., pp. 193–196, 2002.

[7] E. Gale, "TiO2-based memristors and ReRAM: Materials, mechanisms and models (a review)", Semiconductor Science and Technology, vol. 29, no. 10. 2016.

[8] M. H. Tang, Z. P. Wang, J. C. Li, Z. Q. Zeng, X. L. Xu, G. Y. Wang, L. B. Zhang, Y. G. Xiao, S. B. Yang, B. Jiang, and J. He, "Bipolar and unipolar resistive switching behaviors of sol-gel-derived $SrTiO_3$ thin films with different compliance currents", Semicond. Sci. Technol., vol. 26, no. 7, p. 75019, 2011.

[9] X. Sun, G. Li, X. Zhang, L. Ding, and W. Zhang, "Coexistence of the bipolar and unipolar resistive switching behaviours in Au/$SrTiO_3$/Pt cells", J. Phys. D. Appl. Phys., vol. 44, no. 12, p. 125404, 2011.

[10] L. Goux, J. G. Lisoni, M. Jurczak, D. J. Wouters, L. Courtade, and C. Muller, "Coexistence of the bipolar and unipolar resistive-switching modes in NiO cells made by thermal oxidation of Ni layers", J. Appl. Phys., vol. 107, no. 2, p. 24512, 2010.

[11] R. Yasuhara, K. Fujiwara, K. Horiba, H. Kumigashira, M. Kotsugi, M. Oshima, and H. Takagi, "Inhomogeneous chemical states in resistance-switching devices with a planar-type Pt/CuO/Pt structure", Appl. Phys. Lett., vol. 95, no. 1, p. 12110, 2009.

[12] W.-Y. Chang, Y.-C. Lai, T.-B. Wu, S.-F. Wang, F. Chen, and M.-J. Tsai, "Unipolar resistive switching characteristics of ZnO thin films for nonvolatile memory applications", Appl. Phys. Lett., vol. 92, no. 2, p. 22110, 2008.

[13] S. Zhang, S. Long, W. Guan, Q. Liu, Q. Wang, and M. Liu, "Resistive switching characteristics of MnO_x-based ReRAM", J. Phys. D. Appl. Phys., vol. 42, no. 5, p. 55112, 2009.

[14] C. H. Lien, Y. S. Chen, H. Y. Lee, P. S. Chen, F. T. Chen, and M. J. Tsai, "The highly scalable and reliable hafnium oxide ReRAM and its future challenges", in ICSICT-2010 - 2010 10th IEEE International Conference on Solid-State and Integrated Circuit Technology, Proceedings, pp. 1084–1087, 2010.

[15] F. Miao, J. P. Strachan, J. J. Yang, M. X. Zhang, I. Goldfarb, A. C. Torrezan, P. Eschbach, R. D. Kelley, G. Medeiros-Ribeiro, and R. S. Williams, "Anatomy of a nanoscale conduction channel reveals the mechanism of a high-performance memristor", Adv. Mater., vol. 23, no. 47, pp. 5633–5640, 2011.

[16] A. S. Oblea, A. Timilsina, D. Moore, and K. A. Campbell, "Silver chalcogenide based memristor devices", in Proceedings of the International Joint Conference on Neural Networks, pp. 1–3, 2010.

[17] F. Pincella, P. Camorani, and V. Erokhin, “Electrical properties of an organic memristive system”, Appl. Phys. A, vol. 104, no. 4, pp. 1039–1046, 2011.

[18] T. Hasegawa, A. Nayak, T. Ohno, K. Terabe, T. Tsuruoka, J. K. Gimzewski, and M. Aono, “Memristive operations demonstrated by gap-type atomic switches”, Appl. Phys. A Mater. Sci. Process., vol. 102, no. 4, pp. 811–815, 2011.

[19] Y. V. Pershin and M. Di Ventra, “Spin memristive systems: Spin memory effects in semiconductor spintronics”, Phys. Rev. B - Condens. Matter Mater. Phys., vol. 78, no. 11, p. 113309, 2008.

[20] Y. V. Pershin and M. Di Ventra, “Neuromorphic, digital, and quantum computation with memory circuit elements”, in Proceedings of the IEEE, vol. 100, no. 6, pp. 2071–2080, 2012.

[21] S. Grimnes, C. A. Lütken, and O. G. Martinsen, “Memristive properties of electro-osmosis in human sweat ducts”, in IFMBE Proceedings, vol. 25, no. 7, pp. 696–698, 2009.

[22] A. G. Volkov, C. Tucket, J. Reedus, M. I. Volkova, V. S. Markin, and L. Chua, “Memristors in plants”, Plant Signal. Behav., vol. 9, no. FEB, p. 28152, 2014.

[23] S. P. Kosta, Y. P. Kosta, M. Bhatele, Y. M. Dubey, A. Gaur, S. Kosta, J. Gupta, A. Patel, and B. Patel, “Human blood liquid memristor”, Int. J. Med. Eng. Inform., vol. 3, no. 1, p. 16, 2011.

[24] E. Gale, A. Adamatzky, and B. de Lacy Costello, “Slime Mould Memristors”, Bionanoscience, vol. 5, no. 1, pp. 1–8, Mar. 2014.

[25] C. Zamarreño-Ramos, L. A. Camuñas-Mesa, J. A. Perez-Carrasco, T. Masquelier, T. Serrano-Gotarredona, and B. Linares-Barranco, “On spike-timing-dependent-plasticity, memristive devices, and building a self-learning visual cortex”, Front. Neurosci., vol. 5, no. MAR, p. 26, 2011.

[26] L. CHUA, V. SBITNEV, and H. KIM, “Hodgkin-Huxley Axon is made of memristors”, Int. J. Bifurc. Chaos, vol. 22, no. 3, p. 1230011, 2012.

[27] D.-H. Kwon, K. M. Kim, J. H. Jang, J. M. Jeon, M. H. Lee, G. H. Kim, X.-S. Li, G.-S. Park, B. Lee, S. Han, M. Kim, and C. S. Hwang, "Atomic structure of conducting nanofilaments in TiO_2 resistive switching memory", Nat. Nanotechnol., vol. 5, no. 2, pp. 148–153, 2010.

[28] Q. Liu, J. Sun, H. Lv, S. Long, K. Yin, N. Wan, Y. Li, L. Sun, and M. Liu, "Real-Time Observation on Dynamic Growth/Dissolution of Conductive Filaments in Oxide-Electrolyte-Based ReRAM", Adv. Mater., vol. 24, no. 14, pp. 1844–1849, 2012.

[29] X. Wu, S. Mei, M. Bosman, N. Raghavan, X. Zhang, D. Cha, K. Li, and K. L. Pey, "Evolution of Filament Formation in Ni/HfO_2/SiO_x/Si-Based RRAM Devices", Adv. Electron. Mater., vol. 1, no. 11, p. 1500130, 2015.

[30] X. Wu, D. Cha, M. Bosman, N. Raghavan, D. B. Migas, V. E. Borisenko, X.-X. Zhang, K. Li, and K.-L. Pey, "Intrinsic nanofilamentation in resistive switching", J. Appl. Phys., vol. 113, no. 11, p. 114503, 2013.

[31] W. A. Hubbard, A. Kerelsky, G. Jasmin, E. R. White, J. Lodico, M. Mecklenburg, and B. C. Regan, "Nanofilament Formation and Regeneration During Cu/Al_2O_3 Resistive Memory Switching", Nano Lett., vol. 15, no. 6, pp. 3983–3987, Jun. 2015.

[32] M. Kudo, M. Arita, Y. Ohno, and Y. Takahashi, "Filament formation and erasure in molybdenum oxide during resistive switching cycles", Appl. Phys. Lett., vol. 105, no. 17, p. 173504, 2014.

[33] M. Kudo, M. Arita, Y. Ohno, T. Fujii, K. Hamada, and Y. Takahashi, "Preparation of resistance random access memory samples for in situ transmission electron microscopy experiments", Thin Solid Films, vol. 533, pp. 48–53, 2013.

[34] S. J. Choi, G. S. Park, K. H. Kim, S. Cho, W. Y. Yang, X. S. Li, J. H. Moon, K. J. Lee, and K. Kim, "In situ observation of voltage-induced multilevel resistive switching in solid electrolyte memory", Adv. Mater., vol. 23, no. 29, pp. 3272–3277, 2011.

[35] I. Camps, J. M. Ramírez, A. Mariscal, R. Serna, B. Garrido, M. Perálvarez, J. Carreras, N. P. Barradas, L. C. Alves, and E. Alves, "Optical performance

of thin films produced by the pulsed laser deposition of SiAlON and Er targets", in Applied Surface Science, 2015, vol. 336, pp. 274–277.

[36] O. Blázquez, G. Martín, I. Camps, A. Mariscal, J. López-Vidrier, J. M. Ramirez, S. Hernández, S. Estradé, F. Peiró, R. Serna, and B. Garrido, "Memristive behaviour of Si-Al oxynitride thin films: The role of oxygen and nitrogen vacancies in the electroforming process", Nanotechnology, vol. 29, no. 23, p. 235702, 2018.

[37] A. Mehonic, M. Buckwell, L. Montesi, L. Garnett, S. Hudziak, S. Fearn, R. Chater, D. McPhail, and A. J. Kenyon, "Structural changes and conductance thresholds in metal-free intrinsic SiO_x resistive random access memory", J. Appl. Phys., vol. 117, no. 12, p. 124505, 2015.

[38] C. Chen, S. Gao, F. Zeng, G. S. Tang, S. Z. Li, C. Song, H. D. Fu, and F. Pan, "Migration of interfacial oxygen ions modulated resistive switching in oxide-based memory devices", J. Appl. Phys., vol. 114, no. 1, 2013.

[39] B. J. Choi, A. C. Torrezan, J. P. Strachan, P. G. Kotula, A. J. Lohn, M. J. Marinella, Z. Li, R. S. Williams, and J. J. Yang, "High-Speed and Low-Energy Nitride Memristors", Adv. Funct. Mater., vol. 26, no. 29, pp. 5290–5296, 2016.

[40] L. Reimer, U. Zepke, J. Moesch, S. Schulze-Hillert, M. Ross-Messemer, W. Probst, and E. Weimer, "EELS Atlas", 1992.

[41] Cemes, "The EELS Data Base." [Online]. Available: http://pc-web.cemes.fr/eelsdb/index.php?page=home.php.

[42] H. W. Choi, T. Zhou, M. Singh, and G. E. Jabbour, "Recent developments and directions in printed nanomaterials", Nanoscale, vol. 7, no. 8, pp. 3338–3355, 2015.

[43] V. Correia, C. Caparros, C. Casellas, L. Francesch, J. G. Rocha, and S. Lanceros-Mendez, "Development of inkjet printed strain sensors", Smart Mater. Struct., vol. 22, no. 10, p. 105028, 2013.

[44] Z. P. Yin, Y. A. Huang, N. B. Bu, X. M. Wang, and Y. L. Xiong, "Inkjet printing for flexible electronics: Materials, processes and equipments",

Chinese Science Bulletin, vol. 55, no. 30. SP Science China Press, pp. 3383–3407, 2010.

[45] M. Mäntysalo, P. Mansikkamäki, J. Miettinen, K. Kaija, S. Pienimaa, R. Rönkkä, K. Hashizume, A. Kamigori, Y. Matsuba, K. Oyama, N. Terada, H. Saito, M. Kuchiki, and M. Tsubouchi, "Evaluation of inkjet technology for electronic packaging and system integration", in Proceedings - Electronic Components and Technology Conference, pp. 89–94, 2007.

[46] V. Correia, K. Y. Mitra, H. Castro, J. G. Rocha, E. Sowade, R. R. Baumann, and S. Lanceros-Mendez, "Design and fabrication of multilayer inkjet-printed passive components for printed electronics circuit development", J. Manuf. Process., vol. 31, pp. 364–371, 2018.

[47] P. Alpuim, V. Correia, E. S. Marins, J. G. Rocha, I. G. Trindade, and S. Lanceros-Mendez, "Piezoresistive silicon thin film sensor array for biomedical applications", in Thin Solid Films, vol. 519, no. 14, pp. 4574–4577, 2011.

[48] G. Vescio, A. Crespo-Yepes, D. Alonso, S. Claramunt, M. Porti, R. Rodriguez, A. Cornet, A. Cirera, M. Nafria, and X. Aymerich, "Inkjet Printed HfO_2 -Based ReRAMs: First Demonstration and Performance Characterization", IEEE Electron Device Lett., vol. 38, no. 4, pp. 457–460, Apr. 2017.

[49] G. Vescio, J. López-Vidrier, R. Leghrib, A. Cornet, and A. Cirera, "Flexible inkjet printed high-k HfO_2 -based MIM capacitors", J. Mater. Chem. C, vol. 4, no. 9, pp. 1804–1812, 2016.

[50] G. Vescio, J. López-Vidrier, R. Leghrib, A. Cornet, and A. Cirera, "Flexible inkjet printed high-k HfO_2 -based MIM capacitors", J. Mater. Chem. C, vol. 4, no. 9, pp. 1804–1812, 2016.

[51] F. M. Puglisi, L. Larcher, A. Padovani, and P. Pavan, "Bipolar Resistive RAM Based on HfO2: Physics, Compact Modeling, and Variability Control", IEEE J. Emerg. Sel. Top. Circuits Syst., vol. 6, no. 2, pp. 171–184, 2016.

[52] A. Salaün, H. Grampeix, J. Buckley, C. Mannequin, C. Vallée, P. Gonon, S. Jeannot, C. Gaumer, M. Gros-Jean, and V. Jousseaume, "Investigation of HfO_2 and ZrO_2 for Resistive Random Access Memory applications", Thin Solid Films, vol. 525, pp. 20–27, 2012.

[53] Y. Li, S. Long, M. Zhang, Q. Liu, L. Shao, S. Zhang, Y. Wang, Q. Zuo, S. Liu, and M. Liu, "Resistive switching properties of Au/ZrO_2/Ag structure for low-voltage nonvolatile memory applications", IEEE Electron Device Lett., vol. 31, no. 2, pp. 117–119, 2010.

[54] Y. M. Kim and J. S. Lee, "Reproducible resistance switching characteristics of hafnium oxide-based nonvolatile memory devices", J. Appl. Phys., vol. 104, no. 11, p. 114115, 2008.

[55] G. Bersuker, D. C. Gilmer, D. Veksler, P. Kirsch, L. Vandelli, A. Padovani, L. Larcher, K. McKenna, A. Shluger, V. Iglesias, M. Porti, and M. Nafría, "Metal oxide resistive memory switching mechanism based on conductive filament properties", J. Appl. Phys., vol. 110, no. 12, p. 124518, 2011.

[56] J. Y. Chen, C. W. Huang, C. H. Chiu, Y. T. Huang, and W. W. Wu, "Switching Kinetic of VCM-Based Memristor: Evolution and Positioning of Nanofilament", Adv. Mater., vol. 27, no. 34, pp. 5028–5033, 2015.

[57] Y. Shuai, X. Ou, W. Luo, A. Mücklich, D. Bürger, S. Zhou, C. Wu, Y. Chen, W. Zhang, M. Helm, T. Mikolajick, O. G. Schmidt, and H. Schmidt, "Key concepts behind forming-free resistive switching incorporated with rectifying transport properties", Sci. Rep., vol. 3, no. 1, p. 2208, 2013.

[58] J. J. Yang, M. D. Pickett, X. Li, D. A. A. Ohlberg, D. R. Stewart, and R. S. Williams, "Memristive switching mechanism for metal/oxide/metal nanodevices", Nat. Nanotechnol., vol. 3, no. 7, pp. 429–433, 2008.

[59] C. Vaca, M. B. Gonzalez, H. Castan, H. Garcia, S. Duenas, F. Campabadal, E. Miranda, and L. A. Bailon, "Study From Cryogenic to High Temperatures of the High- and Low-Resistance-State Currents of ReRAM Ni–HfO_2–Si Capacitors", IEEE Trans. Electron Devices, vol. 63, no. 5, pp. 1877–1883, 2016.

[60] S. Claramunt, Q. Wu, M. Maestro, M. Porti, M. B. Gonzalez, J. Martin-Martinez, F. Campabadal, and M. Nafría, "Non-homogeneous conduction of conductive filaments in Ni/HfO_2/Si resistive switching structures observed with CAFM", Microelectron. Eng., vol. 147, pp. 335–338, 2015.

[61] M. P. Agustin, L. R. C. Fonseca, J. C. Hooker, and S. Stemmer, “Scanning transmission electron microscopy of gate stacks with HfO_2 dielectrics and TiN electrodes”, Appl. Phys. Lett., vol. 87, no. 12, pp. 1–3, 2005.

[62] K.-S. Ko, S. Crank, P. Chen, D. Yue, S. Lavangkul, H. Mogul, S. Siddiqui, and T. Bonifield, “Characterization of Defect Formation during Ni Silicidation for CMOS Device Application”, Microsc. Microanal., vol. 11, no. S02, pp. 2096–2097, 2005.

[63] X. Wu, K.-L. Pey, N. Raghavan, W.-H. Liu, X. Li, P. Bai, G. Zhang, and M. Bosman, “Using post-breakdown conduction study in a MIS structure to better understand the resistive switching mechanism in an MIM stack”, Nanotechnology, vol. 22, no. 45, p. 455702, 2011.

[64] K. Shubhakar, K. L. Pey, M. Bosman, R. Thamankar, S. S. Kushvaha, Y. C. Loke, Z. R. Wang, N. Raghavan, X. Wu, and S. J. O’Shea, “Nanoscale physical analysis of localized breakdown events in HfO_2/SiO_X dielectric stacks: A correlation study of STM induced BD with C-AFM and TEM”, 19th IEEE International Symposium on the Physical and Failure Analysis of Integrated Circuits, pp. 1–7, 2012.

[65] K. L. Pey, C. H. Tung, L. J. Tang, W. H. Lin, and M. K. Radhakrishnan, “Size difference in dielectric-breakdown-induced epitaxy in narrow n- and p-metal oxide semiconductor field effect transistors”, Appl. Phys. Lett., vol. 83, no. 14, pp. 2940–2942, 2003.

[66] K. L. Pey, R. Ranjan, C. H. Tung, L. J. Tang, W. H. Lin, and M. K. Radhakrishnan, “Gate dielectric degradation mechanism associated with DBIE evolution”, in 2004 IEEE International Reliability Physics Symposium. Proceedings, pp. 117–121.

[67] G. Martín, M. B. González, F. Campabadal, F. Peiró, A. Cornet, and S. Estradé, “Transmission electron microscopy assessment of conductive-filament formation in Ni-HfO_2-Si resistive-switching operational devices”, Appl. Phys. Express, vol. 11, no. 1, p. 14101, 2018.

Chapter 7

Conclusions

The main goal of this thesis has been to apply *in-situ* TEM electrical measurements using a STM tip, combined with TEM imaging and spectroscopic techniques, in order to address the characterization of relevant nanomaterials. This system has not only been used to measure electrical properties, but also to carry out *in-situ* experiments with Joule heating and to apply mechanical stresses.

A review of the different *in-situ* TEM techniques, their development over the years and their impact in the scientific community has been presented.

The instrumental used in this thesis, in particular, the TEM-STM system, has been described. In addition, two techniques for the preparation of specific samples for *in-situ* TEM-STM experiments have been presented: for nanostructured samples (2D materials, nanowires, etc), and for localized samples (devices, thin layers, bulk samples, etc). A gridcase that allows the use of conventional TEM grids in the TEM-STM system has been designed and fabricated in the context

of this thesis. The use of this homemade gridase has allowed us to improve the experiments, offering more reproducibility and versatility. Finally, the calibration of the electrical measurements of the system has been carried out.

The obtained results are grouped from 2D materials to functional devices. In the following paragraphs are summarized the main findings for the studied materials.

- **Effects of electrical current on graphene oxide(GO)**
  - *In-situ* TEM and Raman spectroscopy have been used to assess the effects of the electrical current applied through a single graphene oxide (GO) sheet on its structural parameters.
  - The conductivity of a single sheet of GO before and after the application of Joule heating has been determined using *in-situ* TEM. The resistance of the GO sheets exposed to the electrical current decreases due to the Joule heating induced reduction.
  - Raman spectroscopy has been performed in the very same GO sheet in order to correlate the effect of the current in the structural parameters of the single GO sheet. A lower content of sp^3 bonds is observed due to the carboxyl functional groups removal. As the electrical current increases through the GO sheet, the removal of hydroxyl groups starts inducing the formation of a high disordered carbon structure.
  - Joule heating effect can be used for the reduction of GO but the applied power has to be limited in order to avoid an amorphization of the graphene-based structure takes place.

- **Piezoelectric and ferroelectric behaviour of α-La_2WO_6**
  - The elucidation of the piezo and ferroelectric behaviour at local level of lead-free α-La_2WO_6 thin films has been carried out using *in-situ* TEM.
  - The TEM-STM holder has been used as a nanostressor controlling the applied force by the arm position and I-V characteristics have been acquired while changing the pressure on the film made by the tip. A decrease of the resistance has been observed as higher pressure is applied from the tip to the sample from 8 MΩ to 800 kΩ. This effect can be ascribed to a ΔV produced by the piezoelectricity confirming the local piezoelectric behavior of the α-La_2WO_6 thin films.
  - The ferroelectric behaviour of α-La_2WO_6 thin films has been assessed from the cycle of the hysteresis switching current using the I-V method. The measured coercive voltage is 620 mV.

- **Conductive anisotropy of III-V compounds**
  - The elucidation of the anisotropic electrical conductivity of GaInP $CuPt_B$ type ordered layers has been carried out by using *in-situ* biasing TEM.
  - GaInP structures under study present an ordering that consists of alternating Ga- and In-rich planes on the (-111) and (1-11) planes.
  - HAADF-STEM has been used to confirm the order of GaInP structures and SAED analysis to assess the effect of Sb on the degree of order. The order parameter η of the GaInP structures decreases (from 0.53 to 0.31) as more Sb/P ratio is employed during the growth.
  - The electrical conductivity of GaInP thin films with different degree of order (controlled by the amount of Sb flux during the growth) has been measured in the two orthogonal [110] and [1-10] directions using *in-situ* TEM.
  - The degree of the anisotropy has been calculated as the ratio between the resistivity in both directions. The degree of anisotropy has been calculated as the ratio between the resistivity in the [1-10] and the resistivity in the [110], obtaining values from 5.54 to 1.10)
  - As the degree of order decreases, the anisotropy of the electrical conductivity also decreases. Moreover, the resistivity increases with the order parameter when the current flows perpendicular to the antiphase boundaries (APBs), and it is kept relatively independent from the order parameter in the case that the current flows parallel to the APBs.

- **Switching mechanisms of ReRAM devices**
  - The forming mechanism of conductive filaments (CF) of silicon-aluminium oxynitride (SiAlON) thin films under real operation conditions has been adressed.
    * The electroforming has been made *ex-situ*, at device level, and then the samples have been characterized by TEM in order to correlate the macroscopic effects of the CF formation with the CF nanoscale features.
    * The electroforming process is found to generate some bubble-like features in the Al top electrode, which suggests a gas eruption from the SiAlON layer, and precipitates through the SiAlON layer.
    * EELS analysis has determined that the precipitate corresponds to SiAlON, with its stoichiometry slightly modified, attributable to O^{2-} and N^{3-} ion rearrangement.
  - The study of the forming mechanism in HfO_2 based ReRAM inkjet-printed structures has been also carried out.
    * The characterization of the devices after the electroforming process and several Set-Reset switching cycles has revealed the presence of randomly-distributed bubble-like features with diameters of ∼1 µm due to the formation of crystalline Si agglomerations at the Ag-HfO_2 interface.
    * EELS inspections have discarded a silver electromigration effect, evidencing that the resistive switching mechanism is due to the formation of an oxygen vacancy-based conductive filament going through the HfO_2 layer.

- The elucidation of the mechanism of the CF formation of Ni/HfO_2/Si ReRAM devices has been addressed.
    * The combination of TEM, EELS and EDX detailed characterization carried out in the different states of the ReRAM device (pristine state, HRS (High Resistance State), LRS (Low Resistance State) and HBD (Hard Breakdown)) have enabled the elucidation of the mechanism of *ex-situ* CF formation.
    * A crystalline metallic channel of a Ni-Si-HfO_2 compound is observed through the layer. Two semi-spherical structures consisting of a Ni-Si compound are also observed, one in the Si substrate and the other one in the Ni electrode. Thus, diffusion from the Ni towards the Si substrate and vice versa is observed.
    * *In-situ* biasing TEM experiments have been carried out to observe the formation of the CF in real time and to understand the physical mechanism behind the CF formation.
    * An early forming state of the CF was achieved *in-situ* in the TEM, observing the diffusion from the Ni towards the Si substrate through the oxide layer and enabling a better knowledge of the CF mechanism and its essential role in the behaviour of ReRAM devices.

In-situ microscopy expands the horizons of the characterization and study of materials and, in particular, in the context of this thesis, an *in-situ* TEM-STM system has been used to electrically characterize samples from nanomaterials to functional devices.

Appendix A

Resum en català

Des de la invenció del primer Microscopi Electrònic de Transmissió (TEM) al 1931, ja existia la idea de portar la microscòpia electrònica més enllà de la pura observació: transformar el TEM en un micro-laboratori en què les respostes d'un espècimen a certs estímuls poguessin ser enregistrades en temps real. A aquest concepte de provocar estímuls en la mostra i observar la seva resposta en un TEM se'l va anomenar TEM *in-situ*. Avui dia, les tècniques de TEM *in-situ* estan esdevenint cada cop més rellevants en la comunitat científica.

Les dues tècniques de TEM *in-situ* més tradicionals són, per una banda, les relacionades amb l'escalfament de les mostres dins del microscopi i, per l'altra, amb l'aplicació d'una certa força controlada sobre una mostra, permetent així l'estudi de les seves propietats mecàniques. A més, durant els últims anys s'han anat aconseguint nous avenços en novedosos portamostres de TEM que permeten des de fer passar corrent elèctric a través de la mostra, fins a l'estudi de materials en atmòsferes controlades (tant gasoses com líquides) en la zona del portamostres.

El desenvolupament de nous portamostres no és una feina trivial ja que l'interior del microscopi s'ha de mantenir en ultra-alt buit alhora que l'espècimen es col · loca en un espai reduit entre les dues peces polars. Recentment s'han pogut dur a terme experiments dins del TEM que recreen experiències de laboratori, a la nanoescala, combinant diverses tècniques de TEM *in-situ* i observant les respostes amb resolució atòmica.

En aquesta Tesi, s'ha emprat una tècnica de TEM *in-situ* que permet realitzar mesures elèctriques utilitzant una sonda de microscòpia d'efecte túnel (STM, Scanning Tunneling Microscopy en anglès), tot combinant-la amb imatge TEM i tècniques d'espectroscòpia. A més, aquest sistema no només s'ha utilitzat per a mesurar les propietats elèctriques, sinó també per a dur a terme experiments *in-situ* amb escalfament per efecte Joule o aplicant una tensió mecànica a la superfície de la mostra. D'aquesta manera s'han pogut caracteritzar nanomaterials, des de nanoestructures 2D fins a dispositius completament funcionals.

El **Capítol 1** presenta una introducció general a les diferents tècniques de TEM *in-situ*, el seu desenvolupament al llarg dels anys i la repercusió que han tingut en la comunitat científica.

El **Capítol 2** mostra l'instrumental utilitzat en aquesta tesi i la posada a punt del sistema que s'ha dut a terme. A més s'han presentat dues tècniques de preparació de mostres específiques per a experiments *in-situ* TEM-STM: per a mostres nanoestructurades (materials 2D, nanofils, etc) i per a mostres que necessiten una preparació en un lloc específic (dispositius, capes primes, etc). En aquest cas s'ha donat especial importància a la preparació mitjançant feix d'ions focalitzat (FIB, Focused Ion Beam en anglès). A més, en el context d'aquesta tesi, s'ha dissenyat i fabricat una peça que permet l'ús de reixetes de TEM

convencionals en el sistema TEM-STM. Aquesta peça, manufacturada pel nostre grup, ha permès una millora en els experiments, aportant més versatilitat i reproductibilitat. Per últim, s'ha dut a terme la calibració de les mesures elèctriques del sistema i s'ha estudiat com interpretar les característiques I-V de materials semiconductors obtingudes al llarg d'aquesta Tesi.

Els següents capítols descriuen els resultats d'aquesta caracterització *in-situ* en materials i dispositius nanoestructurats.

El **Capítol 3** mostra l'estudi dels efectes del pas de corrent a través d'un sol full d'òxid de grafè. En aquest estudi s'ha combinat l'ús de la microscòpia *in-situ* amb l'espectroscòpia Raman, per tal de relacionar els efectes elèctrics amb els canvis en els paràmetres estructurals. Com a resultat, s'ha observat que el pas de corrent elèctric a través d'un sol full d'òxid de grafè provoca un estat de reducció inicial amb l'eliminació dels grups funcionals d'oxigen de l'estructura degut a l'efecte d'escalfament Joule. A més, s'observa un menor contingut d'enllaços sp^3 degut a l'eliminació de grups funcionals carboxil. A mesura que el corrent augmenta a través del full d'òxid de grafè, comença també l'eliminació de grups hidroxil, induint d'aquesta manera la formació d'una estructura altament desordenada.

Per tant, podem dir que l'escalfament Joule pot ser utilitzat com a mètode de reducció de l'òxid de grafè, tot i que la potència aplicada s'ha de limitar. En cas contrari, té lloc l'amorfització de l'estructura basada en grafè. Els resultats presentats en aquest capítol mostren la importància d'analitzar de manera exhaustiva els efectes del corrent elèctric a través de fulls 2D de materials de carboni per tal d'entendre com responen durant el seu ús en nano-dispositius.

El **Capítol 4** recull la caracterització piezoelèctrica i ferroelèctrica de capes primes d'òxids funcionals lliures de plom. En particular, en

aquesta tesi s'ha estudiat la resposta piezoelèctrica i ferroelèctrica d'una capa prima d' α-La_2WO_6 crescuda per dipòsit per ablació amb làser polsat (PLD, Pulsed Laser Deposition) sobre un substrat de $SrTiO_3$ (STO).

Per fer una caracterització qualitativa del seu comportament piezoelèctric s'ha mesurat la característica I-V per a cada pas mecànic de la punta d'STM dins del TEM. D'aquesta manera, durant l'experiment s'observa una disminució de la resistència elèctrica a mesura que es va aplicant més pressió a la superfície de la mostra amb la punta, des de 8 MΩ fins a 800 kΩ .

La caracterització del comportament ferroelèctric s'ha fet a partir del cicle d'histerèsi de commutació de corrent utilitzant el mètode I-V. Amb aquest mètode s'obté un pic de corrent quan el voltatge aplicat és proper a la tensió coercitiva de la mostra, que correspon a la contribució de la reorientació dels dipols del material ferroelèctric. Amb aquest estudi s'ha obtingut que el valor del voltatge coercitiu de la capa prima és de 620 mV.

Així doncs, amb les mesures elèctriques *in-situ*, s'ha pogut confirmar i estudiar el comportament piezoelèctric i ferroelèctric d'una capa prima a nivell local.

El **Capítol 5** mostra l'estudi de l'anisotropia en la conductivitat d'estructures ternàries III-V ordenades utilitzades en cèl · lules solars tàndem multicapa. Concretament es tracta de capes de GaInP crescudes amb diferents ratios de Sb/P durant el creixement per MOVPE sobre un substrat de Ge (001) amb 6° de desorientació cap a l'eix [111] més proper. Aquestes mostres presenten ordre del tipus $CuPt_B$ en els plans (1-11) degut a la desorientació del substrat, el qual

disminueix en funció del flux de Sb aplicat durant el creixement de la mostra.

En primer lloc, s'ha fet un estudi TEM preliminar confirmant l'estructura de la mostra. Per a aquest estudi s'han preparat dues lamel · les per a cada mostra (cada mostra ha estat crescuda amb diferents quantitats de flux de Sb) en les dues direccions ortogonals, la [110] i la [1-10]. D'aquesta manera, fent difracció, s'ha observat que en el cas de la direcció [110] existeixen punts addicionals als de l'estructura zinc blenda a les posicions $(h \pm \frac{1}{2}, k \mp \frac{1}{2}, l \pm \frac{1}{2})$ degut a l'ordre. A més, s'ha observat que la intensitat relativa d'aquests punts esdevé més i més feble a mesura que augmenta el flux de Sb, la qual cosa confirma que l'ús de Sb durant el creixement de les mostres fa disminiur el paràmetre d'ordre.

En segon lloc, s'ha estudiat com la conductivitat en les dues direccions de la mostra té una forta dependència amb l'ordre. A partir de les mesures elèctriques a través de la capa de GaInP s'ha vist que a mesura que el paràmetre d'ordre disminueix, l'anisotropia de la conductivitat elèctrica disminueix també. A més, s'ha observat com la resistivitat augmenta amb el paràmetre d'ordre quan el corrent passa perpendicular a les fronteres d'antifase (direcció [1-10]), però es manté relativament independent del paràmetre d'ordre quan el corrent passa paral · lel a les fronteres d'antifase (direcció [110]).

El **Capítol 6** aborda l'estudi amb TEM de la formació de filaments conductors (CF) i del mecanisme de commutació resistiva en tres dispositius ReRAM diferents.

La primera part del capítol es centra en l'estudi del mecanisme de commutació sota condicions reals d'operació de capes primes de SiAlON crescudes mitjançant PLD.

L'electro-conformació dels CF es fa *ex-situ* a nivell de dispositiu i posteriorment les mostres són caracteritzades per TEM, per tal de correlacionar els efectes macroscòpics observats en el dispositiu amb les característiques a la nanoescala dels CF.

Durant l'estudi s'ha observat que el procés de conformació genera certes modificacions en forma de bombolla, les quals suggereixen erupcions gasoses de la capa de SiAlON. A més, s'ha trobat també una petita elevació de l'elèctrode d'Al, provocat per un precipitat a la interfície Al/SiAlON. S'ha determinat a partir dels anàlisis EELS que aquest precipitat correspon a SiAlON però amb una estequiometria lleugerament modificada degut a un procés de difusió tant d'oxigen com de nitrogen.

En la segona part del capítol s'estudia amb TEM el mecanisme de commutació resistiva de dispositius ReRAM fabricats mitjançant procediments d'injecció de tinta, tant pel HfO_2 com pels elèctrodes. La caracterització dels dispositius es duu a terme després del procés de conformació i diverses commutacions entre els estats d'alta i baixa resistència, manifestant la presència de bombolles en l'elèctrode degudes a la formació d'aglomerats cristal · lins de Si a la interfície de Ag/HfO_2. A més, els estudis d'EELS descarten l'efecte d'electromigració de plata, evidenciant d'aquesta manera que el procés de commutació resistiva es deu a la formació de CF de vacants d'oxigen a través de la capa de HfO_2.

Finalment, a la tercera part del capítol 6 es presenta l'estudi del mecanisme de formació dels CF de dispositius ReRAM de $Ni/HfO_2/Si$, fabricats sobre un substrat de Si mitjançant dipòsit de capes atòmiques (ALD, Atomic Layer Deposition).

S'han caracteritzat diverses mostres per tal d'estudiar els diferents estats d'una memòria ReRAM: estat verge, HRS (estat d'alta

resistència), LRS (estat de baixa resistència) i HBD (estat de forta ruptura). En tots els casos en què el CF s'ha conformat *ex-situ*, s'observa un canal metàl · lic cristal · lí a través de la capa de HfO_2, compost per Ni, Si i HfO_2. A més, s'observen també dues estructures en forma de semiesfera compostes per Ni i Si, una al substrat de Si i l'altre a l'electròde de Ni. Per tant, podem dir que s'ha produït una difusió de Ni cap al substrat de Si i viceversa.

A més, s'han dut a terme experiments de TEM *in-situ* per tal d'observar la conformació dels CF en temps real i entendre el procés físic que hi ha darrere del mecanisme de commutació. Durant els experiments s'ha aconseguit un estat preliminar dels CF, i s'ha observat dins del TEM la difusió de Ni cap al substrat de Si a través de la capa de HfO_2.

En els diferents capítols d'aquesta tesi s'ha donat resposta a problemes de ciència de materials amb l'ajut d'una tècnica de TEM *in-situ* tot combinant-la amb altres tècniques d'espectroscòpia i difracció. El desenvolupament d'aquesta tècnica ha permès caracteritzar les propietats del materials a nivell nano, des de materials 2D fins a dispositius funcionals.

Appendix B

Scientific Curriculum

Education

2010 Llicenciatura en Enginyeria Electrònica, Universitat de Barcelona

2012 MSc in Biomedical Engineering, Universitat de Barcelona.

Appointments held

2013-2018 Formación de Personal Investigador (FPI) grant holder, as a PhD student at LENS (Laboratory of Electron Nanoscopies), Departament d'Enginyeria Electrònica i Biomèdica, Universitat de Barcelona.

Research stages

2017 Unidad de Nanotecnología, Centro de Bioinnovación y supercomputación-SCBI, Universidad de Málaga, Spain. May (1 week)

2017 Barcelona Microelectronics Institute-National Microelectronics Centre-CSIC, Spain. October-December (3 months)

Workshops & schools

2010 Innovative Engineering Coaching, Enginycat, La Salle URL, Spain. September.

2011 11th TEM-UCA European Summer Workshop, Transmission Electron Microscopy of Nanomaterials. Universidad de Cádiz, Spain. July.

2011 1st School on Tramission Electron Microscopy, Instituto Universitario de Investigación de Nanociencia de Aragón (LMA-INA), Universidad de Zaragoza, Spain. December.

2012 Introduction to Statistics and Data Processing using the R programming language, University of Barcelona, Spain. November - December.

2014 Advanced Analytical modes in the Nanoscale: Electron Energy Loss Spectrosocpy and Tomography in the TEM, Centres Científics i Tecnològics de la Universitat de Barcelona, Barcelona, Spain. June.

2015 IAMNANO 2015 - The International Workshop on Advanced and In-situ Microscopies of Functional Nanomaterials and Devices, Helmholtz-Zentrum Geesthacth, Hamburg, Germany. July.

2016 Oral skills for teaching and research purposes (Advanced), University of Barcelona, Spain. November.

2017 Basic skills and tools to teach content subjects in English, University of Barcelona, Spain. May-July.

2017 Jornada sobre la Prevenció de Riscos als laboratoris de Recerca, OSSMA - University of Barcelona, Spain. October.

Grants, honors & awards

2011 Formación de Personal investigador (FPI) Grant BES-2011-043928 from Ministerio de Economia y Competitividad (Spain).

Physics degree final project supervision

2018 Structural characterization of GaN nanowires using TEM, Daniel del Pozo Bueno

Journal articles

1. Thomas Carlier, Marie Hélène Chambrier, Anthony Ferri, Sonia Estradé, Jean François Blach, Gemma Martín, Belkacem Meziane, Francesca Peiró, Pascal Roussel, Freddy Ponchel, Denis Rèmiens, Albert Cornet, and Rachel Desfeux. Lead-Free α-La_2WO_6 Ferroelectric Thin Films. *ACS Applied Materials and Interfaces*, 7(44):24409–24418, 2015

2. Lorenzo Caccamo, Giulio Cocco, Gemma Martín, Hao Zhou, Sönke Fundling, Alaaeldin Gad, Matin Sadat Mohajerani, Mahmoud Abdelfatah, Sonia Estradé, Francesca Peiró, Wanja Dziony, Heiko Bremers, Andreas Hangleiter, Leonhard Mayrhofer, Gerhard Lilienkamp, Michael Moseler, Winfried Daum, and Andreas Waag. Insights into Interfacial Changes and Photoelectrochemical Stability of $In_xGa_{1-x}N$ (0001) Photoanode Surfaces in Liquid Environments. *ACS Applied Materials and Interfaces*, 8(12):8232–8238, 2016

3. Pau Torruella, Catalina Coll, Gemma Martín, Lluís López-Conesa, María Vila, Carlos Díaz-Guerra, María Varela, María Luisa Ruiz-González, Javier Piqueras, Francesca Peiró, and Sònia Estradé. Assessing oxygen vacancies in bismuth oxide through EELS measurements and DFT simulations. *Journal of Physical Chemistry C*, 121(39), 2017

4. Gemma Martín, Mireia B. González, Francesca Campabadal, Francesca Peiró, Albert Cornet, and Snia Estradé. Transmission electron microscopy assessment of conductive-filament formation in Ni-HfO_2-Si resistive-switching operational devices. *Applied Physics Express*, 11(1), 2018

5. Oriol Blázquez, Gemma Martín, Ivan Camps, Antonio Mariscal, Julian López-Vidrier, Joan Manel Ramirez, Sergi Hernández, Sonia Estrade, Francesca Peiro, Rosalía Serna, and Blas Garrido. Memristive behaviour of Si-Al oxynitride thin films: The role of oxygen and nitrogen vacancies in the electroforming process. *Nanotechnology*, 29(23):235702, jun 2018

6. Gemma Martín, Aïda Varea, Albert Cirera, Sònia Estradé, Francesca Peiró, and Albert Cornet. Effects of Electric Current on Individual Graphene Oxide Sheets Combining in-situ Transmission Electron Microscopy and Raman Spectroscopy. *Nanotechnology*, Just Accepted, 2018

Contributions in conferences

1. Martín G., Claramunt S., Varea A., Yedra L., Rebled J. M., Sánchez-Hidalgo R., López-Díaz D., Velázquez M. M., Cirera A., Peiró F., Estradé S., and Cornet A. In situ reduction of graphene oxide in TEM-STM. In *V Jornades del Institut de Nanociencia i Nanotecnologia de la Universitat de Barcelona, Facultad de Física, Unversitat de Barcelona (15 Noviembre 2012)*, 2012

3. L. López-Conesa, G. Martín, M. Vila, C. Díaz-Guerra, J. Piqueras, S. Estradé, and F. Peiró. Structural, chemical and in situ electrical characterization of Bi_2O_3 nanowires. In *Microscopy at the Frontiers of Science 2013*, 2013

4. L. López-Conesa, G. Martín, S. Estradé, F. Peiró, M. Vila, C. Díaz-Guerra, and J. Piqueras. Caracterización mediante técnicas de microscopía de transmisión de nanohilos de Bi_2O_3. In *7th Workshop of IMAGINE, Materials at Sub-Angstrom*

resolution, meeting of the Consolider Project CSD2009-00013, Facultad de Ciencias, Universidad de Cadiz, 20-21 de Junio 2013, 2013

5. G. Martín, S. Claramunt, A. Varea, L. Yedra, J.M. Rebled, R. Sánchez-Hidalgo, D. López-Díaz, M.M. Velázquez, A. Cirera, F. Peiró, S. Estradé, and A. Cornet. In situ reduction of graphene oxide. In *18th Internation Microscopy Congress*, 2014

6. G. Martín, S. Claramunt, A. Varea, L. Yedra, J.M. Rebled, R. Sánchez-Hidalgo, D. López-Díaz, M.M. Velázquez, A. Cirera, F. Peiró, S. Estradé, and A. Cornet. In situ reduction of graphene oxide. In *2014 MRS Fall Meeting Exhibit*, 2014

7. Martín G., Claramunt S., Varea A., Yedra L., Rebled J. M., Sanchez-Hidalgo R., López-Díaz D., Velázquez M. M., Cirera A., Peiró F., Estradé S., and Cornet A. In situ reduction of graphene oxide by joule heating with TEM-STM system. In *18th International Microscopy Conference, Praga, Republica Checa, 7-12 Septiembre 2014*, 2014

8. T. Carlier, M. Chambrier, A. Ferri, S. Estradé, J. Blach, G. Martín, B. Meziane, F. Peiró, P. Roussel, A. Cornet, and R. Desfeux. New lead-free α-La_2WO_6 ferroelectric thin films. In *E-MRS Spring Meeting*, 2015

9. G. Martín, A. Varea, J.M. Rebled, R. Sánchez-Hidalgo, D. López-Díaz, M.M. Velázquez, A. Cirera, F. Peiró, S. Estradé, and A. Cornet. In situ TEM study of reduction of graphene oxide by joule heating. In *10th Spanish Conference on Electron Devices (CDE), Aranjuez, 11-13 Febrero 2015.*, 2015

10. Gemma Martín, Thomas Carlier, Marie-Hélène Chambrier, Sonia Estradé, Francesca Peiró, Anthony Ferri, Rachel Desfeux,

and Albert. Cornet. In situ study of piezoelectricity and ferroelectricity of thin films in a TEM. In *XI Reunion Proyecto IMAGINE:CONSOLIDER*, 2015

11. T. Carlier, M.H. Chambrier, A. Ferri, S. Estradé, J. F Blach, G. Martín, B. Meziane, F. Peiró, P. Roussel, A. Cornet, and R. Desfeux. New lead free α-La_2WO_6 ferroelectric thin films: Nouveau compose ferroelectrique sans plomb. In *Congres 2015 de la Societe Chimique de France*, 2015

12. G. Martín, T. Carlier, M.H. Chambrier, S. Estradé, F. Peiró, A. Ferri, R. Desfeux, and A. Cornet. In situ study of piezoelectricity and ferroelectricity of thin films in a TEM. In *MRS Spring Meeting Exhibit 2015*, 2015

13. P. Torruella, R. Arenal, Z. Saghi, L. Yedra, F. de la Peña, A. Eljarrat, M. Estradé, L. López-Conesa, G. Martín, A. López-Ortega, G. Salazar-Álvarez, J. Nogués, P.A. Midgley, F. Peiró, and Estradé S. Multidimensional EELS: from spectrum image to spectrum volume and beyond. In *Energy Materials Nanotechnology Spain San Sebastian 1-4 Septiembre 2015*, 2015

14. G. Martín, T. Carlier, M.H. Chambrier, S. Estradé, F. Peiró, A. Ferri, R. Desfeux, and A. Cornet. In situ study of piezoelectricity and ferroelectricity of thin films in a transmission electron microscope. In *Microscopy at the Frontiers of Science 2015*, 2015

15. G. Martín, T. Carlier, M.H. Chambrier, S. Estradé, F. Peiró, A. Ferri, R. Desfeux, and A. Cornet. In situ study of piezoelectricity and ferroelectricity of thin films in a transmission electron microscope. In *IAM nano 2015*, 2015

16. P. Torruella, R. Arenal, Z. Saghi, L. Yedra, F. de la Peña, A. Eljarrat, M. Estrader, L. López-Conesa, G. Martín, A. López-Ortega, G. Salazar-Álvarez, J. Nogués, P.A. Midgley, F. Peiró, and Estradé S. Accessing the chemical and optoelectronic properties of nanostructures in 3D: The EELS spectrum volume. In *Energy Materials Nanotecnology Open Acces Week, Chengdu China, 22-25-Septiembre*, 2015

17. G. Martín, Chambrier M.H., S. Estradé, F. Peiró, and A. Cornet. In situ TEM study of piezoelectricity and ferroelectricity of α - La_2WO_6 thin films. In *MRS (Materials Research Society) Spring Meeting, Symposium P: Nanogenerators and Piezotronics, San Francisco 6-10 Abril (2015)*, 2015

18. P. Torruella, A. Eljarrat, G. Martín, J.M. Rebled, L. López-Conesa, C. Coll, A. Ruiz, S. Plana, S. Estradé, and F. Peiró. EELS tomography: recovering the spectrum volume from MVA methods. In *10e edition des Journees de l'EELS, Tarragona, 28th 30th June (2016)*, 2016

19. G. Martín, M. B González, F. Campabadal, S. Estradé, F. Peiró, and A. Cornet. In situ TEM assessment of nanoresistive switching in Ni-HfO_2-Si capacitors: the conducting filament mechanism. In *11th Spanish Conference on Electron Devices (CDE2017)*, 2016

20. P. Torruella, M. Dalmases, V. Fernandez-Altable, A. Cabot, M. Ibañez, J. Llorca, L. López-Conesa, G. Martín, S. Estradé, and F. Peiró. Synthesis and characterization of Ag_2Se-based hybrid and ternary semiconductor nanocrystals with potential termoelectric applications. In *16th European Microscopy Conference (EMC2016), MS0: Nanoparticles: from synthesis to applications, 28th August - 2nd September Lyon, France (2016)*, 2016

21. P. Torruella, C. Coll, G. Martín, L. López-Conesa, M. Vila, C. Díaz-Guerra, M. Varela, J. Ruiz-González, M.L. Piqueras, F. Peiró, and Estradé S. EELS assessment of oxidation state in Bi_2O_3. In *FFSCI Nanoscience and EMN Croatia Meeting, Dubrovnik, May 3th-7th (2017)*, 2017

22. O. Blázquez, G. Martín, I. Camps, J.M. Ramírez, S. Hernández, S. Estradé, F. Peiró, R. Serna, A. Cornet, and B. Garrido. Structural and electrical characterization of SiAlON memristors: the role of oxygen vacancies in the electroforming process. In *European Materials Research Society (EMRS) Spring Meeting 2017*, 2017

23. G. Martín, M.B. González, F. Campabadal, S. Estradé, F. Peiró, and A. Cornet. Elucidation of conducting filament formation in nanoresistive switching in Ni-HfO_2-Si capacitors by in-situ TEM. In *Microscopy of Semiconducting Materials (MSM-XX), Oxford, (10-13 Abril 2017)*, 2017

24. G. Martín, M.B. González, F. Campabadal, S. Estradé, F. Peiró, and A. Cornet. Elucidation of conducting filament formation in HfO_2 based ReRAM devices by in-situ TEM. In *EUROMAT 2017, European Congress and Exhibition in Advanced Materials and Processes, Thessaloniki (Grecia), 17-22 Septiembre 2017*, 2017

25. G. Martín, S. Estradé, F. Peiró, and A. Cornet. In-situ electrical measurements of nanomaterials: from 2D structures to functional devices. In *Microscopy at Frontiers of Science 2017 (MFS 2017)*, 2017

University teaching

2015-16 Informàtica, Enginyeria Electrònica de Telecomunicació, University of Barcelona.

2016-17 Informàtica, Enginyeria Electrònica de Telecomunicació, University of Barcelona.

2016-17 Components i circuits electrònics, Enginyeria Electrònica de Telecomunicació, University of Barcelona.

2017-18 Fonaments de laboratori, Enginyeria Electrònica de Telecomunicació, University of Barcelona.

2017-18 Components i circuits electrònics, Enginyeria Electrònica de Telecomunicació, University of Barcelona.

Participation in committees

2010-11 Member of the Student Council of the Electronics Engineering degree, University of Barcelona.

2016-present Member of the Department Council of the Electronics Department, University of Barcelona.

2017-present Representant of the phD students in the Committee of the Nanoscience Doctoral Programe, University of Barcelona.

Scientific dissemination

2014 Fira del Coneixement, Berga, Spain

2015 Festa de la ciència de la Universitat de Barcelona, University of Barcelona, Spain

2016 II Festa de la ciència de la Universitat de Barcelona, University of Barcelona, Spain

2017 III Festa de la ciència de la Universitat de Barcelona, University of Barcelona, Spain.

2017 Festival de la Nanociencia i Nanotecnologia 10alamenos9, Barcelona, Spain.

2018 Espai Ciència, Saló de l'Ensenyament, Barcelona, Spain.

Languages

Spanish and Catalan native level.

English spoken (well), read (well) and written (well). Proficient use of the language in a professional context.

French spoken (sufficient), read (well) and written (sufficient).